



저작자표시-비영리-변경금지 2.0 대한민국

이용자는 아래의 조건을 따르는 경우에 한하여 자유롭게

- 이 저작물을 복제, 배포, 전송, 전시, 공연 및 방송할 수 있습니다.

다음과 같은 조건을 따라야 합니다:



저작자표시. 귀하는 원저작자를 표시하여야 합니다.



비영리. 귀하는 이 저작물을 영리 목적으로 이용할 수 없습니다.



변경금지. 귀하는 이 저작물을 개작, 변형 또는 가공할 수 없습니다.

- 귀하는, 이 저작물의 재이용이나 배포의 경우, 이 저작물에 적용된 이용허락조건을 명확하게 나타내어야 합니다.
- 저작권자로부터 별도의 허가를 받으면 이러한 조건들은 적용되지 않습니다.

저작권법에 따른 이용자의 권리는 위의 내용에 의하여 영향을 받지 않습니다.

이것은 [이용허락규약\(Legal Code\)](#)을 이해하기 쉽게 요약한 것입니다.

[Disclaimer](#)

공학박사 학위논문

고농도 수계 전해질을 활용한 고용량
고효율 수계 이차전지 설계에 관한
연구

**A study for designing cost-efficient and high-energy
density aqueous rechargeable battery**

2021 년 8 월

서울대학교 대학원

재료공학부

이 명 환

고농도 수계 전해질을 활용한 고용량
고효율 수계 이차전지 설계에 관한 연구

A study for designing cost-efficient and high-energy density
aqueous rechargeable battery

지도 교수 강 기 석

이 논문을 공학박사 학위논문으로 제출함

2021 년 8 월

서울대학교 대학원

재료공학부

이 명 환

이명환의 박사 학위논문을 인준함

2021 년 6 월

위 원 장 최 인 석

부위원장 강 기 석

위 원 최 장 욱

위 원 김 대 형

위 원 이 상 영

Abstract

A study for designing cost-efficient and high-energy density aqueous rechargeable battery

Lee, Myeong Hwan

Department of Materials Science and Engineering

College of Engineering

The Graduate School

Seoul National University

The surging requirements for eco-friendly and sustainable energy storage systems have significantly boosted and advanced the mass production of rechargeable lithium-ion batteries (LIBs) in the current energy market. Despite the promising outlook for conventional LIBs, many obstacles to their use for such large-scale applications have yet to be overcome, including rising costs stemming from the limited abundance of raw materials and safety concerns arising from the use of highly flammable organic electrolytes. As an alternative safer chemistry, the batteries that employ aqueous electrolytes have been investigated. However, traditional aqueous electrolytes provide a narrow electrochemical stability window of ~ 1.23 V due to occurring the thermodynamic water decomposition outside this window. This narrow stability window inevitably yields a limited energy density for aqueous systems, which make them unfit for practical application. To improving the energy

density of aqueous battery system, recent invention of highly concentrated aqueous electrolyte systems has paved a way toward the high-voltage aqueous batteries, which have wide electrochemical stability window by forming the stable solid-electrolyte interphase (SEI) layer with salt decomposition and preventing the water splitting. Although, super-concentrated electrolyte systems enable high-energy density of aqueous batteries, it still has major obstacle for their commercialization due to the need for generally high-cost organic solutes in the high-concentration electrolyte. In this thesis, I present a design strategy for developing a low-cost and high-energy density aqueous battery system, particularly using on high-concentration NaClO_4 aqueous electrolyte-based battery and the organic aqueous battery systems.

In Chapter 2, all the commonly used low-cost solutes for high-concentration aqueous electrolyte system are revisited. Finally, it is discovered that the use of NaClO_4 solute effectively results in a wide electrochemical stability window by suppressing water decomposition and induces stable solid-electrolyte interphase (SEI) layer formation without involving the reduction of salt anions. The SEI layer, composed of Na_2CO_3 and Na–O compounds including NaOH, guarantees the excellent electrochemical storage stability of the full-cell composed of $\text{Na}_4\text{Fe}_3(\text{PO}_4)_2(\text{P}_2\text{O}_7)$ cathode and $\text{NaTi}_2(\text{PO}_4)_3$ anode for the extended period of time. This new-class of electrolyte systems provides remarkable cycle stability and a coulombic efficiency, which outperforms the state-of-the-art super-concentrated systems based on NaCF_3SO_3 . This chapter will provide an important guidance for

the realization of low-cost high-voltage aqueous batteries.

In Chapter 3, the facility of low-cost high-concentration NaClO_4 electrolyte is broadened by employing the multi-electron-redox phenazine molecule (*i.e.*, 5,10-dihydro-5,10-dimethyl phenazine, DMPZ), one of the most promising p-type organic cathode materials. It is presented that novel approaches to facilitate the complete utilization of the capacity and drastically improve the cycle durability by employing an electrolyte that is the most compatible with a DMPZ electrode. With the aid of deep learning and experimental validation, an aqueous solution is adopted as the most suitable electrolyte owing to the low solubility of the DMPZ molecule, resulting in enhanced capacity retention, which contrasts with the poor cycling performance in non-aqueous electrolytes. In addition, to further suppress the dissolution and water decomposition, a high-concentration electrolyte strategy is applied. Thereby, the DMPZ with high-concentration aqueous electrolyte successfully provide significantly improved capacity retention with outstanding long-life durability. This chapter will provide a deep understanding about the compatibility between organic electrode materials and electrolytes, which is a key factor toward the successful implementation of rechargeable organic batteries with high-energy density and long cycle life.

I believe that the deep study in this thesis on low-cost high-concentration aqueous system offer two major key aspects: 1) designing strategy for exploration of a new salts for high-concentration aqueous electrolytes, which could be widened the electrochemical stability window by suppressing water decomposition and robust

surface layer formation without salt decomposition, and 2) deep understanding and facilitating the full utilization of a organic molecule electrode by employing the most appropriate electrolyte that provides low solubility of DMPZ. It will provide important guidance for the realization of low-cost high-energy density aqueous batteries.

Keywords: Electrochemistry, Secondary batteries, Aqueous batteries, High-concentration electrolyte

Student Number: 2012-24163

Contents

List of Tables	ix
----------------------	----

List of Figures	x
-----------------------	---

Chapter 1. Introduction	1
--------------------------------------	----------

1.1 Research motivation and objectives	1
--	---

1.2 Introduction to aqueous batteries	3
---	---

1.3 Emerging the super-concentrated aqueous electrolyte for high-energy density aqueous battery system	7
---	---

1.4 Purpos of this research.....	9
----------------------------------	---

1.5 References	11
----------------------	----

Chapter 2. Toward a low-cost high-voltage sodium aqueous rechargeable battery.....	26
---	-----------

2.1 Research background.....	26
------------------------------	----

2.2 Experimental method.....	31
------------------------------	----

2.2.1	Preparation of aqueous electrolyte and electrode materials	31
2.2.2	Electrochemical measurements	32
2.2.3	Materials characterization	33
2.3	Result and discussion	34
2.3.1	Selection guideline for the low-cost high-concentration aqueous electrolyte and their chemistry for electrochemical stability in rechargeable aqueous batteries	34
2.3.2	Electrochemical performance of rechargeable aqueous sodium battery in highly concentrated NaClO ₄ aqueous electrolyte system	44
2.3.3	Analysis of the surface protective layer formed in high-concentration aqueous electrolyte	53
2.3.4	Mechanism of surface layer forming in high-concentration NaClO ₄ aqueous electrolytes	61
2.4	Concluding remarks	66
2.5	References	67

Chapter 3. Unveiling the superior durability of multi-redox molecules employing high-concentration electrolyte for high-energy and sustainable aqueous battery	79
3.1 Research background	79

3.2 Experimental method.....	83
3.2.1 Preparation of aqueous electrolyte and electrode.....	83
3.2.2 Computational details	84
3.2.3 Electrochemistry of DMPZ aqueous battery	85
3.2.4 Dissolution behaviors of the DMPZ experiments	86
3.2.5 Materials characterization	87
3.3 Result and discussion	88
3.3.1 Solubility feature of DMPZ in various electrolyte solutions and electrochemical property of DMPZ in aqueous electrolyte	88
3.3.2 Prediction of the solubility of the DMPZ in generic battery electrolyte solutions via deep learning.....	96
3.3.3 Strategy for perfectly utilizing the performance of DMPZ.....	100
3.3.4 Kinetic hindrance of the DMPZ initial charge process in 17 m NaClO ₄ aqueous electrolyte.....	108
3.3.5 Durable electrochemical performance of the DMPZ cell employing the high-concentration aqueous electrolyte	115
3.3.6 Structural and morphological analysis of the DMPZ cycled in the high- concentration aqueous electrolyte with long-term cycles	121
3.3.7 Comparison of the performance of the DMPZ with previously reported works.....	128
3.4 Concluding remarks.....	136
3.5 References	138

Chapter 4. Conclusion	152
------------------------------------	------------

Chapter 5. Abstract in Korean	158
--	------------

List of Tables

Table 2.1. Properties of conventional non-aqueous electrolyte (1 M LiPF_6) vs. aqueous electrolyte salts. The cost from Sigma-Aldrich with an assay above 99% was used. The ionic conductivity was measured at 25 °C..... 39

Table 3.1. Prediction of the solubility of DMPZ in the generic battery electrolyte solution..... 99

Table 3.2. Comparison of the performance of the DMPZ with previously reported works..... 131

List of Figures

Figure 2.1. (a) Raman spectra of water molecules in various aqueous solutions, namely, saturated 1.3 m Na₂SO₄, saturated 10.7 m NaNO₃, saturated 21 m LiTFSI, saturated 9.26 m NaCF₃SO₃, and saturated 17 m NaClO₄ in water. The broadening of the spectra between the two black dashed lines in the range of 2,900–3,800 cm⁻¹ is attributed to O–H stretching modes of clustered water molecules with diverse hydrogen bonding. The sharp peak marked by the orange line near 3,550 cm⁻¹ is attributed to cation-solvated water molecules that are free of hydrogen bonding. (b) Raman spectra of NaClO₄ electrolyte at various salt concentrations in the range of 2,700–4,000 cm⁻¹ showing O–H stretching modes of water molecules.....40

Figure 2.2. Raman spectra of conventional aqueous electrolytes in various salt concentrations.....41

Figure 2.3. (a) ClO₄ stretching modes in Raman spectra for NaClO₄ electrolytes of different salt concentrations (1 m, 5 m, 10 m, and 17 m). (b) Deconvolution fitting results of V_s (ClO₄⁻) stretching mode in Raman spectra.....42

Figure 2.4. (c) Overall electrochemical stability window and (a and b) enlarged regions near the cathodic (HER) and anodic (OER) limits of 17 m NaClO₄ electrolyte determined from CV measurements between -1.55 and 1.65 V vs. SCE at 1 mV s⁻¹ on gold working electrodes. The potential was converted to a Na/Na⁺ reference for convenience. The bump near 2.1 V vs. Na/Na⁺ in (a and c) is attributed to bubble

formation on a gold electrode.....43

Figure 2.5. (a and b) SEM images and (c) XRD pattern of the pristine $\text{Na}_4\text{Fe}_3(\text{PO}_4)_2(\text{P}_2\text{O}_7)$ powder. (d and e) SEM images and (f) XRD pattern of the pristine $\text{NaTi}_2(\text{PO}_4)_3$ powder.....48

Figure 2.6. Comparison of voltage profiles of (a) $\text{Na}_4\text{Fe}_3(\text{PO}_4)_2(\text{P}_2\text{O}_7)$ electrode and (b) $\text{NaTi}_2(\text{PO}_4)_3$ electrode in 1 m and 17 m NaClO_4 electrolytes at constant current of 1C. The half-cell data in (a) and (b) were obtained from a three-electrode system consisting of $\text{Na}_4\text{Fe}_3(\text{PO}_4)_2(\text{P}_2\text{O}_7)$ and $\text{NaTi}_2(\text{PO}_4)_3$ as working electrodes, a SCE as the reference electrode, and activated carbon as the counter electrode.....49

Figure 2.7. Galvanostatic charge/discharge performance and cycle stability of a $\text{NaTi}_2(\text{PO}_4)_3$ half-cell.....50

Figure 2.8. Galvanostatic profiles of the $\text{Na}_4\text{Fe}_3(\text{PO}_4)_2(\text{P}_2\text{O}_7)/\text{NaTi}_2(\text{PO}_4)_3$ full-cell in (a) 1 m and (b) 17 m NaClO_4 electrolytes at 1C. The insets of (a) and (b) present CV curves of the $\text{Na}_4\text{Fe}_3(\text{PO}_4)_2(\text{P}_2\text{O}_7)/\text{NaTi}_2(\text{PO}_4)_3$ full-cell at a scan rate of 0.1 mV s^{-1} in (a) 1 m and (b) 17 m NaClO_4 electrolytes.....51

Figure 2.9. (a) Cycle stability of $\text{Na}_4\text{Fe}_3(\text{PO}_4)_2(\text{P}_2\text{O}_7)/\text{NaTi}_2(\text{PO}_4)_3$ full-cell cycled at 1C in different aqueous electrolytes: 1 m NaClO_4 , 9.26 m NaCF_3SO_3 , and 17 m NaClO_4 . (b) Galvanostatic charge/discharge profiles of a $\text{Na}_4\text{Fe}_3(\text{PO}_4)_2(\text{P}_2\text{O}_7)/\text{NaTi}_2(\text{PO}_4)_3$ full-cell in 9.26 m NaCF_3SO_3 electrolyte at 1C. (c) Coulombic efficiency of a $\text{Na}_4\text{Fe}_3(\text{PO}_4)_2(\text{P}_2\text{O}_7)/\text{NaTi}_2(\text{PO}_4)_3$ full-cell cycled at 1C in different aqueous electrolytes: 1 m NaClO_4 , 9.26 m NaCF_3SO_3 , and 17 m NaClO_4 .

(d) Rate performance of the $\text{Na}_4\text{Fe}_3(\text{PO}_4)_2(\text{P}_2\text{O}_7)/\text{NaTi}_2(\text{PO}_4)_3$ full-cell in 17 m electrolyte at 0.2C, 1C, 5C, and 10C. The inset of (f) presents the cycle stability and coulombic efficiency of the full-cell in 17 m electrolyte at 5C. The voltage of the full-cell ranges between 0.01 and 2.0 V.....52

Figure 2.10. TEM analysis of a $\text{NaTi}_2(\text{PO}_4)_3$ anode surface. Low-magnification TEM images of (a) pristine $\text{NaTi}_2(\text{PO}_4)_3$ and $\text{NaTi}_2(\text{PO}_4)_3$ after 20 cycles in (c) 1 m and (e) 17 m NaClO_4 electrolytes at 1C. (b), (d), and (f) high-magnification TEM images of (a), (c), and (e), respectively. (g) High-resolution TEM images of a $\text{NaTi}_2(\text{PO}_4)_3$ surface after 20 cycles in 9.26 m NaCF_3SO_3 . (h) Magnified image (from boxed region in (a)) of SEI layer on a $\text{NaTi}_2(\text{PO}_4)_3$ anode surface.....57

Figure 2.11. (a) High-resolution TEM images and corresponding elemental EELS maps showing (c) carbon K-edge and (d) oxygen K-edge of $\text{NaTi}_2(\text{PO}_4)_3$ surface after 20 cycles in 1 m NaClO_4 electrolyte. (b) High-resolution TEM images and corresponding elemental EELS maps of (e) carbon K-edge and (f) oxygen K-edge of $\text{NaTi}_2(\text{PO}_4)_3$ surface after 20 cycles in 17 m NaClO_4 electrolyte.....58

Figure 2.12. EELS spectra of Cl L-edge for surface of the $\text{NaTi}_2(\text{PO}_4)_3$ electrode cycled in 17 m NaClO_4 and for reference NaCl powder. No signals from salt decomposition (i.e., Cl of NaClO_4) were detected on the electrodes cycled in the 17 m NaClO_4 electrolyte. The peak at 284 eV belongs to the carbon K-edge....59

Figure 2.13. XPS profile of (a) O 1s spectra, (b) Na 1s spectra, and (c) Cl 2p spectra of the $\text{NaTi}_2(\text{PO}_4)_3$ electrode before and after 20 cycles in 1 m and 17 m NaClO_4

electrolyte. (d) Carbon K-edge and (e) oxygen K-edge of sXAS spectra of pristine $\text{NaTi}_2(\text{PO}_4)_3$ electrode, first charged electrode, and electrode charged after 5 cycles and reference Na_2CO_360

Figure 2.14. (a) Thickness changes of surface layer on $\text{NaTi}_2(\text{PO}_4)_3$ electrode cycled in 17 m NaClO_4 electrolyte before and after DI water washing. High-resolution TEM images of the surface of $\text{NaTi}_2(\text{PO}_4)_3$ electrode cycled in 17 m NaClO_4 electrolyte, (b) before and (c) after DI water washing. (d) Voltage decay curve of a $\text{Na}_4\text{Fe}_3(\text{PO}_4)_2(\text{P}_2\text{O}_7)/\text{NaTi}_2(\text{PO}_4)_3$ full-cell after full charge (SOC 100) measured at 25 °C. Before obtaining the voltage decay curve, the full-cell was cycled 20 times at 1C in different aqueous electrolytes: 1 m NaClO_4 , 9.26 m NaCF_3SO_3 , and 17 m NaClO_4 , as shown in the graph.....64

Figure 2.15. Mechanism of the surface layer formation on the $\text{NaTi}_2(\text{PO}_4)_3$ anode comparing within 1 m and 17 m NaClO_4 aqueous electrolyte.....65

Figure 3.1. (a) Schematic illustrations of molecular structures of DMPZ. (b), Charge-discharge curves of DMPZ for 15 cycles in triglyme (TEGDME) electrolyte cycled in the voltage range of 2.2-4 V vs. Na/Na^+ at 1C ($1\text{C} = 255 \text{ mA g}^{-1}$)...93

Figure 3.2. (a) Relative solubility of DMPZ calculated by machine learning comparing within generic battery electrolyte solvents. (b) Experimental solubility of DMPZ in TEGDME and aqueous solutions. (c) Dissolution behavior of DMPZ in

DMC and PC solutions. DMPZ easily dissolved in DMC solution even over the high-concentration of 0.1 M, which coincident with the solubility prediction in (a). 0.02 M of DMPZ dissolved in PC solution, but ~ 0.1 M of DMPZ was not fully dissolved in PC and DMPZ powder was floating in the solution.....94

Figure 3.3. Galvanostatic charge-discharge profiles of the DMPZ in 1 m NaClO₄ according to (a) half charge and (b) full charge. The inset of (a) present the cycle stability of DMPZ at 1C. The inset of (b) presents the comparison of capacity retention in DMPZ according to half charge and full charge.....95

Figure 3.4. (a) Schematic illustrations of the strategy for perfectly drawing out the performance of DMPZ. (b) The charge–discharge profiles of DMPZ for the initial 5 cycles. (c) Comparison of redox potential in dQ/dV curves of DMPZ cycled in 1 and 17 m NaClO₄ aqueous electrolytes. The inset of (c) shows the redox potential dependency on the salt concentration.....105

Figure 3.5. (a) Dissolution behaviors of DMPZ electrodes, especially the DMPZ⁺ and DMPZ²⁺ states and comparison of that between in non-aqueous electrolyte, 1 and 17 m NaClO₄ aqueous electrolyte. The inset pictures in (a) show the collected solutions at the DMPZ⁺ and DMPZ²⁺ state in each electrolyte. (b) UV-vis spectroscopy of retrieved solutions after soaking the cycled DMPZ electrode in each electrolyte. The upper part of (b) presents the absorbance spectrum of DMPZ⁺ state solutions and the lower part of (b) presents the UV-vis spectra of DMPZ²⁺ state solutions.....106

Figure 3.6. (a) Relative dissolution quantity of DMPZ for non-aqueous electrolyte, 1 m NaClO₄ aqueous, and 17 m NaClO₄ aqueous electrolytes at each charged state of DMPZ (DMPZ⁺ and DMPZ²⁺, respectively). The relative dissolution quantity of the DMPZ in comparing each electrolyte was obtained from the area of the absorbance spectrum which indicates the dissolution amount of the DMPZ⁺ and DMPZ²⁺ in Figure 3.5b. (b) The corresponding weight changes of the DMPZ electrode at different SOC after the dissolution in each electrolyte.....107

Figure 3.7. GITT profiles of the DMPZ in 17 m NaClO₄ aqueous electrolyte at 1C rate with 2 hours of rest time during initial and second charge-discharge process111

Figure 3.8. Morphology of DMPZ powder and electrode. SEM images of (a) pristine DMPZ powder and (b) Before roll-press the DMPZ electrode. This electrode was mixed only with DMPZ powder and binder (PTFE), then cast on the c-Ti foil. (c and d) Surface morphology of the electrode after the roll-press process. (c) low- and (d) high-magnification of the roll-pressed DMPZ electrode.....112

Figure 3.9. Surface morphology of the DMPZ pristine electrode and ex-situ electrode after the first cycle in 1 M NaClO₄ TEGDME electrolyte. (a, c, and e) SEM images of (a) pristine DMPZ electrode, and (c) first charged, (e) discharged DMPZ in 1 M NaClO₄ TEGDME electrolyte. (b), (d), and (e) presents the magnified SEM images of (a), (c), and (e), respectively.....113

Figure 3.10. Surface morphology of the DMPZ electrode during the first cycle in 17

m NaClO₄ aqueous electrolyte (a and c) SEM images of DMPZ electrode after (a) first charged and (c) first discharged. (b) and (d) presents the magnified SEM images of (a) and (c), respectively.....114

Figure 3.11. Rate performance of DMPZ cell at 0.2C, 0.5C, 1C, 2C, 4C, and 5C

.....117

Figure 3.12. Rate performance of DMPZ cell at 0.2C, 0.5C, 1C, 2C, 4C, and 5C.

Rate performance of DMPZ in 17 m aqueous electrolyte. (a) Discharge profiles of the DMPZ in 17 m aqueous electrolyte at 0.2C, 0.5C, 1C, 2C, 4C, and 5C. (b) Cycle stability and coulombic efficiency of the DMPZ in 17 m aqueous electrolyte at 5C

.....118

Figure 3.13. Cycle stability of DMPZ cell at 0.2C rate.....119

Figure 3.14. Cycle stability of DMPZ cell at 1C rate.....120

Figure 3.15. Structural analysis of the DMPZ after long-term cycling. (a) Charge-discharge profile changes of the DMPZ in 17 m aqueous electrolyte during 1 to 100 cycles. (b) Charge-discharge curves of the DMPZ in 17 m aqueous electrolyte during 100 to 1000 cycles.....125

Figure 3.16. (a) Ex-situ XRD patterns of pristine, 1-, 50-, and 100-cycled DMPZ at the charged, discharged state of each cycle. **(b)** Schematic illustrations of crystal structures of DMPZ. The structural information of DMPZ has been adopted from CCDC (Cambridge Crystallographic Data Centre, www.ccdc.cam.ac.uk), whose

detailed information is provided in the reference 74-75. (c) XPS profiles of N 1s spectra of DMPZ pristine and electrode after 1-, 50-, and 100-cycled at charged, discharged state of each cycle. Black arrow lines indicate the reversible reaction at redox center N of C-N-C groups in DMPZ. The green arrow line indicates the C-N-C satellite peak, which also indicates reversible redox reactions at redox center N of DMPZ.....126

Figure 3.17. Surface morphologies of the DMPZ electrode after long-term cycling in 17 m aqueous electrolyte. a, c, e, g, SEM images of DMPZ electrode after (a) 50 cycle charged, (c) 50 cycle discharged, (e) 100 cycle charged, and (g) 100 cycle discharged. (b), (d), (f), and (h) presents the magnified SEM images of (a), (c), (e), and (g), respectively.....127

Figure 3.18. Comparison of performance of DMPZ aqueous battery with that of previously demonstrated organic-based aqueous battery system. This plot summarizes the energy density (*i.e.*, initial discharge-capacity-based energy density of each battery system, z-axis), cycle degradation rate per day (x-axis), and calculated battery operational life (y-axis) based on the cumulative discharge capacity from recently reported works (see Table 3.2 and Chapter 3.3.7 for the calculation details of the battery operational life, degradation rate per day, and detailed references with abbreviations for each material).....135

Chapter 1. Introduction

1.1 Research motivation and objectives

With the ever-increasing carbon dioxide gas levels in the atmosphere by using of fossil fuel combustion for producing large-scale of electricity, which causing a greenhouse effect with global warming, rechargeable batteries have received extensive attention for use in grid-scale energy storage systems (ESSs) owing to their high energy density, compactness, versatility, low maintenance, and high round-trip efficiency¹⁻³. The surging requirements for the eco-friendly and sustainable energy storage systems have significantly boosted and advanced the mass production of the rechargeable lithium-ion batteries (LIBs) in the current energy market⁴⁻⁶. Although the LIBs lie in the frontline deployment for green energy technologies, it still poses many hurdles to be addressed for large-scale energy storage application such as the high-cost from limited resources and intrinsic safety issues^{4,7-9}. The conventional cathodes of LIBs rely on the electrode chemistry based on heavy transition-metals (TM), and it is clear that the limited resources continuously bring about the cost issues¹⁰⁻¹². Moreover, limited design versatility and reaching theoretical capacity have retarded further advances for greener and sustainable energy storage in grid-scale energy market. Thus, despite the promising outlook for conventional lithium-ion batteries, many obstacles to their use for such large-scale applications have yet to be overcome, including rising costs stemming from the limited abundance of raw materials and safety concerns arising from the use of highly flammable organic

electrolytes^{7,8,13-16}.

As an alternative safer chemistry, the batteries that employ aqueous electrolytes or solid-state electrolyte have been investigated owing to their non-flammability. However, the solid-state electrolyte also has lots of obstacles to their use for practical large-scale applications due to its low ionic conductivity, surface degradation, and high-cost. Therefore, the aqueous electrolyte system more attractive for large-scale energy storage system owing to their non-toxicity and low-cost with non-flammability. However, traditional aqueous electrolytes provide a narrow electrochemical stability window of ~ 1.23 V; thermodynamic water decomposition, such as hydrogen and oxygen evolution, occurs outside this window. This narrow stability window inevitably serves as a bottleneck for the selection of electrode materials, yielding limited energy density for aqueous systems, which make them unfit for practical application^{15,17-19}.

The aim of this research is to develop low-cost and sustainable aqueous battery with high-energy density by addressing limitations induced by narrow electrochemical stability nature of water. Main strategy is to drive a new low-cost aqueous battery system by introducing high-concentration aqueous electrolyte.

1.2 Introduction to aqueous battery

From the first beginning of the aqueous battery in 1994 by Dahn and co-workers, water has been considered as an electrolyte for large-scale energy storage²⁰⁻²². The aqueous electrolytes are promising alternatives from the use of highly flammable organic ones, owing to their non-flammable safe chemistry, non-toxicity, and low-cost^{13,15,17,18,23,24}. The successful working of aqueous system necessitates various electrolyte properties such as high ionic conductivity, chemical and electrochemical stability, safety, low-cost, and environmental beingness, which are common for both aqueous and non-aqueous electrolytes^{15,18,24}. However, since aqueous electrolyte particularly suffers from strictly narrow electrochemical stability window despite other potential advantages, pushing the limits of cathodic and anodic stability against HER and OER, respectively, has been a major concern of the fields. While suitable electrode design could, to some extent, retard the HER or OER, for such a performance improvement in a given cell configuration, the feasibly tunable components in aqueous electrolyte itself are the type and concentration of salts (or solutes). Therefore, the research efforts on an aqueous electrolyte have generally been related to the optimizations of utilizing conditions of salts and discoveries of new salts.

In regards to the classical aqueous electrolyte, most researches were placed on identifying the compatible electrode chemistry for aqueous electrolytes^{15,18}. Nevertheless, there have been noteworthy results concerning the optimizations of the aqueous electrolytes with respect to salt species and the pH to improve the kinetics

and tailor the HER and OER limit. In conventional systems, the most commonly selected salts include inorganics such as sulfate (SO_4^{2-}), nitrate (NO_3^-), chloride (Cl^-), hydroxide (OH^-), and perchlorate (ClO_4^-) due to their low cost and decent electrochemical properties^{15,24-28}. A few studies have reported organic salts, most of which addressed lithium bis(trifluoromethane sulfonyl)imide (LiTFSI)²⁹⁻³¹. To leverage the effect of cations in conjunction with that of salt anions, W. Zuo *et al.* systematically evaluated the electrochemical kinetics and found that the hydration energy of cations and anions plays an important role in determining the kinetics of the electrochemical system. In the study, series of aqueous cells were constructed employing Li^+ , Na^+ , K^+ , Mg^{2+} , Ca^{2+} , Sr^{2+} , Ba^{2+} , and Al^{3+} for cations and Cl^- , NO_3^- , and SO_4^{2-} for anions, respectively³². They observed a clear linear correlation between the hydration energy of ions and the overpotential observed for the cell. It was speculated that stronger ionic hydration energy of cations and anions are beneficial for the fast-redox reactions, possibly because a stronger binding between water and ions makes a more favorable chemical environment to the redox of electrodes.

The pH value of aqueous electrolyte has also served as a tool to regulate the relative spontaneity of HER and OER to improve the stability of the system. In principle, the decrease of proton activity (*i.e.* pH increases) lowers the HER and OER potential concomitantly. Therefore, the potential of voltage window determined from pH value has been used as a guideline for selecting viable electrode materials, and some works have attempted to stabilize the interfacial reactions at the electrode by tailoring pH value to allow voltage window to encompass the redox potential of the

electrode^{21,22,33-40}. To widen cathodic and anodic limit simultaneously, Chen *et al.* applied different pH conditions for aqueous electrolytes at the positive and negative electrode side, respectively³⁹. To this end, a ceramic Li-ion exchange membrane ($\text{Li}_{1+x+y}\text{Al}_x\text{Ti}_{2-x}\text{Si}_y\text{P}_{3-y}\text{O}_{12}$) was inserted in the electrolyte to separate the acidic electrolyte at the cathode side and the alkaline electrolyte at the anode side. As a consequence of increased OER potential and decreased OER potential, a wide voltage window (~ 3 V) were obtained for a Zn/KMnO₄ aqueous cell. However, the use of Li-ion exchange membrane can lead to the other limitations related with ionic conductivity and the stability of ceramic membrane, and without this electrolyte separation, the gap between OER and HER is fixed to 1.23 V irrespective pH value. In addition, even at the strongly alkaline conditions (pH=14), the cathodic limit still remains 2.213 V vs. Li.⁴¹, implying that the adjustment of pH is only marginally effective⁴². Besides pH conditions of aqueous electrolyte, the presence of gaseous species dissolved was found to exhibit a significant effect on the stability of the system. Residual O₂ or CO₂ in the aqueous electrolyte could trigger side reactions on the surface of the anode during the discharge process involving water molecules, severely deteriorating the cycling capability of the electrochemical cell⁴³.

Ever since the pioneering work by Li *et al.* reported the stable electrochemical performances of lithium aqueous batteries exploiting 5 M LiNO₃ + 0.001 M LiOH aqueous electrolyte and intercalation compounds, many researchers have dedicated to understanding the working mechanism of concentrated salt electrolytes^{20-22,44}. While intercalation compounds were generally unstable in pure water, it could be

stabilized in an aqueous system containing concentrated lithium salts, since the chemical potential of lithium in solution increases with the concentrations. More systematic studies on the effect of the concentrations were carried out by Yushin group^{45,46}. They attempted to precisely examine the compatibility of LiNO_3 and Li_2SO_4 based aqueous electrolytes with typical cathodes such as LiFePO_4 ⁴⁵ and LiCoO_2 ⁴⁶. Interestingly, for both electrodes, the more improved capacity retention was obtained with the concentration increase, representing the optimal properties at the respective saturation points. Authors suggested that a higher concentration leads to a less amount of free water molecules, thereby more effectively suppressing the parasitic reactions between free water and electrode interfaces. This implies the presence of an optimum salt concentration for aqueous electrolyte, which contrasts with conventional non-aqueous electrolyte, where the optimum value has been regarded near 1.0 M ($\text{M} = \text{mol L}^{-1}$) because of the highest ionic conductivity at this point¹³. In the case of aqueous electrolyte whose primary bottleneck lies in the poor cycling stability rather than ionic conductivity, the high concentration that aided in the stability enhancement could have been more desirable despite the reduced ionic conductivity arising from relatively high viscosity. Indeed, recent theoretical investigation proposed the mechanism by which above a certain concentration, the aqueous electrolyte can attain a decent overall ionic conductivity irrespective of the viscosity, supporting the necessity of higher concentration of aqueous electrolyte for better performance⁴⁷.

1.3 Emerging the super-concentrated aqueous electrolyte for high-energy density aqueous battery system

Recently, highly concentrated electrolytes have emerged as a potential game changer in the battery market for both aqueous and non-aqueous systems because of their remarkable characteristics, which are distinct from those of conventional electrolyte systems, including low flammability, low solvent activity, and high chemical stability that suppress side reactions^{19,48-65}. The works on “water-in-salt” electrolyte (WiSE) by Xu group have opened a new avenue toward the high-concentration aqueous electrolytes with the remarkably expanded electrochemical window^{52,55,57,64,66}. Series of studies regarding WiSE showed that it benefits from (i) the formation of anion-derived passivation films (or SEI layer) at the anode interfaces and (ii) water solvation structure, retarding the HER and OER, respectively^{67,68}. It was claimed that, to obtain sufficient protection from the SEI layer, WiSE should meet two prerequisites⁴¹. First, during the SEI formation, salt anions are predominantly decomposed in competitions with water molecules and gas species. Second, the formed SEI should be sufficiently dense and chemically/electrochemically stable in the electrolyte to maintain its protective role. Mechanistic investigations revealed that what is essential in satisfying both requirements are the ‘super-concentration’ condition itself^{41,52}. In this respect, many following works have considered the saturation points of salts as a primary criterion of salt selection, and have explored highly soluble salts such as LiTFSI, lithium trifluoromethane sulfonate (LiOTf), and lithium bis(pentafluoroethane

sulfonyl)imide (LiBETI) for WiSE^{52,57,66}. These findings have also invoked the extensive research efforts to identify the viable positive electrodes^{53,56,60}, negative electrodes^{58,60}, and current collectors for the given WiSE^{54,66}. In the similar context, two major determinants of solubility were often considered for the search of new salts with higher solubility; the lattice energy required to dissociate salts, and energy gains upon hydration of ions⁶⁹. For example, compared with NaTFSI salts, sodium bis(fluorosulfonyl)imide (NaFSI) whose lattice and hydration energies were predicted be lower and higher, respectively, could exhibit remarkably increased maximum solubility⁶⁹. Meanwhile, the mixing of two distinct salts could also be an effective strategy to increase the overall concentration because it was found that a saturated electrolyte could still dissolve another unhydrated salt with similar chemical structures. In this regard, Suo *et al.* dissolved two salts with similar fluorinated structures up to their respective saturation points (7m LiOTf and 21 m LiTFSI) to form “water-in-bisalt” electrolyte with 28 m Li⁺⁵⁷. In a similar vein, Yamada *et al.* introduced the concept of hydrate-melt electrolyte exemplifying Li(TFSI)_{0.7}(BETI)_{0.3} · 2H₂O electrolyte⁶⁶. The hydrate-melt electrolyte indicates the eutectic molten salt which contains the negligible amount of free water molecules because of low water concentration but retains fluidity benefiting from the exploration of eutectic systems.

1.4 Purpose of this research

Despite the validations of WiSE systems with the widened electrochemical window, their real-world deployment has been delayed by the excessive use of expensive and toxic organic imide salts (*eg.* LiTFSI), which inevitably compromises the original merits of the aqueous system^{62,70,71}. Therefore, the discovery of low-cost salts has been of recent interest of many researchers. Moreover, the demands of the greener and more sustainable aqueous battery system with high-energy density was increased. Thus, sustainable and low-cost aqueous battery system with high-energy density should to be investigated.

Chapter 2 unveiled that the high-concentrated NaClO₄ aqueous electrolyte is a promising candidate for a low-cost high-voltage sodium aqueous electrolyte. This study comprehensively revisited the applicability of low-cost salts such as SO₄²⁻, NO₃⁻, and ClO₄⁻ for both Li- and Na- high-concentration aqueous systems. The overall trend of solubility was found to be identical with the prediction based on Hofmeister series^{71,72}, which ranks the water solvation strength of solutes. Among the candidate salts, NaClO₄ was identified as the most soluble and effective salts. Unlike the conventional WiSE systems, it was observed that a stable SEI layer was formed, which is composed of a reduction compound of dissolved gases during the electrochemical cycling, not from byproducts of anion salt decomposition, suggesting an alternative route to stabilize the electrode against HER. It was proposed that the high-concentration of NaClO₄ aids in preventing the dissolution of the SEI layer by reducing the presence of free water.

Chapter 3 suggest novel approaches to facilitate the complete utilization of the capacity and drastically improve the cycle durability by employing an electrolyte that is the most compatible with a DMPZ electrode. For fully utilizing the DMPZ electrode, high-concentration aqueous electrolyte (NaClO_4) strategy was applied to further suppress the dissolution and water decomposition, thereby achieving significantly improved capacity retention of $\sim 87\%$ over 200 cycles (over 1,000 hours) at 0.2C with a discharge capacity of 231 mAh g^{-1} . Even after 1,000 cycles at 1C (over 1,630 hours), outstanding long-life durability with a cycle degradation rate of below 0.5% per day is achieved, corresponding to a capacity retention of $\sim 81\%$, with a discharge capacity of 221 mAh g^{-1} .

The findings in this research on the new inorganic solutes suitable for the high-concentration aqueous electrolytes broaden our understanding on this new class of electrolyte systems and provide important guidance for the realization of low-cost high-voltage aqueous batteries. Moreover, understandings of the compatibility between ROMs and electrolytes is a key factor toward the successful implementation of rechargeable organic aqueous batteries with high-energy density and long cycle life

1.5 References

1. Huggins, R. *Advanced Batteries: Materials Science Aspects*. (Springer US, 2008).
2. Liu, C., Li, F., Ma, L.-P. & Cheng, H.-M. Advanced Materials for Energy Storage. *Advanced Materials* **22**, E28-E62, doi:doi:10.1002/adma.200903328 (2010).
3. Dunn, B., Kamath, H. & Tarascon, J.-M. Electrical Energy Storage for the Grid: A Battery of Choices. *Science* **334**, 928, doi:10.1126/science.1212741 (2011).
4. Vikström, H., Davidsson, S. & Höök, M. Lithium availability and future production outlooks. *Applied Energy* **110**, 252-266, doi:https://doi.org/10.1016/j.apenergy.2013.04.005 (2013).
5. Larcher, D. & Tarascon, J. M. Towards greener and more sustainable batteries for electrical energy storage. *Nature Chemistry* **7**, 19, doi:10.1038/nchem.2085 (2014).
6. Winter, M., Barnett, B. & Xu, K. Before Li Ion Batteries. *Chemical Reviews* **118**, 11433-11456, doi:10.1021/acs.chemrev.8b00422 (2018).

7. Choi, N.-S. *et al.* Challenges Facing Lithium Batteries and Electrical Double-Layer Capacitors. *Angewandte Chemie International Edition* **51**, 9994-10024, doi:<https://doi.org/10.1002/anie.201201429> (2012).
8. Kalhoff, J., Eshetu, G. G., Bresser, D. & Passerini, S. Safer Electrolytes for Lithium-Ion Batteries: State of the Art and Perspectives. *ChemSusChem* **8**, 2154-2175, doi:<https://doi.org/10.1002/cssc.201500284> (2015).
9. Sharma, S. S. & Manthiram, A. Towards more environmentally and socially responsible batteries. *Energy & Environmental Science* **13**, 4087-4097, doi:10.1039/D0EE02511A (2020).
10. Armand, M. & Tarascon, J. M. Building better batteries. *Nature* **451**, 652-657, doi:10.1038/451652a (2008).
11. Larcher, D. & Tarascon, J. M. Towards greener and more sustainable batteries for electrical energy storage. *Nature Chemistry* **7**, 19-29, doi:10.1038/nchem.2085 (2015).
12. Lewis, N. S. Research opportunities to advance solar energy utilization. *Science* **351**, aad1920, doi:10.1126/science.aad1920 (2016).
13. Xu, K. Nonaqueous Liquid Electrolytes for Lithium-Based Rechargeable

- Batteries. *Chemical Reviews* **104**, 4303-4418, doi:10.1021/cr030203g (2004).
14. Roth, E. P. & Orendorff, C. J. How Electrolytes Influence Battery Safety. *The Electrochemical Society Interface* **21**, 45-49, doi:10.1149/2.F04122if (2012).
15. Kim, H. *et al.* Aqueous Rechargeable Li and Na Ion Batteries. *Chemical Reviews* **114**, 11788-11827, doi:10.1021/cr500232y (2014).
16. Kim, H. *et al.* Recent Progress in Electrode Materials for Sodium-Ion Batteries. *Advanced Energy Materials* **6**, 1600943, doi:doi:10.1002/aenm.201600943 (2016).
17. Tang, W. *et al.* Aqueous rechargeable lithium batteries as an energy storage system of superfast charging. *Energy & Environmental Science* **6**, 2093-2104, doi:10.1039/C3EE24249H (2013).
18. Bin, D. *et al.* Progress in Aqueous Rechargeable Sodium-Ion Batteries. *Advanced Energy Materials* **8**, 1703008, doi:doi:10.1002/aenm.201703008 (2018).
19. Jiao, S. *et al.* Stable cycling of high-voltage lithium metal batteries in ether

- electrolytes. *Nature Energy* **3**, 739-746, doi:10.1038/s41560-018-0199-8 (2018).
20. Li, W., Dahn, J. R. & Wainwright, D. S. Rechargeable Lithium Batteries with Aqueous Electrolytes. *Science* **264**, 1115, doi:10.1126/science.264.5162.1115 (1994).
21. Li, W., McKinnon, W. R. & Dahn, J. R. Lithium Intercalation from Aqueous Solutions. *Journal of The Electrochemical Society* **141**, 2310-2316, doi:10.1149/1.2055118 (1994).
22. Li, W. & Dahn, J. R. Lithium-Ion Cells with Aqueous Electrolytes. *Journal of The Electrochemical Society* **142**, 1742-1746, doi:10.1149/1.2044187 (1995).
23. Wang, Y., Yi, J. & Xia, Y. Recent Progress in Aqueous Lithium-Ion Batteries. *Advanced Energy Materials* **2**, 830-840, doi:10.1002/aenm.201200065 (2012).
24. Eftekhari, A. High-Energy Aqueous Lithium Batteries. *Advanced Energy Materials* **8**, 1801156, doi:10.1002/aenm.201801156 (2018).
25. Zhang, Y. & Cremer, P. S. Interactions between macromolecules and ions:

- the Hofmeister series. *Current Opinion in Chemical Biology* **10**, 658-663, doi:<https://doi.org/10.1016/j.cbpa.2006.09.020> (2006).
26. Marcus, Y. Effect of Ions on the Structure of Water: Structure Making and Breaking. *Chemical Reviews* **109**, 1346-1370, doi:10.1021/cr8003828 (2009).
 27. Brini, E. *et al.* How Water's Properties Are Encoded in Its Molecular Structure and Energies. *Chemical Reviews* **117**, 12385-12414, doi:10.1021/acs.chemrev.7b00259 (2017).
 28. Huang, J. *et al.* Recent Progress of Rechargeable Batteries Using Mild Aqueous Electrolytes. *Small Methods* **3**, 1800272, doi:10.1002/smt.201800272 (2019).
 29. Salomon, M. Conductance of solutions of lithium bis(trifluoromethanesulfone)imide in water, propylene carbonate, acetonitrile and methyl formate at 25°C. *Journal of Solution Chemistry* **22**, 715-725, doi:10.1007/BF00647411 (1993).
 30. Perron, G., Brouillette, D. & Desnoyers, J. E. Comparison of the thermodynamic and transport properties of lithium bis(trifluoromethylsulfonyl)imide (LiTFSI) with LiClO₄ and Bu₄NBr in

water at 25 °C. *Canadian Journal of Chemistry* **75**, 1608-1614, doi:10.1139/v97-191 (1997).

31. Lux, S. F. *et al.* LiTFSI Stability in Water and Its Possible Use in Aqueous Lithium-Ion Batteries: pH Dependency, Electrochemical Window and Temperature Stability. *Journal of The Electrochemical Society* **160**, A1694-A1700 (2013).
32. Zuo, W. *et al.* Bismuth oxide: a versatile high-capacity electrode material for rechargeable aqueous metal-ion batteries. *Energy & Environmental Science* **9**, 2881-2891, doi:10.1039/C6EE01871H (2016).
33. Pei, W., Hui, Y. & Huaquan, Y. Electrochemical behavior of Li Mn spinel electrode material in aqueous solution. *Journal of Power Sources* **63**, 275-278, doi:https://doi.org/10.1016/S0378-7753(96)02477-9 (1996).
34. Zhang, M. & Dahn, J. R. Electrochemical Lithium Intercalation in VO₂(B) in Aqueous Electrolytes. *Journal of The Electrochemical Society* **143**, 2730-2735, doi:10.1149/1.1837099 (1996).
35. Khomenko, V., Raymundo-Piñero, E. & Béguin, F. Optimisation of an asymmetric manganese oxide/activated carbon capacitor working at 2V in aqueous medium. *Journal of Power Sources* **153**, 183-190,

doi:<https://doi.org/10.1016/j.jpowsour.2005.03.210> (2006).

36. Wang, Y.-g., Luo, J.-y., Wang, C.-x. & Xia, Y.-y. Hybrid Aqueous Energy Storage Cells Using Activated Carbon and Lithium-Ion Intercalated Compounds: II. Comparison of $\text{Li Mn}_2\text{O}_4$, $\text{Li Co}_{1/3}\text{Ni}_{1/3}\text{Mn}_{1/3}\text{O}_2$, and Li Co O_2 Positive Electrodes. *Journal of The Electrochemical Society* **153**, A1425-A1431, doi:[10.1149/1.2203772](https://doi.org/10.1149/1.2203772) (2006).
37. Bichat, M. P., Raymundo-Piñero, E. & Béguin, F. High voltage supercapacitor built with seaweed carbons in neutral aqueous electrolyte. *Carbon* **48**, 4351-4361, doi:<https://doi.org/10.1016/j.carbon.2010.07.049> (2010).
38. Yang, X., He, Y.-S., Jiang, G., Liao, X.-Z. & Ma, Z.-F. High voltage supercapacitors using hydrated graphene film in a neutral aqueous electrolyte. *Electrochemistry Communications* **13**, 1166-1169, doi:<https://doi.org/10.1016/j.elecom.2011.09.006> (2011).
39. Chen, L., Guo, Z., Xia, Y. & Wang, Y. High-voltage aqueous battery approaching 3 V using an acidic–alkaline double electrolyte. *Chemical Communications* **49**, 2204-2206, doi:[10.1039/C3CC00064H](https://doi.org/10.1039/C3CC00064H) (2013).
40. Yu, J. *et al.* Development of High-Voltage Aqueous Electrochemical Energy

- Storage Devices. *Advanced Materials Interfaces* **4**, 1700279, doi:10.1002/admi.201700279 (2017).
41. Suo, L. *et al.* How Solid-Electrolyte Interphase Forms in Aqueous Electrolytes. *Journal of the American Chemical Society* **139**, 18670-18680, doi:10.1021/jacs.7b10688 (2017).
 42. Wessells, C., Ruffo, R., Huggins, R. A. & Cui, Y. Investigations of the Electrochemical Stability of Aqueous Electrolytes for Lithium Battery Applications. *Electrochemical and Solid-State Letters* **13**, A59-A61 (2010).
 43. Luo, J.-Y., Cui, W.-J., He, P. & Xia, Y.-Y. Raising the cycling stability of aqueous lithium-ion batteries by eliminating oxygen in the electrolyte. *Nature Chemistry* **2**, 760, doi:10.1038/nchem.763, <https://www.nature.com/articles/nchem.763#supplementary-information> (2010).
 44. Zhao, M., Huang, G., Qu, F., Wang, F. & Song, X. Electrochemical performances of (LiMn_{0.6}Fe_{0.4}PO₄/C)//LiV₃O₈ in different aqueous solution electrolyte. *Electrochimica Acta* **151**, 50-55, doi:<https://doi.org/10.1016/j.electacta.2014.10.148> (2015).
 45. Gordon, D. *et al.* Enhancing Cycle Stability of Lithium Iron Phosphate in

- Aqueous Electrolytes by Increasing Electrolyte Molarity. *Advanced Energy Materials* **6**, 1501805, doi:10.1002/aenm.201501805 (2016).
46. Ramanujapuram, A. *et al.* Degradation and stabilization of lithium cobalt oxide in aqueous electrolytes. *Energy & Environmental Science* **9**, 1841-1848, doi:10.1039/C6EE00093B (2016).
47. Borodin, O. *et al.* Liquid Structure with Nano-Heterogeneity Promotes Cationic Transport in Concentrated Electrolytes. *ACS Nano* **11**, 10462-10471, doi:10.1021/acsnano.7b05664 (2017).
48. Suo, L., Hu, Y.-S., Li, H., Armand, M. & Chen, L. A new class of Solvent-in-Salt electrolyte for high-energy rechargeable metallic lithium batteries. *Nature Communications* **4**, 1481, doi:10.1038/ncomms2513, <https://www.nature.com/articles/ncomms2513#supplementary-information> (2013).
49. Wang, J. *et al.* Superconcentrated electrolytes for a high-voltage lithium-ion battery. *Nature Communications* **7**, 12032, doi:10.1038/ncomms12032, <https://www.nature.com/articles/ncomms12032#supplementary-information> (2016).
50. Chen, S. *et al.* High-Voltage Lithium-Metal Batteries Enabled by Localized High-Concentration Electrolytes. *Advanced Materials* **30**, 1706102,

doi:10.1002/adma.201706102 (2018).

51. Wang, J. *et al.* Fire-extinguishing organic electrolytes for safe batteries. *Nature Energy* **3**, 22-29, doi:10.1038/s41560-017-0033-8 (2018).
52. Suo, L. *et al.* “Water-in-salt” electrolyte enables high-voltage aqueous lithium-ion chemistries. *Science* **350**, 938, doi:10.1126/science.aab1595 (2015).
53. Gambou-Bosca, A. & Bélanger, D. Electrochemical characterization of MnO₂-based composite in the presence of salt-in-water and water-in-salt electrolytes as electrode for electrochemical capacitors. *Journal of Power Sources* **326**, 595-603, doi:https://doi.org/10.1016/j.jpowsour.2016.04.088 (2016).
54. Kühnel, R. S. *et al.* “Water-in-salt” electrolytes enable the use of cost-effective aluminum current collectors for aqueous high-voltage batteries. *Chemical Communications* **52**, 10435-10438, doi:10.1039/C6CC03969C (2016).
55. Suo, L. *et al.* Advanced High-Voltage Aqueous Lithium-Ion Battery Enabled by “Water-in-Bisalt” Electrolyte. *Angewandte Chemie International Edition* **55**, 7136-7141, doi:10.1002/anie.201602397 (2016).

56. Suo, L. *et al.* “Water-in-Salt” electrolytes enable green and safe Li-ion batteries for large scale electric energy storage applications. *Journal of Materials Chemistry A* **4**, 6639-6644, doi:10.1039/C6TA00451B (2016).
57. Wang, F. *et al.* Stabilizing high voltage LiCoO₂ cathode in aqueous electrolyte with interphase-forming additive. *Energy & Environmental Science* **9**, 3666-3673, doi:10.1039/C6EE02604D (2016).
58. Sun, W. *et al.* “Water-in-Salt” electrolyte enabled LiMn₂O₄/TiS₂ Lithium-ion batteries. *Electrochemistry Communications* **82**, 71-74, doi:https://doi.org/10.1016/j.elecom.2017.07.016 (2017).
59. Vatamanu, J. & Borodin, O. Ramifications of Water-in-Salt Interfacial Structure at Charged Electrodes for Electrolyte Electrochemical Stability. *The Journal of Physical Chemistry Letters* **8**, 4362-4367, doi:10.1021/acs.jpcclett.7b01879 (2017).
60. Yang, C. *et al.* Flexible Aqueous Li-Ion Battery with High Energy and Power Densities. *Advanced Materials* **29**, 1701972, doi:10.1002/adma.201701972 (2017).
61. Yang, C. *et al.* Unique aqueous Li-ion/sulfur chemistry with high energy density and reversibility. *Proceedings of the National Academy of Sciences*

- 114**, 6197, doi:10.1073/pnas.1703937114 (2017).
62. Lukatskaya, M. R. *et al.* Concentrated mixed cation acetate “water-in-salt” solutions as green and low-cost high voltage electrolytes for aqueous batteries. *Energy & Environmental Science* **11**, 2876-2883, doi:10.1039/C8EE00833G (2018).
63. Zheng, Q. *et al.* Sodium- and Potassium-Hydrate Melts Containing Asymmetric Imide Anions for High-Voltage Aqueous Batteries. *Angewandte Chemie International Edition* **58**, 14202-14207, doi:10.1002/anie.201908830 (2019).
64. Borodin, O., Self, J., Persson, K. A., Wang, C. & Xu, K. Uncharted Waters: Super-Concentrated Electrolytes. *Joule* **4**, 69-100, doi:https://doi.org/10.1016/j.joule.2019.12.007 (2020).
65. Xie, J., Liang, Z. & Lu, Y.-C. Molecular crowding electrolytes for high-voltage aqueous batteries. *Nature Materials*, doi:10.1038/s41563-020-0667-y (2020).
66. Yamada, Y. *et al.* Hydrate-melt electrolytes for high-energy-density aqueous batteries. *Nature Energy* **1**, 16129, doi:10.1038/nenergy.2016.129, <https://www.nature.com/articles/nenergy2016129#supplementary->

information (2016).

67. Dubouis, N. *et al.* The role of the hydrogen evolution reaction in the solid–electrolyte interphase formation mechanism for “Water-in-Salt” electrolytes. *Energy & Environmental Science* **11**, 3491-3499, doi:10.1039/C8EE02456A (2018).
68. Zheng, J. *et al.* Understanding Thermodynamic and Kinetic Contributions in Expanding the Stability Window of Aqueous Electrolytes. *Chem* **4**, 2872-2882, doi:https://doi.org/10.1016/j.chempr.2018.09.004 (2018).
69. Kühnel, R.-S., Reber, D. & Battaglia, C. A High-Voltage Aqueous Electrolyte for Sodium-Ion Batteries. *ACS Energy Letters* **2**, 2005-2006, doi:10.1021/acsenergylett.7b00623 (2017).
70. He, X. *et al.* Fluorine-free water-in-ionomer electrolytes for sustainable lithium-ion batteries. *Nature Communications* **9**, 5320, doi:10.1038/s41467-018-07331-6 (2018).
71. Lee, M. H. *et al.* Toward a low-cost high-voltage sodium aqueous rechargeable battery. *Materials Today*, doi:https://doi.org/10.1016/j.mattod.2019.02.004 (2019).

72. Hofmeister, F. Zur Lehre von der Wirkung der Salze. *Archiv für experimentelle Pathologie und Pharmakologie* **24**, 247-260, doi:10.1007/BF01918191 (1888).

Chapter 2. Toward a low-cost high-voltage sodium aqueous rechargeable battery

2.1 Research background

(The essence of this chapter has been published in *Materials Today*. Reproduced with permission from [Lee, M. H.[†] and Kim, S. J.[†] *et al.*, *Mater. Today* **2019**, 29, 26-36] Copyright (2019) Elsevier)

In continuously growing greener and sustainable energy demand, grid-scale energy storage systems (ESSs) using Lithium-ion batteries (LIBs) have received enormous attention over many years owing to their high energy density, compactness, versatility, low maintenance, and high round-trip efficiency¹⁻⁴. Despite its promising outlook, such a large-scale application has yet to overcome many obstacles including costs from limited abundance of raw materials and safety concerns from highly flammable organic electrolytes⁵⁻¹⁰. In this regard, aqueous electrolytes emerge as a potential game changer in LIB market due to its non-flammability, non-toxicity, and low-cost resources. However, aqueous electrolytes give a narrow electrochemical stability window of ~ 1.23 V away from which gives rise to thermodynamic water decomposition such as hydrogen and oxygen evolution. Inevitably, this acts as a bottleneck for the limited choice of electrode materials that in turn provide a limited energy density for the aqueous system, making it unfit for practical application¹¹⁻¹³. Recently, highly concentrated electrolytes have attracted a tremendous interest for

both aqueous and non-aqueous systems owing to their remarkable characteristics distinct from dilute electrolytes, which include low solvent activity, low flammability, and ability to suppress side reactions¹⁴⁻²⁰. Especially, super-concentrated electrolytes in an aqueous electrolyte system, with “water-in-salt” and “hydrate-melt” prototypes have already outperformed conventional electrolytes by suppressing water activity and thus expanding its stability window of electrochemical operation²¹⁻³³. These newly proposed concentrated electrolytes enable high voltage operation of an aqueous battery with wide-range of electrode choice. However, there exists a significant economic concern especially regarding the use of expensive organic salts like imide organic salts that delays the market use of the aqueous battery. For instance, the price of aqueous electrolyte solution of 21 molal (21 m) lithium bis(trifluoromethanesulfony)imide (LiTFSI), which is the most well-known high-concentration aqueous electrolyte, is about 18 times that of conventional non-aqueous electrolytes (i.e. 1 M LiPF₆)³¹ and about 6 times higher than that of 9.26 m NaCF₃SO₃, which is widely studied for sodium-based high-concentration aqueous electrolyte system (see **Table 2.1** for the price comparison of various saturated aqueous electrolyte systems), bringing up an urgent need for low-cost high voltage aqueous electrolytes.

Historically, lithium- and sodium-based salts consist of sulfate (SO₄), nitrate (NO₃), and perchlorate (ClO₄) have been used as solutes for aqueous electrolytes owing to their anion stability within the operating voltage window and low cost^{11-13, 34-37}. Unfortunately, these inorganic salts have received relatively less attention in highly

concentrated aqueous battery than organic counterparts specially known for their ability to form a protective SEI layer by anion decomposition^{21-24,27-29,32,33,38,39}. Nevertheless, they are still competitive in terms of low price and the ability to change water solvation structure, because the ability to change the water solvation structure and their solvating behaviors in the aqueous systems have been relatively well evaluated and investigated in the previous literatures³⁴⁻³⁷. In addition, the solvation interaction between water molecules and inorganic salt ions dissolved in water has been studied mainly in dilute condition, over many years³⁴⁻³⁷. The summary of their behaviors is well presented in Hofmeister series, which predicts the effects of inorganic salts on solvation structure in dilute aqueous solution by rank-ordering anions according to their strength of water solvation and dividing them into water structure-making and -breaking groups⁴⁰. According to this series, water solvation power in all commonly used anion of inorganic salts can be ordered, $\text{SO}_4^{2-} > \text{NO}_3^- > \text{ClO}_4^-$, implying ClO_4^- salts having tendency to break water structure for high solubility and probability of changing solvation structures with ion aggregations^{36,37,41}. Although the Hofmeister series is basically used for examining the influence of the salts on the solubility of proteins in aqueous solution and has been studied in the dilute conditions, it could be extended to predict the effects of inorganic salts on the solvation structure in the aqueous solution. Moreover, rank-ordering of various anions and dividing them into water-structure-making and -breaking groups from the series might offer the guidelines in the selection of the proper solutes in high-concentration aqueous electrolytes. Anion salts that have a

strong tendency to break the water structure would be correlated with the solubility and the probability of changing solvation structures with ion aggregations^{36,37,41}. Recent molecular dynamics (MD) simulations also support that this would be more pronounced in the case of highly concentrated aqueous solutions⁴²⁻⁴⁷. This theoretical study provides an important evidence that high-concentration water structure-breaking salts tend to exhibit ion aggregated networking with water, enhancing the possibility of expanding the stability voltage window of aqueous electrolytes. Hence, this inspires a great need to revisit and examine all the commonly used inorganic salts in super-concentrated aqueous electrolytes.

Here, we demonstrated all the saturated aqueous solutions dissolved commonly used low-cost inorganic solutes and revisited their chemistry in the high-concentrated aqueous sodium rechargeable batteries. Water-structure-modifying effect of the salts was probed for saturated aqueous solutions in which lithium- or sodium- sulfate (SO_4), nitrate (NO_3), and perchlorate (ClO_4) solutes were dissolved and was compared with those of already reported super-concentrated electrolytes using organic salts such as LiTFSI and NaCF_3SO_3 . We find the saturated NaClO_4 (17 m) solution can be a promising candidate for low-cost high-voltage sodium aqueous electrolyte with electrochemical stability window up to 2.7 V. With this new-class electrolyte, we successfully developed a 2 V Na-ion full-cell with high coulombic efficiency (up to 99 %) and cycle stability up to 200 cycles at 1 C rate. In addition, we also first-time discovered that highly concentrated electrolyte composed of inorganic salts forms a super stable SEI layer without anion decomposition with the

extraordinary OCV stability over 890 hours.

2.2 Experimental method

2.2.1 Preparation of aqueous electrolyte and electrode materials

Aqueous electrolytes including NaClO_4 solution were prepared in various concentrations according to molality (mol of salt in kg of solvent, denoted by m). $\text{Na}_4\text{Fe}_3(\text{PO}_4)_2(\text{P}_2\text{O}_7)$ was synthesized via a conventional solid-state method. A stoichiometric quantity of $\text{Na}_4\text{P}_2\text{O}_7$ (95 %, Aldrich), $\text{FeC}_2\text{O}_4 \cdot 2\text{H}_2\text{O}$ (99 %, Aldrich), and $\text{NH}_4\text{H}_2\text{PO}_4$ (98 %, Aldrich) was mixed using high-energy ball milling (Pulverisette 5, FRITSCH) at 400 rpm for 12 hours. The mixture was calcined at 300 °C for 6 hours under flowing Argon (Ar) before being pelletized manually under 200 kg cm^{-2} pressure using a disk-shaped mold. This sample was then sintered again at 550 °C for 12 hours under flowing Ar. For enhancing the electrical conductivity of an electrode, pyromellitic acid (PA) ($\text{C}_{10}\text{H}_6\text{O}_2$, 96 %, Alfa Aesar) was added during ball-milling (weight ratio of the active material : PA = 95 : 5).

Similarly, $\text{NaTi}_2(\text{PO}_4)_3$ anode was synthesized by mixing stoichiometric amounts of Na_2CO_3 (98 %, Aldrich), TiO_2 (99.7 %, anatase phase, Aldrich), and $(\text{NH}_4)_2\text{HPO}_4$ (98 %, Aldrich) via ball-milling in acetone for 24 hours before evaporating it at 70 °C for 12 hours. A homogeneously mixed powder was sintered at 300 °C for 6 hours under flowing Ar. The calcined powder was pelletized manually under 200 kg cm^{-2} pressure using a disk-shaped mold. This sample was then heated again at

900 °C for 24 hours in air. The carbon-coated $\text{NaTi}_2(\text{PO}_4)_3$ was prepared via high-energy ball milling at 400 rpm for 2 hours with PA (weight ratio of the active materials : PA = 95 : 5). The mixture was annealed at 800 °C for 2 hours under a Ar flow.

2.2.2 Electrochemical measurements

The $\text{Na}_4\text{Fe}_3(\text{PO}_4)_2(\text{P}_2\text{O}_7)$ electrode was fabricated by compressing active materials, super P carbon black, and polytetrafluoroethylene (PTFE) binder with mass ratio of 7:2:1 against a stainless steel grid. Similarly, the $\text{NaTi}_2(\text{PO}_4)_3$ electrode was fabricated with mass ratio of 8:1:1 also on a stainless steel grid. Cyclic voltammetry (CV) was measured using a three-electrode system at a scan rate of 1 mV s^{-1} with a gold electrode (area of 0.126 cm^2) as a working electrode, a standard calomel electrode (SCE) as a reference electrode, and a Pt wire as a counter electrode. For galvanostatic measurements, the half-cell of each electrode was assembled via three electrode configurations with active electrode as a working electrode, activated carbon as a counter electrode, and standard calomel electrode (SCE) as a reference electrode. The full-cell was assembled in a coin-cell (CR2032, Wellcos). Galvanostatic measurements of the half-cell and full-cell were conducted using a multichannel potentio-glavanostat (WBCS-3000, Wonatech, Korea) at 25 °C. All preparation above was performed in a nitrogen-filled glove box.

2.2.2 Materials characterization

The Raman spectroscopy (LabRAM HR Evolution, Horiba) was conducted using capillary tubes (inner diameter of 1.1 – 1.2 mm) with continuous-wave linearly polarized laser wavelengths of 532 nm. The surface analysis of $\text{NaTi}_2(\text{PO}_4)_3$ was performed using a transmission electron microscope (TEM, JEM-2100F, JEOL) equipped with electron energy loss spectroscopy mapping (EELS, Quantum 963, Gatan, Inc, USA). The x-ray photoelectron spectroscopy (XPS) analysis was performed using a monochromatic Al $K\alpha$ X-ray source (1486.6 eV) generated by the acceleration voltage of 15 kV (PHI 5000 VersaProbe, ULVAC-PHI). The XPS spectra of all electrodes were obtained with the raster size of $2 \times 2 \text{ mm}^2$, after etching them by Ar^+ -sputtering of 2 kV acceleration voltage within 5 nm. The overall XPS peaks are arranged based on a reference C-C bond at 248.4 eV.

The soft x-ray absorption spectroscopy (sXAS) measurement, taken at the 10D KIST bending magnet beamline of Pohang Light Source-II (PLS-II), was performed at room temperature under a base pressure of 3×10^{-10} torr. The spectra of C and O K-edges were obtained in surface-sensitive total electron yield (TEY) mode detected at the penetration depth of $< 10 \text{ nm}$ and normalized to the incident photon flux at the energy resolution of 0.1 eV. Before measurement, all electrode samples were washed by dimethoxyethane (DME) for many times and then dried under 70°C vacuum chamber for 12 hours.

2.3 Result and discussion

2.3.1 Selection guideline for the low-cost high-concentration aqueous electrolyte and their chemistry for electrochemical stability in rechargeable aqueous batteries

Based on previous studies, important criteria for super-concentrated aqueous electrolytes are the following: 1) high solubility that enables a cation/water ratio to be over 0.3 to eliminate free water, 2) wide availability with potentially low-cost, and 3) ability to change a cation-anion-water molecule solvation structure at high salt concentration with ion aggregated structure, from which translates into low water activity and stable SEI layer formation^{21,22,24,26,27,38,39}. In search of aqueous electrolytes that satisfy those criteria, we referred to Hofmeister series that consider the thermodynamic properties of inorganic salts commonly used in highly saturated aqueous solution to better comprehend the correlation between their aqueous solubility and influence on water solvation structure. As a result, we came up with a list of commonly used salts including sulfate (SO_4), nitrate (NO_3), and perchlorate (ClO_4)-based sodium salts as tabulated in **Table 2.1**. According to the series, the relative ability to destabilize the bulk water structure for these representative inorganic salt anions is $\text{SO}_4^{2-} < \text{NO}_3^- < \text{ClO}_4^-$, implying that ClO_4^- salts have a strong tendency to break the water structure, indicating the probability of changing solvation structures with ion aggregations^{36,37,40,41,46,47}. Furthermore, the solubility of inorganic salts follows the rank-order of series about water-structure breaking

strength for these salts (i.e., $\text{SO}_4^{2-} < \text{NO}_3^- < \text{ClO}_4^-$ groups), as depicted in **Table 2.1**. Upon reaching solubility limits in water, the water-breaking ions (i.e. ClO_4^-) that constitute the higher end of rank-order, are predicted to be extremely capable of forming complex ion networks with water structure, disrupting their hydrogen bonding networks^{46,47}.

In order to verify this, Raman spectroscopy was employed as a facile tool capable of identifying unique fingerprints from changes in the solvation structure of various electrolyte candidates depending on salt concentration. **Figure 2.1.a, b**, and **2.2** present the Raman spectra of the O-H stretching vibration modes of water molecules in various lithium and sodium aqueous electrolytes at different salt concentrations in the band range of 2,700-4,000 cm^{-1} . In the case of de-ionized water and low concentration electrolytes, both symmetric (near 3,200 cm^{-1}) and asymmetric (near 3,400 cm^{-1}) vibration modes of water molecules exhibit a broad Raman band owing to their diverse hydrogen bonding environments^{21,24,48,49}. The broad band of water clusters maintains its shape at different salt concentrations of conventional aqueous electrolytes, Li_2SO_4 , LiNO_3 , LiClO_4 , Na_2SO_4 , and NaNO_3 , as shown in **Figure 2.2**, indicating the presence of free water. Even at the saturated concentrations of these salts in the electrolyte, the broad nature of the band did not notably change in contrast to the behavior of well-known super-concentrated salts of NaCF_3SO_3 and LiTFSI in **Figure 2.1.a**. On the other hand, it was found that NaClO_4 exhibit hydration characteristics that are distinct from those of other conventional electrolytes and are similar to those of NaCF_3SO_3 and LiTFSI . **Figure 2.1.b** illustrates that, with

increasing salt concentration of NaClO₄, the O–H stretching vibration bands are significantly altered, with gradual disappearance of the broad band followed by the rise of a sharp peak near 3,550 cm⁻¹, which resembles the characteristics of “water-in-salt”^{21,24,50}. Moreover, NaClO₄ showed the most pronounced blue shift of the Raman band, even close to that of LiTFSI, which has been reported as one of the most effective salts in stabilizing the water in the electrochemical system^{24,39}. According to the literatures, this new sharp peak near 3,550 cm⁻¹ was attributed to the signature of crystalline hydrates, where most water molecules participate in ion coordination with cations and anions of the salt with negligible hydrogen bonding among them, giving rise to a unique solvation structure. Hence, this peak can indeed be a clear indicator to determine a new-class electrolyte with a unique solvation structure.

Inspired by this observation, we examined more carefully the aggregation behavior of the NaClO₄ salts in the electrolyte at various concentrations based on the change in the ClO₄⁻ stretching bands in Raman spectra as depicted in **Figure 2.3a**. A blue shift of overall band spectra, with increasing salt concentration from 1 m to 17 m, reveals the drastic change in the cation-anion coordination environment (light blue lines with open circles in **Figure 2.3a**). The band can be deconvoluted into three components: free anion (FA: 932.6 cm⁻¹, red dashed line), solvent-separated ion pairs (SSIP: 934.6 cm⁻¹, blue dashed line), and contact ion pairs (CIP)/aggregated cation-anion pairs (AGG: 941.7 cm⁻¹, green dashed line) (**Figure 2.3a** and **Figure 2.3b**)⁵¹. The FAs fraction, about 77 % at 1 m salt concentration, drastically drops to 20 % at

5 m before it reaches 0 % at 10 m. On the other hand, the SSIPs fraction increases from 22.8 % at 1 m to 79.9 % at 5 m concentration. However, above 10 m concentration, the fraction drops to 42.9 % at 17 m concentration with the majority of ion species (above 57 %) exist as CIP/AGG. Based on both O-H stretching and ClO_4^- stretching band spectra of 17 m NaClO_4 electrolyte, the solvation structure of the high concentrated aqueous NaClO_4 solution transforms to a highly ion aggregated state with the low free water content (**Table 2.1**). Such conclusion is in line with the result from previously reported density functional theory (DFT) calculation, which predicted a significant increase in the number of large sized ion aggregates breaking hydrogen bonding of water by infiltrating into its percolating structure in a form of an intertwined network^{46,47}.

The reduced water activity expected from this unique solvation chemistry can most likely be translated into widening of an electrochemical stability window. Hence, cyclic voltammetry (CV) on gold electrodes at a scan rate of 1 mV s^{-1} was performed as shown in **Figure 2.4**. The overall stability window of 17 m NaClO_4 electrolytes widens to 2.7 V with cathodic and anodic limits at $\sim 1.7 \text{ V}$ and $\sim 4.4 \text{ V}$ vs. Na/Na^+ , respectively. In the enlarged anodic region in **Figure 2.4b**, the oxygen evolution reaction (OER) becomes suppressed with increasing salt concentration from 1 m to 17 m, as the onset potential of OER shifts from 4.0 V to 4.4 V vs. Na/Na^+ . This finding provides the reduced water activity in the high-concentration aqueous electrolyte systems resulting from the changes in the solvation structure^{21-24,26,27}. In addition, the cathodic side also pushes its limit from $\sim 2.2 \text{ V}$ to $\sim 1.7 \text{ V}$ upon a same

concentration change, effectively suppressing hydrogen evolution reaction (HER) as shown in **Figure 2.4a**. Referring the previous literature, this is likely attributed to the formation of a passivation layer from reduction of salt aggregates^{21,22,24,27,28,38,39}. However, considering the difficulty associated with ClO_4^- reduction, this point needs further scrutiny and will be discussed chapter 2.3.4⁵².

Table 2.1. Properties of conventional non-aqueous electrolyte (1 M LiPF₆) vs. aqueous electrolyte salts¹³. The cost from Sigma-Aldrich with an assay above 99% was used. The ionic conductivity was measured at 25 °C.

Salt	Max. Con. (m)	Na ⁺ (Li ⁺)/water molar ratio	Ionic conductivity (mS cm ⁻¹)	Cost (\$ g ⁻¹)	Electrolyte cost (\$ L ⁻¹)
LiPF ₆	-	-		16.06	1 M = 2,439.7
LiTFSI	21	0.38 : 1	~10	7.18	21 m = 43,287.4
Li ₂ SO ₄	3.1	0.06 : 1	69.2	5.5	3.1 m = 119.3
LiNO ₃	7.5	0.14 : 1	80.6	7.64	7.5 m = 400
LiClO ₄	5.6	0.10 : 1	75	5.75	5.6 m = 881.8
Na ₂ SO ₄	1.3	0.02 : 1	118	0.107	1.3 m = 36.4
NaNO ₃	10.7	0.19 : 1	190	0.204	10.7 m = 185.5
NaCF ₃ SO ₃	9.26	0.17 : 1	50	7.68	9.26 m = 12,235.6
NaClO₄	17	0.31 : 1	108	0.49	17m = 1,020.1

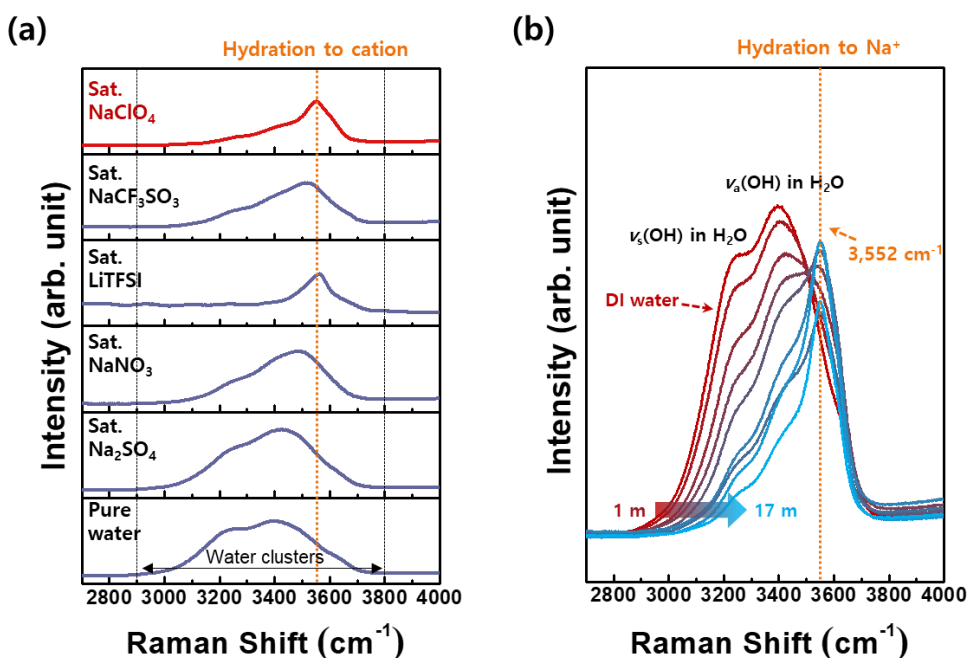


Figure 2.1. (a) Raman spectra of water molecules in various aqueous solutions, namely, saturated 1.3 m Na_2SO_4 , saturated 10.7 m NaNO_3 , saturated 21 m LiTFSI , saturated 9.26 m NaCF_3SO_3 , and saturated 17 m NaClO_4 in water. The broadening of the spectra between the two black dashed lines in the range of $2,900\text{--}3,800 \text{ cm}^{-1}$ is attributed to O–H stretching modes of clustered water molecules with diverse hydrogen bonding. The sharp peak marked by the orange line near $3,550 \text{ cm}^{-1}$ is attributed to cation-solvated water molecules that are free of hydrogen bonding. (b) Raman spectra of NaClO_4 electrolyte at various salt concentrations in the range of $2,700\text{--}4,000 \text{ cm}^{-1}$ showing O–H stretching modes of water molecules.

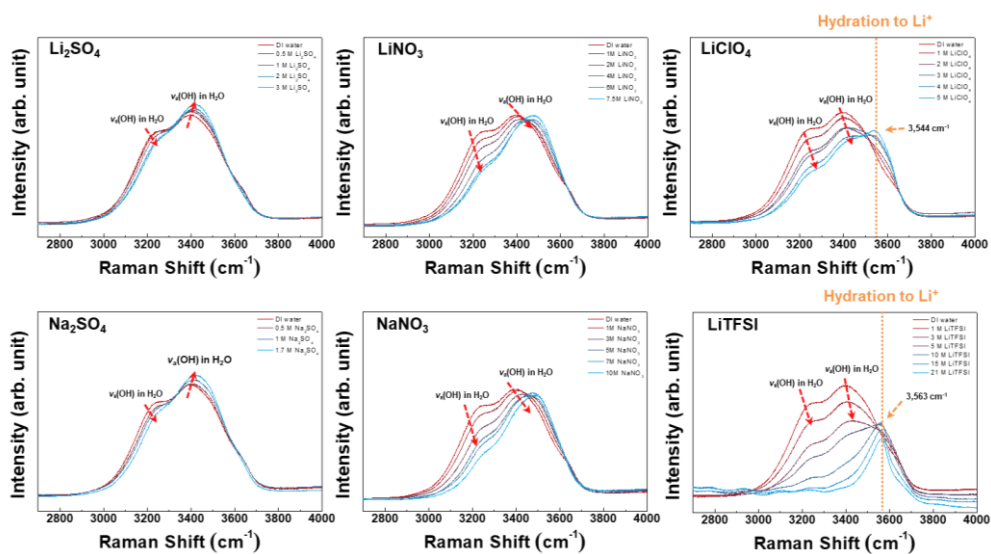


Figure 2.2. Raman spectra of conventional aqueous electrolytes in various salt concentrations.

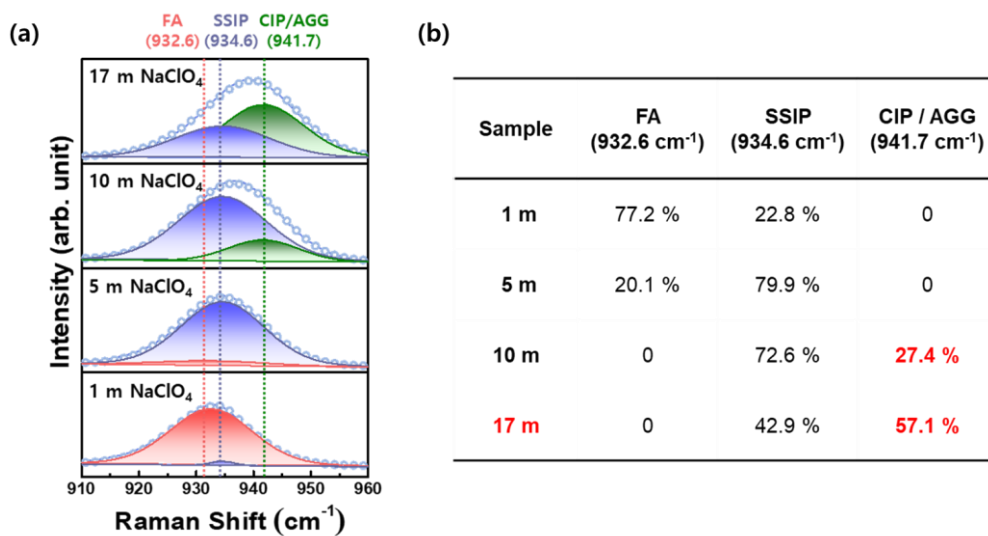


Figure 2.3. (a) ClO₄ stretching modes in Raman spectra for NaClO₄ electrolytes of different salt concentrations (1 m, 5 m, 10 m, and 17 m). **(b)** Deconvolution fitting results of V_s (ClO₄⁻) stretching mode in Raman spectra.

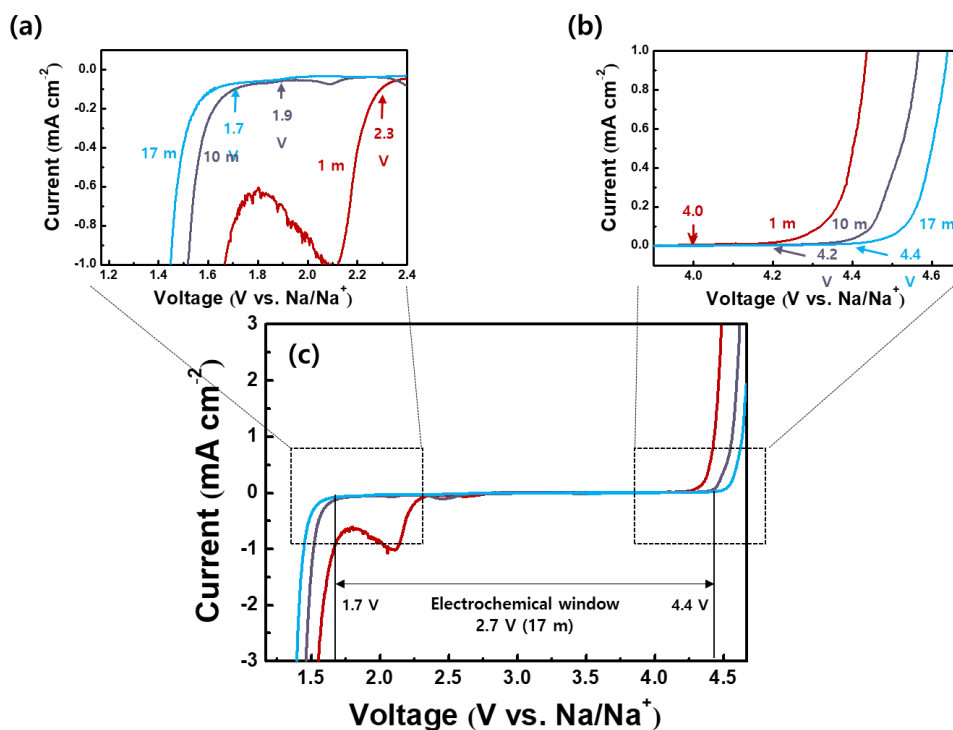


Figure 2.4. (c) Overall electrochemical stability window and (a and b) enlarged regions near the cathodic (HER) and anodic (OER) limits of 17 m NaClO₄ electrolyte determined from CV measurements between -1.55 and 1.65 V vs. SCE at 1 mV s^{-1} on gold working electrodes. The potential was converted to a Na/Na⁺ reference for convenience. The bump near 2.1 V vs. Na/Na⁺ in (a and c) is attributed to bubble formation on a gold electrode.

2.3.2 Electrochemical performance of rechargeable aqueous sodium battery in highly concentrated NaClO₄ aqueous electrolyte system

Based on initial assessment of the electrochemical stability window of NaClO₄ electrolytes using CV, the electrochemical properties of both cathode and anode were further evaluated accordingly. Na₄Fe₃(PO₄)₂(P₂O₇) was chosen as a cathode material due to its promising rate capability and capacity (theoretical capacity of 129 mAh g⁻¹ in organic electrolytes) and its average redox potential of 3.2 V vs. Na/Na⁺ suitable for aqueous system⁵³⁻⁵⁵. At the counter, NaTi₂(PO₄)₃ was chosen as an anode material for its long cyclability, high theoretical capacity (~133 mAh g⁻¹), and average potential of 2.1 V vs. Na/Na⁺ also appropriate for an anodic regime of aqueous system⁵⁶⁻⁵⁹. The structures and morphologies of both pristine Na₄Fe₃(PO₄)₂(P₂O₇) and NaTi₂(PO₄)₃ powders were examined using X-ray diffraction (XRD) and scanning electron microscope (SEM), as shown in **Figure 2.5**. A comparative study of Na₄Fe₃(PO₄)₂(P₂O₇) half-cell and NaTi₂(PO₄)₃ half-cell was conducted in 1 m and 17 m NaClO₄ electrolytes, with the results shown respectively in **Figures 2.6a** and **b**. The first charge/discharge profiles of a Na₄Fe₃(PO₄)₂(P₂O₇) cathode at 1 C under both 1 m and 17 m conditions show discharge capacity of 90–100 mAh g⁻¹ with an average redox voltage of ~ 3.2 V vs. Na/Na⁺, which is similar to that using organic electrolytes (see **Figure 2.6a**). However, charging the cathode to 4.2 V, higher than the theoretical oxygen evolution potential (3.527 V vs. Na/Na⁺ at pH = 7), induces oxygen evolution at ~ 3.9 V vs. Na/Na⁺ in a 1 m condition, while having it suppressed

well in 17 m condition. As expected, the result agrees with CV measurement in **Figure 2.4b**. More dramatic difference could be found in the anodic performance. The voltage profile of the $\text{NaTi}_2(\text{PO}_4)_3$ anode in 1 m NaClO_4 electrolytes indicates the serious HER near 2.0 V *vs.* Na/Na^+ (**Figure 2.6b**). This is attributable to the HER potential (2.297 V *vs.* Na/Na^+ at pH = 7) that is higher than the redox potential of $\text{NaTi}_2(\text{PO}_4)_3$, driving hydrogen evolution to occur in the conventional aqueous electrolyte simultaneously with sodiation of $\text{NaTi}_2(\text{PO}_4)_3$ near 2.1 V *vs.* Na/Na^+ . However, it is remarkable that the highly concentrated NaClO_4 electrolyte could effectively suppress the hydrogen evolution and successfully deliver the discharge capacity of 113 mAh g^{-1} reversibly. Moreover, the capacity could be reversibly retained over 200 cycles in the 17 m NaClO_4 electrolyte as shown in **Figure 2.7**.

To further evaluate the practicality of NaClO_4 electrolytes, $\text{Na}_4\text{Fe}_3(\text{PO}_4)_2(\text{P}_2\text{O}_7)/\text{NaTi}_2(\text{PO}_4)_3$ full-cells were assembled and tested at different electrolyte concentrations. The negative-to-positive electrode mass ratio (NP ratio) was set to $\sim 1.1:1$, considering the specific capacity of $\text{Na}_4\text{Fe}_3(\text{PO}_4)_2(\text{P}_2\text{O}_7)$ and $\text{NaTi}_2(\text{PO}_4)_3$. **Figures 2.8a** and **b** present the galvanostatic charge/discharge profiles of the full-cell at 1C in 1 m and 17 m NaClO_4 electrolytes, respectively, within the voltage range between 0.01 and 2.0 V. In both electrolytes, the full-cell exhibited a discharge capacity of ~ 44 mAh g^{-1} based on the total electrode mass (denoted as mAh $\text{g}^{-1}_{\text{tot}}$) with an average redox voltage of 1.0 V, which is equivalent to an energy density of 36 Wh kg^{-1} . However, similar to the observations in the half-cells, the full-cell using the 1 m electrolyte exhibited irreversible capacity decay upon the first

cycle owing to water decomposition that occurs at approximately 1.8 V (**Figure 2.8a**). The water decomposition is slightly suppressed for the 1 m electrolyte as compared with the half-cells, which is attributed to a relatively fast rate (above 1C), kinetically hindering the decomposition reaction²⁷. On the other hand, significantly less degradation was observed when the 17 m NaClO₄ electrolyte was used as shown in **Figure 2.8b**. In consistent with the half-cell results, no signature of the OER or HER was observed, leading to reversible charge and discharge reaction. CVs of the full-cells that were carried out at a slow scan rate (0.1 mV s⁻¹) further confirm the difference in each electrolyte. The insets of **Figures 2.8a** and **b** illustrate that the irreversible reaction clearly occurred above 1.8 V in the 1 m electrolyte, whereas no detectable signature of the side reaction was observed at a similar voltage level for the 17 m electrolyte.

The long-term cycle stability and coulombic efficiency of the Na₄Fe₃(PO₄)₂(P₂O₇)/NaTi₂(PO₄)₃ full-cell were examined in **Figures 2.9**. **Figure 2.9b** present the galvanostatic charge/discharge profiles of the full-cell at 1C in 9.26 m NaCF₃SO₃ electrolyte, which is previously reported one, within the voltage range between 0.01 and 2.0 V. It was found that the electrochemical performance of the full-cell in both 17 m NaClO₄ and 9.26 m NaCF₃SO₃ electrolyte within initial 3 cycles was comparable. The discharge capacity fading of the cell in 1 m NaClO₄ electrolyte was notably severe over repeated cycles, as the capacity decreases rapidly from 44 to 8 mAh g⁻¹_{tot} (or equivalently from 87 to 17 mAh g⁻¹ based on the cathode mass) within only 50 times of charge and discharge (**Figure 2.9a**). The coulombic

efficiency in 1 m electrolyte was also low (**Figure 2.9c**), starting at 87% for the first cycle before plummeting to 68%. However, notable improvements in both the capacity retention and columbic efficiency of the cell were observed in 17 m electrolyte, with their values eventually reaching 75% and 99% after 200 cycles, respectively. Unexpectedly, this performance is comparable to that of the previously reported “water-in-salt” NaCF_3SO_3 electrolyte (capacity retention and coulombic efficiency of 63% and 99%, respectively) as shown in **Figures 2.9a** and **c**. Additionally, we evaluated the rate capability of the full-cell in 17 m NaClO_4 electrolyte. **Figure 2.9d** presents the discharge profiles of the full-cell at 0.2C, 1C, 5C and 10C after the first charge at 0.2C. The full-cell delivered capacities of 46, 44, 39, and 34 $\text{mAh g}^{-1}_{\text{tot}}$ at 0.2C, 1C, 5C, and 10C, respectively. The acceptable rate capability of the full-cell is attributed to its high ionic conductivity of 108 mS cm^{-1} measured at 25°C . Even at extended high-rate cycle tests, the cell could retain the high capacity and power capability at 5C for more than 500 cycles as illustrated in the inset of **Figure 2.9d**.

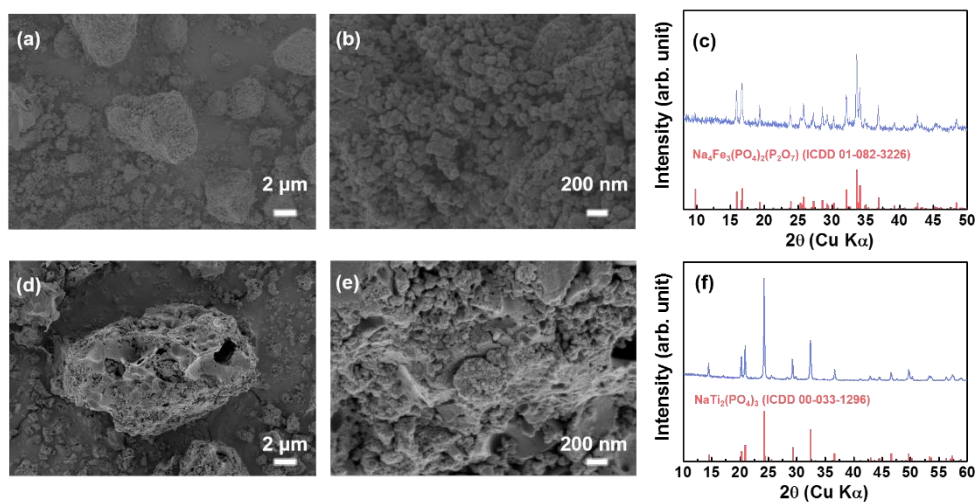


Figure 2.5. (a and b) SEM images and (c) XRD pattern of the pristine $\text{Na}_4\text{Fe}_3(\text{PO}_4)_2(\text{P}_2\text{O}_7)$ powder. (d and e) SEM images and (f) XRD pattern of the pristine $\text{NaTi}_2(\text{PO}_4)_3$ powder.

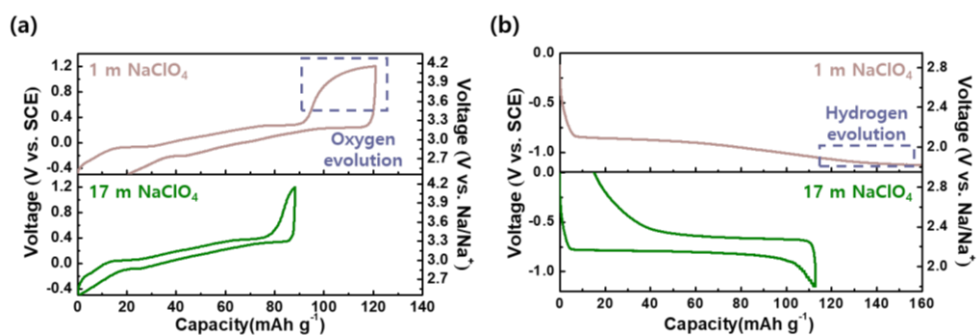


Figure 2.6. Comparison of voltage profiles of **(a)** $\text{Na}_4\text{Fe}_3(\text{PO}_4)_2(\text{P}_2\text{O}_7)$ electrode and **(b)** $\text{NaTi}_2(\text{PO}_4)_3$ electrode in 1 m and 17 m NaClO_4 electrolytes at constant current of 1C. The half-cell data in **(a)** and **(b)** were obtained from a three-electrode system consisting of $\text{Na}_4\text{Fe}_3(\text{PO}_4)_2(\text{P}_2\text{O}_7)$ and $\text{NaTi}_2(\text{PO}_4)_3$ as working electrodes, a SCE as the reference electrode, and activated carbon as the counter electrode.

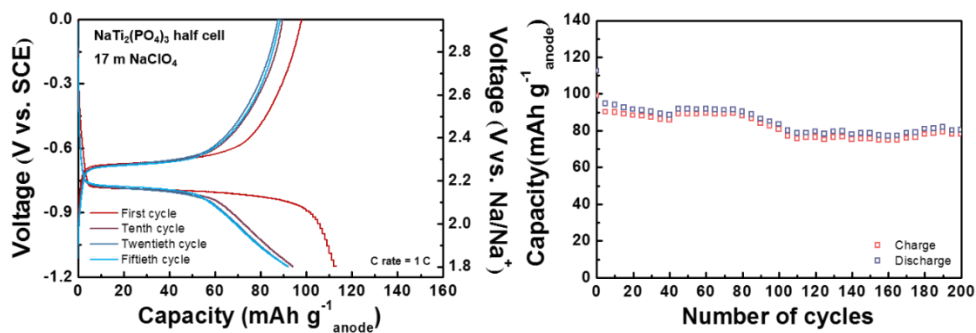


Figure 2.7. Galvanostatic charge/discharge performance and cycle stability of a $\text{NaTi}_2(\text{PO}_4)_3$ half-cell.

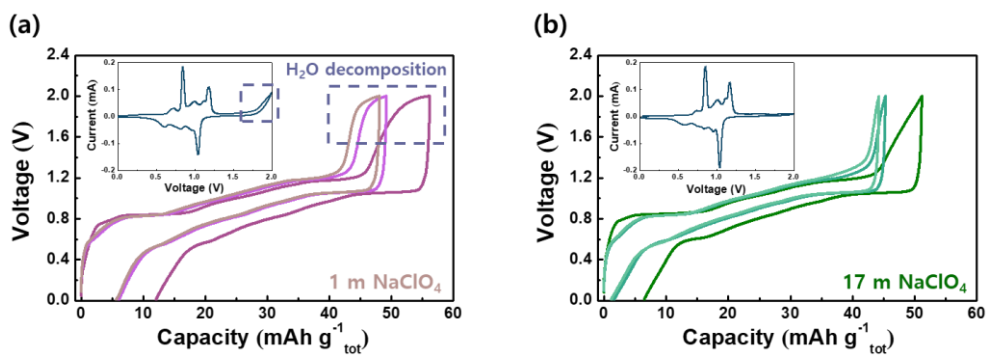


Figure 2.8. Galvanostatic profiles of the $\text{Na}_4\text{Fe}_3(\text{PO}_4)_2(\text{P}_2\text{O}_7)/\text{NaTi}_2(\text{PO}_4)_3$ full-cell in (a) 1 m and (b) 17 m NaClO_4 electrolytes at 1C. The insets of (a) and (b) present CV curves of the $\text{Na}_4\text{Fe}_3(\text{PO}_4)_2(\text{P}_2\text{O}_7)/\text{NaTi}_2(\text{PO}_4)_3$ full-cell at a scan rate of 0.1 mV s^{-1} in (a) 1 m and (b) 17 m NaClO_4 electrolytes.

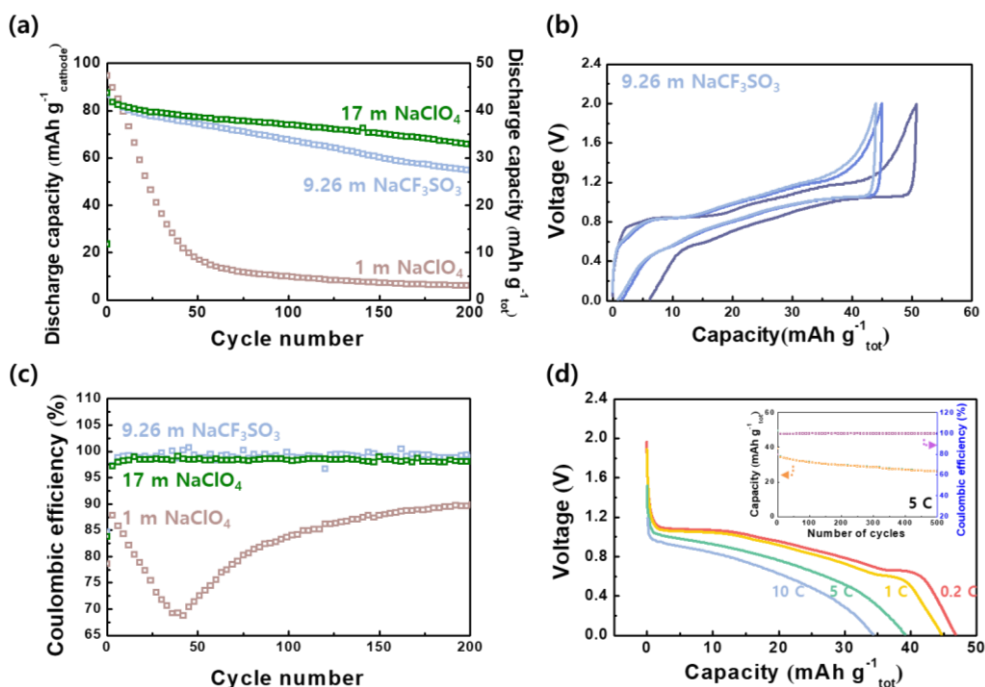


Figure 2.9. (a) Cycle stability of $\text{Na}_4\text{Fe}_3(\text{PO}_4)_2(\text{P}_2\text{O}_7)/\text{NaTi}_2(\text{PO}_4)_3$ full-cell cycled at 1C in different aqueous electrolytes: 1 m NaClO_4 , 9.26 m NaCF_3SO_3 , and 17 m NaClO_4 . (b) Galvanostatic charge/discharge profiles of a $\text{Na}_4\text{Fe}_3(\text{PO}_4)_2(\text{P}_2\text{O}_7)/\text{NaTi}_2(\text{PO}_4)_3$ full-cell in 9.26 m NaCF_3SO_3 electrolyte at 1C. (c) Coulombic efficiency of a $\text{Na}_4\text{Fe}_3(\text{PO}_4)_2(\text{P}_2\text{O}_7)/\text{NaTi}_2(\text{PO}_4)_3$ full-cell cycled at 1C in different aqueous electrolytes: 1 m NaClO_4 , 9.26 m NaCF_3SO_3 , and 17 m NaClO_4 . (d) Rate performance of the $\text{Na}_4\text{Fe}_3(\text{PO}_4)_2(\text{P}_2\text{O}_7)/\text{NaTi}_2(\text{PO}_4)_3$ full-cell in 17 m electrolyte at 0.2C, 1C, 5C, and 10C. The inset of (f) presents the cycle stability and coulombic efficiency of the full-cell in 17 m electrolyte at 5C. The voltage of the full-cell ranges between 0.01 and 2.0 V.

2.3.3 Analysis of the surface protective layer formed in high-concentration aqueous electrolyte

As demonstrated thus far, the highly concentrated NaClO_4 electrolyte suppresses water decomposition and enhances the performance of the aqueous cell, presumably due to the change in the ion solvation structure and reduced water activity. However, it is also worth noting how it influences the stability of the electrode surface, as it has been widely suggested that the formation of a SEI on an active anode occurs via reduction of salts and partially negates the hydrogen evolution^{21,22,24,27,28,38,39}. In addition, the passivation layer acts as a critical component in maintaining the structural stability of a $\text{NaTi}_2(\text{PO}_4)_3$ anode. Nevertheless, to the best of our knowledge, ClO_4^- reduction from the NaClO_4 electrolyte appears highly improbable within the voltage window tested here, as it requires high decomposition energy⁵². Hence, it is necessary to verify how the $\text{NaTi}_2(\text{PO}_4)_3$ anode surface has been protected in our NaClO_4 electrolytes. To examine the surface of the $\text{NaTi}_2(\text{PO}_4)_3$ anode, two samples of $\text{NaTi}_2(\text{PO}_4)_3$ anodes before and after 20 cycles were prepared and probed using transmission electron microscopy (TEM). **Figure 2.10a to f** present representative TEM images of the $\text{NaTi}_2(\text{PO}_4)_3$ electrode particles before and after 20 cycles in 1 m and 17 m NaClO_4 electrolytes. The pristine $\text{NaTi}_2(\text{PO}_4)_3$ particles exhibited clean surfaces with a carbon coating layer thickness of less than 1 nm (**Figure 2.10a and b**). After cycles in 1 m NaClO_4 electrolyte, no significant change or formation of additional protective surface film was observed on the surface of the electrode particles (after 20 cycles at 1C), as shown in **Figures 2.10c and d**. However,

for the sample cycled in 17 m NaClO₄ electrolyte, a 5–10-nm-thick amorphous layer was observed on the NaTi₂(PO₄)₃ surface (**Figure 2.10e and f**), indicating the formation of surface passivation film. The presence of the surface layer after the cycles is similar to what has been previously observed for the NaTi₂(PO₄)₃ anode cycled in highly concentrated NaCF₃SO₃ electrolyte with the SEI layer on the surface (**Figure 2.10g and h**). According to the previous report, it has been suggested that the SEI layer forms due to the reduction of NaCF₃SO₃ salts, yielding to the byproducts such as crystalline NaF nanoparticles, which actively preserve the electrode surface from the HER reaction²⁷. Nevertheless, in our extensive analysis of the surface film, we could not detect any component related with the byproducts from NaClO₄ decomposition within the surface layer of the electrode after cycling in the saturated electrolyte system. Moreover, no sign of elements derived from salt reduction such as Cl could be detected. **Figures 2.11a to f** present the chemical composition analysis of the surface region performed for the NaTi₂(PO₄)₃ anode cycled in 1 m and 17 m NaClO₄ via EELS mapping. While a passivation layer is hardly detectable on the electrode cycled in 1 m NaClO₄ electrolyte in **Figure 2.11a, c, and e**, even for the thick surface film on the electrode cycled in 17 m electrolyte (light yellow dashed region in **Figure 2.11b**), we were only able to detect carbon and oxygen K-edge signals as elements comprising the SEI layer, and other signature of salt reduction such as Cl could not be detected as illustrated in **Figure 2.11e and f**, and **Figure 2.12**.

To support TEM results, XPS analysis was performed on the NaTi₂(PO₄)₃

electrodes cycled in 1 m and 17 m NaClO₄ electrolytes to obtain an in-depth chemical view of the surface layers. O 1s, Na 1s, and Cl 2p spectra of the surfaces of the pristine and cycled electrodes were obtained in **Figures 2.13a-c**. The figures show that O 1s and Na 1s spectra of the electrode cycled in 17 m NaClO₄ electrolytes present generally red shifts compared with those of the pristine electrode and the electrode cycled in 1 m NaClO₄ electrolyte. Peak deconvolution revealed that Na₂CO₃ (the peak at 531.5 eV in O 1s spectra and the peak at 1071.5 eV in Na 1s spectra; purple dashed line) and NaOH (the peak at 532.8 eV in the O 1s spectra, light blue dashed line) were present in the surface layer of the cycled electrode in the saturated NaClO₄ electrolytes (**Figures 2.13a and b**). In addition, the Na Auger peak at 536 eV (green dashed line in **Figure 2.13a**) in the O 1s spectra was also detected for the electrode cycled in 17 m NaClO₄ electrolytes. For possible production of the reduction products from NaClO₄, Cl 2p spectra of the electrodes were examined in **Figure 2.13c**. It is apparent that no salt reduction occurred to generate known compounds such as NaCl from NaClO₄ in consistent with the EELS results in **Figure 2.12**. sXAS analysis was further employed to confirm the XPS results. In **Figures 2.13d and e**, the surface of the NaTi₂(PO₄)₃ electrode at the pristine and charged states after the first and after 5 cycles in 17 m electrolyte was examined for the carbon and oxygen K-edge signals in comparison with a reference Na₂CO₃ spectrum. Both the carbon and oxygen K-edge signals that newly appeared after the first charge agree with the characteristic signals of Na₂CO₃, indicating the formation of Na₂CO₃ in 17 m NaClO₄ system. It is also noted that the peak corresponding to Na₂CO₃

gradually increased until the fifth cycle, implying that the surface layer forms immediately during the first charge process and continues to grow to better protect the surface from the HER. In addition, the newly appeared signal after the fifth cycle in the oxygen K-edge spectrum corresponds to the characteristic signature from NaOH, suggesting its formation on the NTP surface in 17 m NaClO₄ electrolyte.

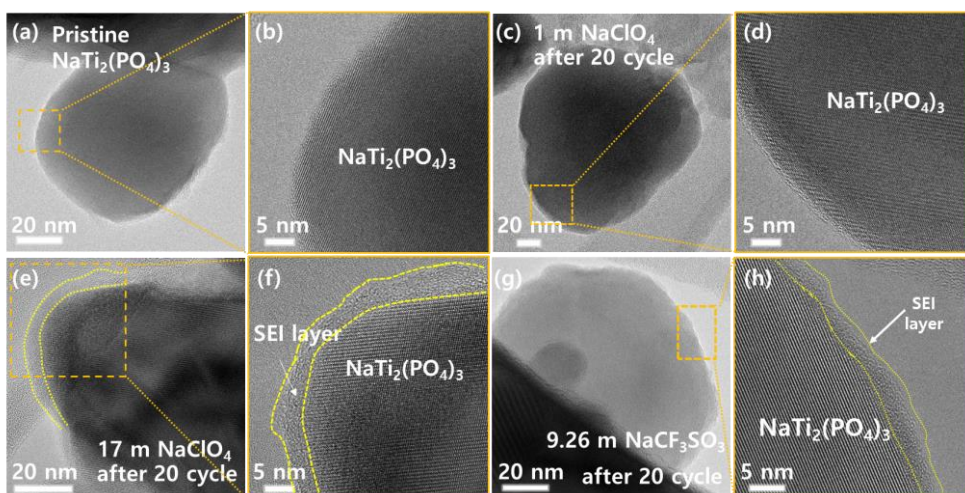


Figure 2.10. TEM analysis of a $\text{NaTi}_2(\text{PO}_4)_3$ anode surface. Low-magnification TEM images of **(a)** pristine $\text{NaTi}_2(\text{PO}_4)_3$ and $\text{NaTi}_2(\text{PO}_4)_3$ after 20 cycles in **(c)** 1 m and **(e)** 17 m NaClO_4 electrolytes at 1C. **(b)**, **(d)**, and **(f)** high-magnification TEM images of **(a)**, **(c)**, and **(e)**, respectively. **(g)** High-resolution TEM images of a $\text{NaTi}_2(\text{PO}_4)_3$ surface after 20 cycles in 9.26 m NaCF_3SO_3 . **(h)** Magnified image (from boxed region in **(a)**) of SEI layer on a $\text{NaTi}_2(\text{PO}_4)_3$ anode surface.

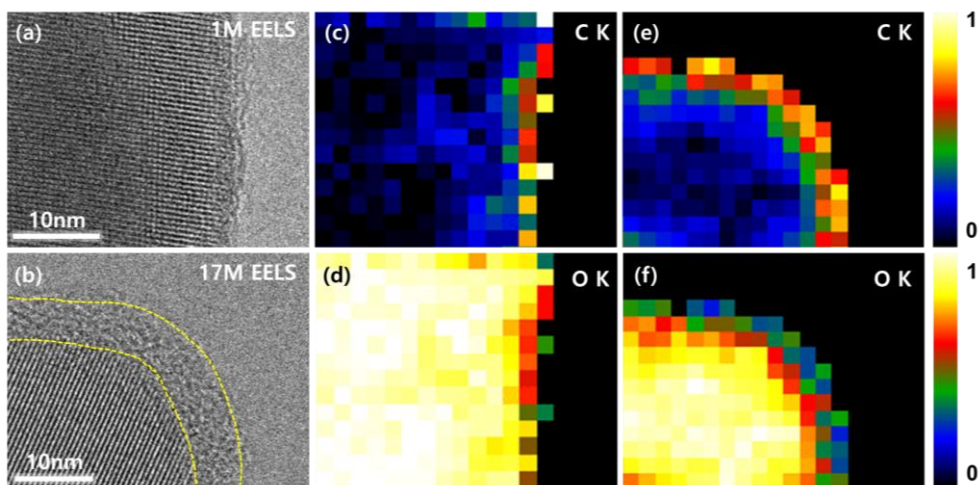


Figure 2.11. (a) High-resolution TEM images and corresponding elemental EELS maps showing (c) carbon K-edge and (d) oxygen K-edge of $\text{NaTi}_2(\text{PO}_4)_3$ surface after 20 cycles in 1 m NaClO_4 electrolyte. (b) High-resolution TEM images and corresponding elemental EELS maps of (e) carbon K-edge and (f) oxygen K-edge of $\text{NaTi}_2(\text{PO}_4)_3$ surface after 20 cycles in 17 m NaClO_4 electrolyte.

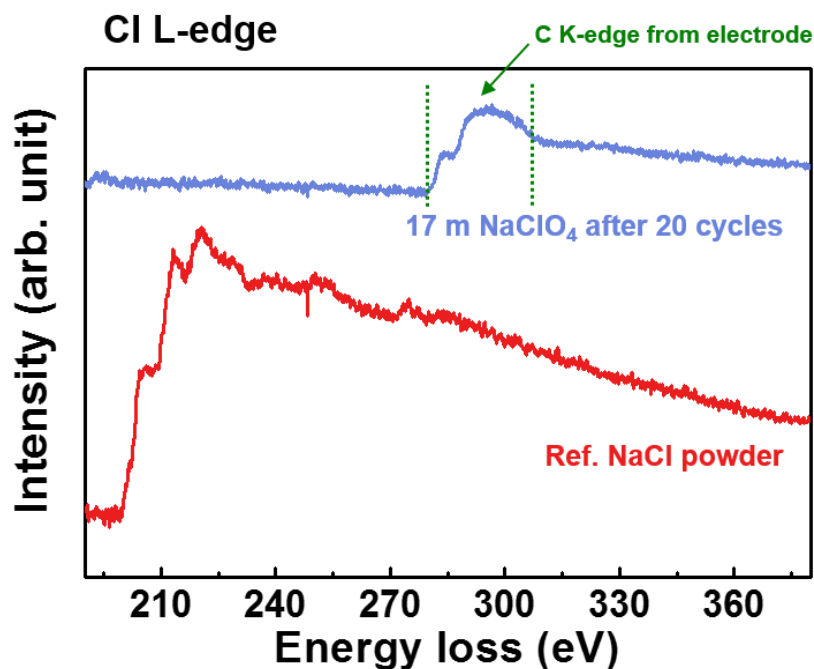


Figure 2.12. EELS spectra of Cl L-edge for surface of the $\text{NaTi}_2(\text{PO}_4)_3$ electrode cycled in 17 m NaClO_4 and for reference NaCl powder. No signals from salt decomposition (i.e., Cl of NaClO_4) were detected on the electrodes cycled in the 17 m NaClO_4 electrolyte. The peak at 284 eV belongs to the carbon K-edge.

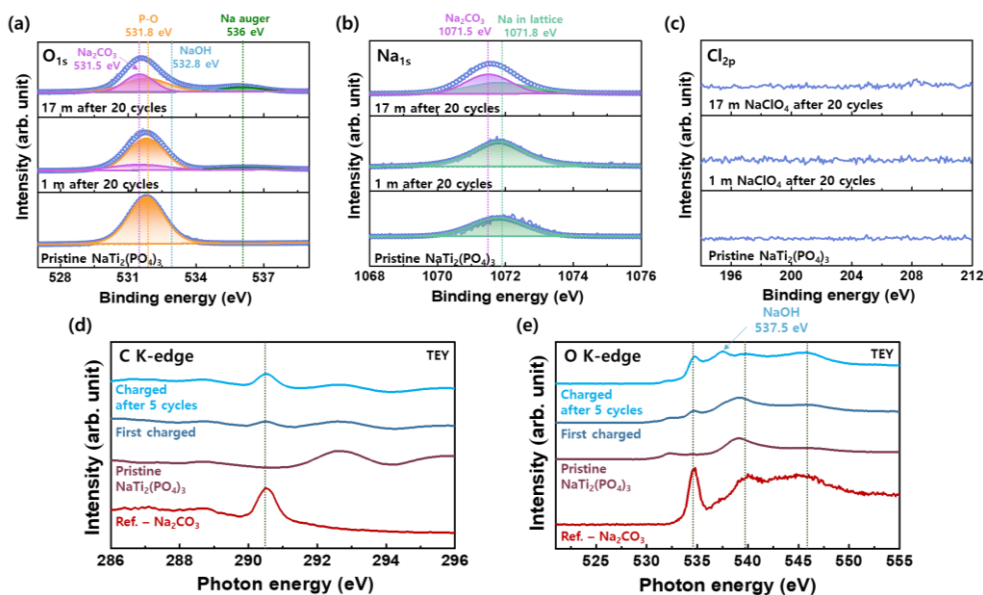
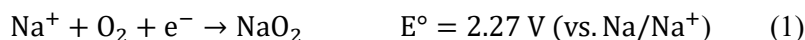


Figure 2.13. XPS profile of (a) O 1s spectra, (b) Na 1s spectra, and (c) Cl 2p spectra of the $\text{NaTi}_2(\text{PO}_4)_3$ electrode before and after 20 cycles in 1 m and 17 m NaClO_4 electrolyte. (d) Carbon K-edge and (e) oxygen K-edge of sXAS spectra of pristine $\text{NaTi}_2(\text{PO}_4)_3$ electrode, first charged electrode, and electrode charged after 5 cycles and reference Na_2CO_3 .

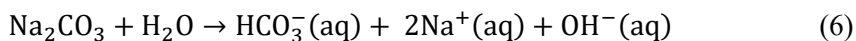
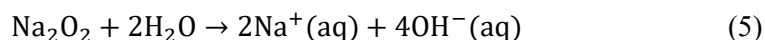
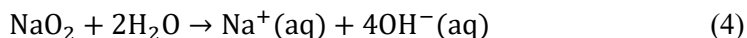
2.3.4 Mechanism of surface layer forming in high-concentration NaClO₄ aqueous electrolytes

Based on the results from the surface analysis of the electrode in highly concentrated electrolytes, we propose that 1) the formation of the surface layer occurs from the first charge process and 2) the layer is composed of carbonates and hydroxides without significant contribution from the salt reduction. Previous reports on a highly concentrated lithium aqueous battery system showed that inorganic compounds such as carbonates and oxides other than those from salt reduction also likely form during electrochemical cycling and they usually originate from the reduction species of O₂ and CO₂ dissolved in the electrolyte³⁹. Similarly, it is supposed that the surface layer formation comprising of Na₂CO₃ in the 17 m NaClO₄ electrolyte was possibly driven by reduction of dissolved gases (O₂ and CO₂). During the first charge process of the full-cell in the highly concentrated NaClO₄ electrolyte, sodium ions may react with dissolved O₂ and CO₂ gases at the potential near the Na intercalation of NaTi₂(PO₄)₃ (~ 2.1 V vs. Na/Na⁺) via the following reaction sequence⁶⁰⁻⁶³:



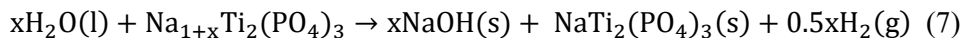
While these reactions are expected to occur for both 1m and 17 m electrolyte

systems thus initially forming a similar surface layer comprising of sodium carbonates and oxides, it is believed that the surface layer cannot be sustained in 1 m NaClO₄ electrolyte due to their general instability in water. It is widely known that they rapidly dissolve and hydrolyze in water via the following reactions^{64,65}:



In fact, Na-O compounds in the surface layer readily hydrolyze and eventually form NaOH via the first two reactions (4) and (5), regardless of salt concentration in aqueous electrolyte, due to their instability in water. Unlike the case of high-concentration electrolytes, where the activity of the free water is significantly diminished, the dissolution reactions of NaOH and Na₂CO₃ are likely to occur rapidly in 1 m NaClO₄ electrolyte due to the substantial presence of free water. As a counter experiment to prove this, we investigated whether the surface layer composed of Na₂CO₃ and NaOH that formed after the cycling in the 17 m NaClO₄ electrolyte would be easily washed out in the fresh deionized (DI) water. In **Figure 2.14a-c**, it is shown that, after DI water washing, the amorphous layer on the surface of the electrode cycled in the electrolytes disappeared, with its thickness rapidly diminishing from ~ 3–4 nm to ~ 1 nm. It clearly supports the idea that the highly concentrated NaClO₄ electrolyte effectively preserves the surface layer composed of carbonates and hydroxides on the anode surface from the dissolution. A consequence

of not having a surface protective layer on a fully sodiated $\text{Na}_{1+x}\text{Ti}_2(\text{PO}_4)_3$ ($x \leq 2$) electrode in dilute electrolyte is the chemical side reaction that results in hydrogen evolution and the loss of sodium such as self-discharge, as in the following reaction²⁷:



To further confirm the stability of the surface layer, we examined the changes in the open-circuit voltages (OCVs) of the charged full-cell after 20 cycles at 1C in 1 m and 17 m NaClO_4 electrolytes, as shown in **Figure 2.14d**. The cell cycled in the 17 m NaClO_4 electrolyte was stable for far longer than the cell cycled in 1 m NaClO_4 electrolyte. The OCV of the cell cycled in 17 m NaClO_4 electrolyte was stably sustained at a constant voltage of 1.08 V for more than 37 days (~ 900 hours). In contrast, the cell cycled in 1 m NaClO_4 electrolyte experienced a drastic voltage drop after only 50 hours, indicating rapid sodium loss from the sodiated anode via self-discharge, leading to hydrogen evolution. This differing stability of the OCVs for the 1 m and 17 m electrolytes can be attributed to the availability of the stable protective layer generated on the anode surface. As a reference, the OCV plot of the cell cycled in 9.26 m NaCF_3SO_3 electrolyte in **Figure 2.14d** also shows the stable constant voltage of 1.08 V for 546 hours, indicating that the enhanced stability of the high-concentration NaClO_4 electrolyte systems is partly due to the stabilized surface of the anode, as was previously demonstrated for the high-concentration NaCF_3SO_3 electrolyte systems²⁷. The overall mechanism about the formation of the surface layer in 1 m and 17 m NaClO_4 aqueous electrolyte is presented in **Figure 2.15**.

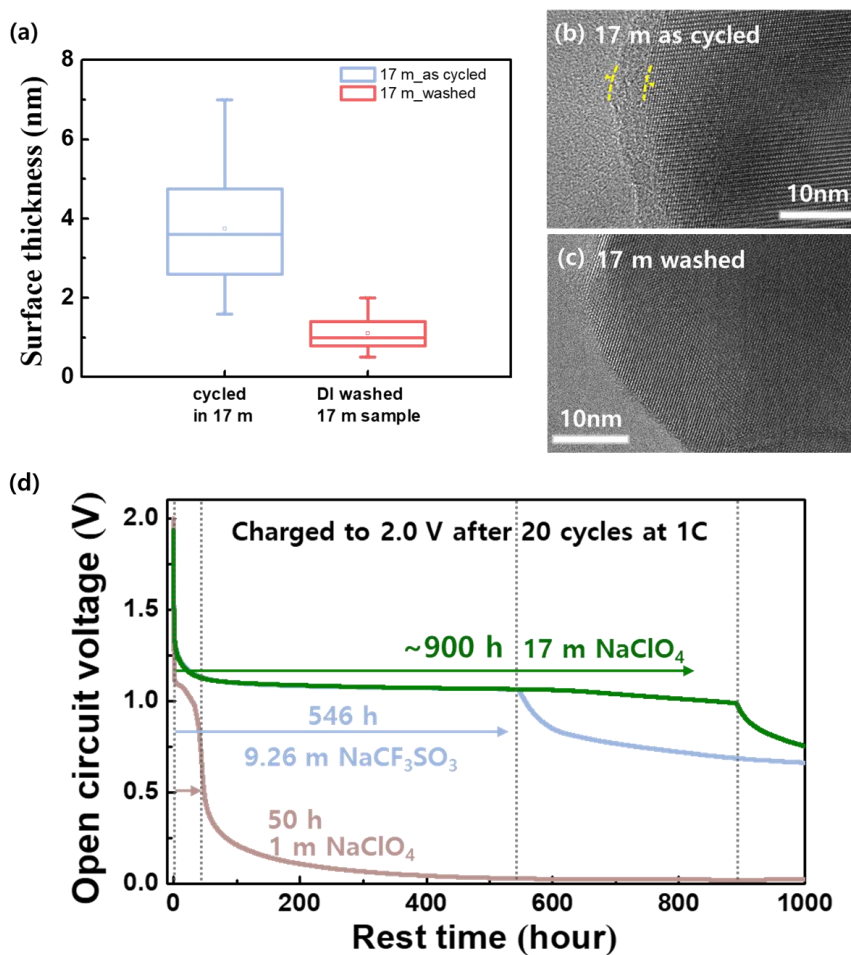


Figure 2.14. (a) Thickness changes of surface layer on NaTi₂(PO₄)₃ electrode cycled in 17 m NaClO₄ electrolyte before and after DI water washing. High-resolution TEM images of the surface of NaTi₂(PO₄)₃ electrode cycled in 17 m NaClO₄ electrolyte, (b) before and (c) after DI water washing. (d) Voltage decay curve of a Na₄Fe₃(PO₄)₂(P₂O₇)/NaTi₂(PO₄)₃ full-cell after full charge (SOC 100) measured at 25 °C. Before obtaining the voltage decay curve, the full-cell was cycled 20 times at 1C in different aqueous electrolytes: 1 m NaClO₄, 9.26 m NaCF₃SO₃, and 17 m NaClO₄, as shown in the graph.

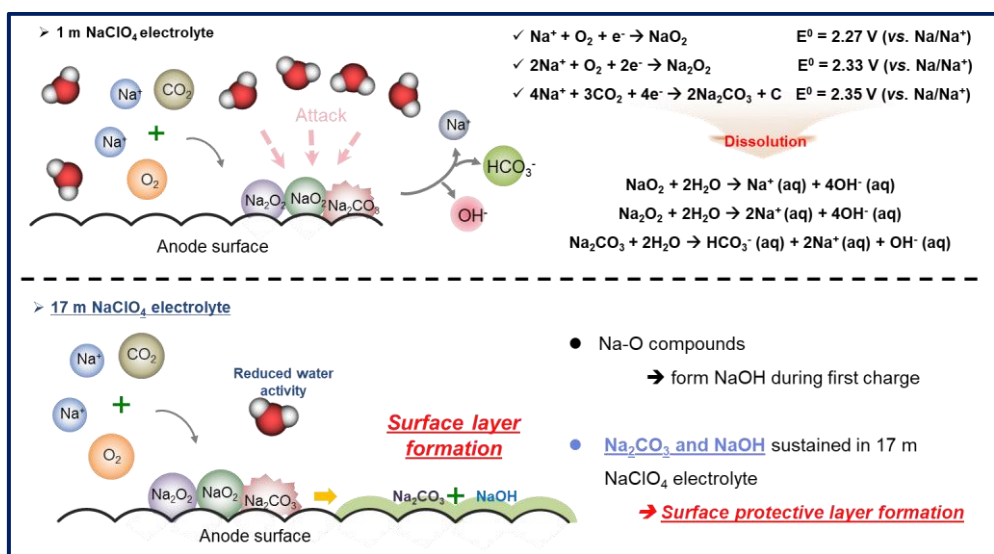


Figure 2.15. Mechanism of the surface layer formation on the NaTi₂(PO₄)₃ anode comparing within 1 m and 17 m NaClO₄ aqueous electrolyte.

2.4 Concluding remarks

We demonstrated for the first time the feasibility of using high-concentration electrolyte based on low-cost inorganic solutes to construct a high-performance aqueous cell. From the rational screening of the potential solutes with respect to the solubility, cost, and solvation strength according to Hofmeister series, 17 m of NaClO_4 was chosen and employed in the sodium aqueous rechargeable batteries. It was successfully demonstrated that a $\text{Na}_4\text{Fe}_3(\text{PO}_4)_2(\text{P}_2\text{O}_7)/\text{NaTi}_2(\text{PO}_4)_3$ full cell could operate with a high energy density of 36 Wh kg^{-1} and coulombic efficiency up to 99% at 1C for over 200 cycles, outperforming the state-of-the-art super-concentrated systems based on NaCF_3SO_3 . This significant outcome is attributed to two key aspects of highly concentrated inorganic electrolytes: 1) expansion of the electrochemical stability window to up to 2.7 V by suppressing water decomposition and 2) robust surface layer formation. In particular, the formation of the surface layer composed of Na_2CO_3 and NaOH led to remarkable stability of the full-cell with extraordinary storage stability for ~ 900 hours. In addition, we proposed a new mechanism of the surface layer formation on the anode involving the oxygen reduction in contrast to the conventional model of the reduction of the salts. It was found that the relative stability of this surface layer in the high-concentration electrolyte aids the stability of the electrode in the cell. Our findings on the new inorganic solutes suitable for the high-concentration aqueous electrolytes broaden our understanding on this new class of electrolyte systems and provide important guidance for the realization of low-cost high-voltage aqueous batteries.

2.5 References

1. Liu, C., Li, F., Ma, L.-P. & Cheng, H.-M. Advanced Materials for Energy Storage. *Adv. Mater.* **22**, E28-E62, doi:doi:10.1002/adma.200903328 (2010).
2. Dunn, B., Kamath, H. & Tarascon, J.-M. Electrical Energy Storage for the Grid: A Battery of Choices. *Science* **334**, 928 (2011).
3. Larcher, D. & Tarascon, J. M. Towards greener and more sustainable batteries for electrical energy storage. *Nat. Chem.* **7**, 19, doi:10.1038/nchem.2085 (2014).
4. Huang, Y. *et al.* Electrode Materials of Sodium-Ion Batteries toward Practical Application. *ACS Energy Lett.* **3**, 1604-1612, doi:10.1021/acsenerylett.8b00609 (2018).
5. Xu, K. Nonaqueous Liquid Electrolytes for Lithium-Based Rechargeable Batteries. *Chem. Rev.* **104**, 4303-4418, doi:10.1021/cr030203g (2004).
6. Choi, N.-S. *et al.* Challenges Facing Lithium Batteries and Electrical Double-Layer Capacitors. *Angew. Chem. Int. Ed.* **51**, 9994-10024, doi:doi:10.1002/anie.201201429 (2012).

7. Roth, E. P. & Orendorff, C. J. How Electrolytes Influence Battery Safety. *Electrochem. Soc. Interface* **21**, 45-49, doi:10.1149/2.F04122if (2012).
8. Vikström, H., Davidsson, S. & Höök, M. Lithium availability and future production outlooks. *Appl. Energy* **110**, 252-266, doi:https://doi.org/10.1016/j.apenergy.2013.04.005 (2013).
9. Kalhoff, J., Eshetu, G. G., Bresser, D. & Passerini, S. Safer Electrolytes for Lithium-Ion Batteries: State of the Art and Perspectives. *ChemSusChem* **8**, 2154-2175, doi:doi:10.1002/cssc.201500284 (2015).
10. Kim, H. *et al.* Recent Progress in Electrode Materials for Sodium-Ion Batteries. *Adv. Energy Mater.* **6**, 1600943, doi:doi:10.1002/aenm.201600943 (2016).
11. Tang, W. *et al.* Aqueous rechargeable lithium batteries as an energy storage system of superfast charging. *Energy Environ. Sci.* **6**, 2093-2104, doi:10.1039/C3EE24249H (2013).
12. Kim, H. *et al.* Aqueous Rechargeable Li and Na Ion Batteries. *Chem. Rev.* **114**, 11788-11827, doi:10.1021/cr500232y (2014).
13. Bin, D. *et al.* Progress in Aqueous Rechargeable Sodium-Ion Batteries. *Adv.*

Energy Mater. **8**, 1703008, doi:doi:10.1002/aenm.201703008 (2018).

14. Yoshida, K. *et al.* Oxidative-Stability Enhancement and Charge Transport Mechanism in Glyme–Lithium Salt Equimolar Complexes. *J. Am. Chem. Soc.* **133**, 13121-13129, doi:10.1021/ja203983r (2011).
15. Suo, L., Hu, Y.-S., Li, H., Armand, M. & Chen, L. A new class of Solvent-in-Salt electrolyte for high-energy rechargeable metallic lithium batteries. *Nat. Commun.* **4**, 1481, doi:10.1038/ncomms2513, <https://www.nature.com/articles/ncomms2513#supplementary-information> (2013).
16. Qian, J. *et al.* High rate and stable cycling of lithium metal anode. *Nat. Commun.* **6**, 6362, doi:10.1038/ncomms7362, <https://www.nature.com/articles/ncomms7362#supplementary-information> (2015).
17. Wang, J. *et al.* Superconcentrated electrolytes for a high-voltage lithium-ion battery. *Nat. Commun.* **7**, 12032, doi:10.1038/ncomms12032, <https://www.nature.com/articles/ncomms12032#supplementary-information> (2016).
18. Chen, S. *et al.* High-Voltage Lithium-Metal Batteries Enabled by Localized High-Concentration Electrolytes. *Adv. Mater.* **30**, 1706102, doi:doi:10.1002/adma.201706102 (2018).

19. Jiao, S. *et al.* Stable cycling of high-voltage lithium metal batteries in ether electrolytes. *Nat. Energy* **3**, 739-746, doi:10.1038/s41560-018-0199-8 (2018).
20. Wang, J. *et al.* Fire-extinguishing organic electrolytes for safe batteries. *Nat. Energy* **3**, 22-29, doi:10.1038/s41560-017-0033-8 (2018).
21. Suo, L. *et al.* “Water-in-salt” electrolyte enables high-voltage aqueous lithium-ion chemistries. *Science* **350**, 938 (2015).
22. Kühnel, R. S. *et al.* “Water-in-salt” electrolytes enable the use of cost-effective aluminum current collectors for aqueous high-voltage batteries. *Chem. Commun.* **52**, 10435-10438, doi:10.1039/C6CC03969C (2016).
23. Suo, L. *et al.* Advanced High-Voltage Aqueous Lithium-Ion Battery Enabled by “Water-in-Bisalt” Electrolyte. *Angew. Chem. Int. Ed.* **55**, 7136-7141, doi:doi:10.1002/anie.201602397 (2016).
24. Yamada, Y. *et al.* Hydrate-melt electrolytes for high-energy-density aqueous batteries. *Nat. Energy* **1**, 16129, doi:10.1038/nenergy.2016.129, <https://www.nature.com/articles/nenergy2016129#supplementary-information> (2016).

25. Kühnel, R.-S., Reber, D. & Battaglia, C. A High-Voltage Aqueous Electrolyte for Sodium-Ion Batteries. *ACS Energy Lett.* **2**, 2005-2006, doi:10.1021/acsenerylett.7b00623 (2017).
26. Reber, D., Kühnel, R.-S. & Battaglia, C. High-voltage aqueous supercapacitors based on NaTFSI. *Sustain. Energy Fuels* **1**, 2155-2161, doi:10.1039/C7SE00423K (2017).
27. Suo, L. *et al.* “Water-in-Salt” Electrolyte Makes Aqueous Sodium-Ion Battery Safe, Green, and Long-Lasting. *Adv. Energy Mater.* **7**, 1701189, doi:doi:10.1002/aenm.201701189 (2017).
28. Yang, C. *et al.* 4.0 V Aqueous Li-Ion Batteries. *Joule* **1**, 122-132, doi:https://doi.org/10.1016/j.joule.2017.08.009 (2017).
29. Yang, C. *et al.* Unique aqueous Li-ion/sulfur chemistry with high energy density and reversibility. *Proc. Natl. Acad. Sci.* **114**, 6197 (2017).
30. Leonard, D. P., Wei, Z., Chen, G., Du, F. & Ji, X. Water-in-Salt Electrolyte for Potassium-Ion Batteries. *ACS Energy Lett.* **3**, 373-374, doi:10.1021/acsenerylett.8b00009 (2018).
31. Lukatskaya, M. R. *et al.* Concentrated mixed cation acetate “water-in-salt”

- solutions as green and low-cost high voltage electrolytes for aqueous batteries. *Energy Environ. Sci.*, doi:10.1039/C8EE00833G (2018).
32. Wang, F. *et al.* Hybrid Aqueous/Non-aqueous Electrolyte for Safe and High-Energy Li-Ion Batteries. *Joule* **2**, 927-937, doi:https://doi.org/10.1016/j.joule.2018.02.011 (2018).
 33. Wang, F. *et al.* Highly reversible zinc metal anode for aqueous batteries. *Nat. Mater.* **17**, 543-549, doi:10.1038/s41563-018-0063-z (2018).
 34. Marcus, Y. Thermodynamics of solvation of ions. Part 5.—Gibbs free energy of hydration at 298.15 K. *J. Chem. Soc. Faraday Trans.* **87**, 2995-2999, doi:10.1039/FT9918702995 (1991).
 35. Hribar, B., Southall, N. T., Vlachy, V. & Dill, K. A. How Ions Affect the Structure of Water. *J. Am. Chem. Soc.* **124**, 12302-12311, doi:10.1021/ja026014h (2002).
 36. Marcus, Y. Effect of Ions on the Structure of Water: Structure Making and Breaking. *Chem. Rev.* **109**, 1346-1370, doi:10.1021/cr8003828 (2009).
 37. Brini, E. *et al.* How Water's Properties Are Encoded in Its Molecular Structure and Energies. *Chem. Rev.* **117**, 12385-12414,

doi:10.1021/acs.chemrev.7b00259 (2017).

38. Borodin, O. *et al.* Liquid Structure with Nano-Heterogeneity Promotes Cationic Transport in Concentrated Electrolytes. *ACS Nano* **11**, 10462-10471, doi:10.1021/acsnano.7b05664 (2017).
39. Suo, L. *et al.* How Solid-Electrolyte Interphase Forms in Aqueous Electrolytes. *J. Am. Chem. Soc.* **139**, 18670-18680, doi:10.1021/jacs.7b10688 (2017).
40. Hofmeister, F. Zur Lehre von der Wirkung der Salze. *Archiv für experimentelle Pathologie und Pharmakologie* **24**, 247-260, doi:10.1007/BF01918191 (1888).
41. Zhang, Y. & Cremer, P. S. Interactions between macromolecules and ions: the Hofmeister series. *Curr. Opin. Chem. Biol.* **10**, 658-663, doi:https://doi.org/10.1016/j.cbpa.2006.09.020 (2006).
42. Choi, J.-H. & Cho, M. Ion aggregation in high salt solutions. II. Spectral graph analysis of water hydrogen-bonding network and ion aggregate structures. *J. Chem. Phys.* **141**, 154502, doi:10.1063/1.4897638 (2014).
43. Kim, S., Kim, H., Choi, J.-H. & Cho, M. Ion aggregation in high salt

- solutions: Ion network versus ion cluster. *J. Chem. Phys.* **141**, 124510, doi:10.1063/1.4896227 (2014).
44. Choi, J.-H. & Cho, M. Ion aggregation in high salt solutions. IV. Graph-theoretical analyses of ion aggregate structure and water hydrogen bonding network. *J. Chem. Phys.* **143**, 104110, doi:10.1063/1.4930608 (2015).
45. Choi, J.-H. *et al.* Ion aggregation in high salt solutions. III. Computational vibrational spectroscopy of HDO in aqueous salt solutions. *J. Chem. Phys.* **142**, 204102, doi:10.1063/1.4920972 (2015).
46. Choi, J.-H. & Cho, M. Ion aggregation in high salt solutions. VI. Spectral graph analysis of chaotropic ion aggregates. *J. Chem. Phys.* **145**, 174501, doi:10.1063/1.4966246 (2016).
47. Choi, J.-H., Choi, H. R., Jeon, J. & Cho, M. Ion aggregation in high salt solutions. VII. The effect of cations on the structures of ion aggregates and water hydrogen-bonding network. *J. Chem. Phys.* **147**, 154107, doi:10.1063/1.4993479 (2017).
48. Auer, B., Kumar, R., Schmidt, J. R. & Skinner, J. L. Hydrogen bonding and Raman, IR, and 2D-IR spectroscopy of dilute HOD in liquid D₂O. *Proc. Natl. Acad. Sci.* **104**, 14215 (2007).

49. Auer, B. M. & Skinner, J. L. IR and Raman spectra of liquid water: Theory and interpretation. *J. Chem. Phys.* **128**, 224511, doi:10.1063/1.2925258 (2008).
50. Chen, Y., Zhang, Y.-H. & Zhao, L.-J. ATR-FTIR spectroscopic studies on aqueous LiClO_4 , NaClO_4 , and $\text{Mg}(\text{ClO}_4)_2$ solutions. *Phys. Chem. Chem. Phys.* **6**, 537-542, doi:10.1039/B311768E (2004).
51. Miller, A. G. & Macklin, J. W. Vibrational spectroscopic studies of sodium perchlorate contact ion pair formation in aqueous solution. *J. Phys. Chem.* **89**, 1193-1201, doi:10.1021/j100253a028 (1985).
52. Coates, J. D. & Achenbach, L. A. in *Perchlorate: Environmental Occurrence, Interactions and Treatment* (eds Baohua Gu & John D. Coates) 279-295 (Springer US, 2006).
53. Kim, H. *et al.* New Iron-Based Mixed-Polyanion Cathodes for Lithium and Sodium Rechargeable Batteries: Combined First Principles Calculations and Experimental Study. *J. Am. Chem. Soc.* **134**, 10369-10372, doi:10.1021/ja3038646 (2012).
54. Kim, H. *et al.* Understanding the Electrochemical Mechanism of the New Iron-Based Mixed-Phosphate $\text{Na}_4\text{Fe}_3(\text{PO}_4)_2(\text{P}_2\text{O}_7)$ in a Na Rechargeable

- Battery. *Chem. Mater.* **25**, 3614-3622, doi:10.1021/cm4013816 (2013).
55. Fernández-Ropero, A. J., Zarrabeitia, M., Reynaud, M., Rojo, T. & Casas-Cabanas, M. Toward Safe and Sustainable Batteries: $\text{Na}_4\text{Fe}_3(\text{PO}_4)_2\text{P}_2\text{O}_7$ as a Low-Cost Cathode for Rechargeable Aqueous Na-Ion Batteries. *J. Phys. Chem. C* **122**, 133-142, doi:10.1021/acs.jpcc.7b09803 (2018).
56. Park, S. I., Gocheva, I., Okada, S. & Yamaki, J.-i. Electrochemical Properties of $\text{NaTi}_2(\text{PO}_4)_3$ Anode for Rechargeable Aqueous Sodium-Ion Batteries. *J. Electrochem. Soc.* **158**, A1067-A1070, doi:10.1149/1.3611434 (2011).
57. Li, Z., Young, D., Xiang, K., Carter, W. C. & Chiang, Y.-M. Towards High Power High Energy Aqueous Sodium-Ion Batteries: The $\text{NaTi}_2(\text{PO}_4)_3/\text{Na}_{0.44}\text{MnO}_2$ System. *Adv. Energy Mater.* **3**, 290-294, doi:10.1002/aenm.201200598 (2012).
58. Wu, X.-y. *et al.* Energetic Aqueous Rechargeable Sodium-Ion Battery Based on $\text{Na}_2\text{CuFe}(\text{CN})_6\text{-NaTi}_2(\text{PO}_4)_3$ Intercalation Chemistry. *ChemSusChem* **7**, 407-411, doi:10.1002/cssc.201301036 (2014).
59. Wang, Y. *et al.* A Novel High Capacity Positive Electrode Material with Tunnel-Type Structure for Aqueous Sodium-Ion Batteries. *Adv. Energy Mater.* **5**, 1501005, doi:10.1002/aenm.201501005 (2015).

60. Adelhelm, P. *et al.* From lithium to sodium: cell chemistry of room temperature sodium–air and sodium–sulfur batteries. *Beilstein J. Nanotechnol.* **6**, 1016-1055, doi:10.3762/bjnano.6.105 (2015).
61. Hu, X. *et al.* Rechargeable Room-Temperature Na–CO₂ Batteries. *Angew. Chem.* **128**, 6592-6596, doi:10.1002/ange.201602504 (2016).
62. Kim, J. *et al.* Dissolution and ionization of sodium superoxide in sodium–oxygen batteries. *Nat. Commun.* **7**, 10670, doi:10.1038/ncomms10670, <https://www.nature.com/articles/ncomms10670#supplementary-information> (2016).
63. Hu, X. *et al.* Quasi–solid state rechargeable Na–CO₂ batteries with reduced graphene oxide Na anodes. *Sci. Adv.* **3** (2017).
64. Yadegari, H. *et al.* On rechargeability and reaction kinetics of sodium–air batteries. *Energy Environ. Sci.* **7**, 3747-3757, doi:10.1039/C4EE01654H (2014).
65. Liu, C. *et al.* On the Stability of NaO₂ in Na–O₂ Batteries. *ACS Appl. Mater. Interfaces.* **10**, 13534-13541, doi:10.1021/acsami.8b01516 (2018).

Chapter 3. Unveiling the superior durability of multi-redox molecules employing high-concentration electrolyte for high-energy and sustainable aqueous battery

3.1 Research background

The surging requirements for the eco-friendly and sustainable energy storage systems have significantly boosted and advanced the mass production of the rechargeable lithium-ion batteries (LIBs) in the current energy market¹⁻³. Although the LIBs lie in the frontline deployment for green energy technologies, it still poses many hurdles to be addressed for large-scale energy storage application such as the high-cost from limited resources and intrinsic safety issues⁴⁻⁷. Especially, the conventional cathodes of LIBs rely on the electrode chemistry based on heavy transition-metals (TM), and it is clear that the limited resources continuously bring about the cost issues⁸⁻¹⁰. Moreover, limited design versatility and reaching theoretical capacity have retarded further advances for greener and sustainable energy storage in grid-scale energy market. Among the next-generation cathode candidates to transcend the drawbacks of the TM based cathode materials, the redox-active organic materials (ROMs) have stood out as promising alternatives due to their low-toxicity, potential cost-efficiency, and sustainability^{8,11-17}. Different from the conventional TM based inorganic materials, the ROMs mainly consist of light and naturally

abundant elements such as carbon, oxygen, hydrogen, nitrogen, and sulfur, which are advantageous to deliver the high specific capacity¹³⁻¹⁵. Furthermore, it is notably attractive that the physicochemical and electrochemical characteristics of the ROMs can be easily and flexibly tuned by tailoring the molecular structure appropriately^{16,17}.

Numerous ROMs including quinone derivatives have been widely reported, in particular, multi-electron-redox phenazine based molecule (i.e. 5,10-dihydro-5,10-dimethyl phenazine, denoted DMPZ) showed exceptional potentials owing to its outstanding electrochemical properties¹⁸⁻²⁴. This material can undergo highly reversible two single-electron redox reactions at the diazabutadiene (N-C=C-N) redox center, which can provide high theoretical capacity of 255 mAh g⁻¹. At the same time, p-type characteristic of DMPZ enables a relatively high average redox potential of 3.4 V vs. Li/Li⁺, considering that redox potentials of most ROMs stay under 3.0 V vs. Li/Li⁺. Therefore, DMPZ can provide superior energy density of 867 Wh kg⁻¹, which is much higher than that of conventional electrodes such as LiCoO₂ and LiNi_{1/3}Co_{1/3}Mn_{1/3}O₂ (550 and 590 Wh Kg⁻¹, respectively)²⁵⁻²⁷. Moreover, the ready-to charge feature of p-type DMPZ enables flexible selection of anode, which can be an attractive point to demonstrate full cell.

Despite the marvelous potential of DMPZ, remaining challenges related to the dissolution of the electrode material and the resulting poor cycle life with undesirable shuttle effects, which are general issues in organic batteries, make it unsuitable for practical implementation²⁸⁻³⁰. Various attempts have been progressed to address these detrimental concerns of the ROMs in organic batteries, such as encapsulation

within the host material, polymerization, and adoption of designed separator^{15,31-37}. The efforts for suppressing the dissolution of DMPZ through the electrode-level tunings such as dimerization were also tried, but the utilization level of DMPZ has not yet been satisfied^{18-24,38}. Therefore, more fundamental approaches are necessary to understand and mitigate the dissolution problems of DMPZ, and rational electrolyte engineering can be a crucial solution for demonstrating high performance organic battery since the dissolution behavior is clearly affected by the interaction between electrolytes and electrode materials.

Herein, we propose the strategy for boosting durability of DMPZ through the rational design of electrolyte which exhibits optimal performance with DMPZ. Carefully predicting and comparing the dissolution tendency of DMPZ for the various solvents through state-of-the-art machine learning technic, we finally adopt the aqueous solution as the most suitable electrolyte to effectively suppress the dissolution. We demonstrate that the DMPZ electrode in 1 m NaClO₄ aqueous electrolyte was retained intrinsically insoluble, thus delivering the enhanced capacity retention of the value reaching 85% over 200 cycles, comparing with the miserable cycling performance in non-aqueous electrolyte. However, the second redox reaction of DMPZ is restricted due to the narrow stability window of the aqueous electrolyte. We further adopt the high-concentration NaClO₄ aqueous electrolyte in our system to fully utilize DMPZ, which is previously reported as the low-cost and high-voltage aqueous electrolyte³⁹⁻⁴¹, and thus the two single-electron redox reactions of DMPZ are successfully provided, corresponding to the discharge capacity of 221 mAh g⁻¹

at 1C rate. The long-term cycle durability of the DMPZ electrode is obtained as the capacity retention of $\sim 87\%$ over 200 cycles at 0.2C rate (over 1,000 hours). Moreover, the outstanding capacity fading rate of $\sim 0.5\%$ per day and capacity retention of $\sim 81\%$ over 1,000 cycles at 1C (over 1,630 hours) are achieved, which is one of the best superior performance in organic aqueous battery systems⁴²⁻⁴⁹.

3.2 Experimental method

3.2.1 Preparation of aqueous electrolyte and electrode

All the chemicals, such as DMPZ (99%, TCI), NaClO_4 (anhydrous 98%, Alfa Aesar), $\text{Zn}(\text{CF}_3\text{SO}_3)_2$ (98%, Sigma-Aldrich, here denoted $\text{Zn}(\text{OTf})_2$), and triglyme (TEGDME, 99%, Sigma-Aldrich), were purchased from commercial suppliers and were used without further purification. The carbon-coated titanium (c-Ti) foil (0.01 mm thickness of carbon-coated on the 0.02 mm thickness of titanium (Ti) with 99.5% of purity, purchased from Wellcos Corporation) was used as a current collector. Non-aqueous electrolyte, especially TEGDME electrolyte, was prepared by 1 molarity (the number of moles of salt (solute, NaClO_4) per total liters of solvent (TEGDME), here denoted by M) of concentration marked in abbreviation (1 M NaClO_4 in TEGDME). In the aqueous battery system, we selected the Zinc (Zn) based aqueous systems with high-concentration electrolyte for perfectly drawing out the performance of DMPZ, because a recently reported electrolyte (17 m NaClO_4 + 0.5 m $\text{Zn}(\text{OTf})_2$) enables the highly reversible and stable dendrite-free Zn plating/stripping, which can be focused on the performance of DMPZ⁵⁰. The aqueous electrolytes (1 m NaClO_4 + 0.5 m $\text{Zn}(\text{OTf})_2$ and 17 m NaClO_4 + 0.5 m $\text{Zn}(\text{OTf})_2$) were prepared by dissolving NaClO_4 and $\text{Zn}(\text{OTf})_2$ in water according to the molality (here denoted by m, 1 mol or 17 mol of NaClO_4 and 0.5 mol of $\text{Zn}(\text{OTf})_2$ in 1 kg of water). To legibly distinguish the electrolytes between non-aqueous and aqueous electrolyte in this manuscript, we only marked using the abbreviation according to

the NaClO₄ concentration (*i.e.* 1 M NaClO₄ in TEGDME, 1 m and 17 m NaClO₄ aqueous electrolyte). Zinc foil (0.25 mm thickness, 99.98% of purity) was purchased from Alfa Aesar. Polytetrafluoroethylene (PTFE) binder was purchased from Wellcos Corporation. The anion-exchange membrane (AMV, 120 μ m thickness, pore size < 10 Å, Selemion, Japan) was used as a separator in the aqueous battery cell. Before use, the AMV separator was immersed in each aqueous solution (1 m and 17 m NaClO₄ aqueous electrolytes) and stored in a glovebox.

3.2.2 Computational details

We used the value of $\log P$ for predicting the soluble property of DMPZ in generic battery electrolyte solutions, in which the term of $\log P$ indicates the logarithmic molar concentration ratio (or logarithmic equilibrium constant) of DMPZ between two different solvents (see **Chapter 3.3.2**). To calculate $\log P$ values (versus water), a deep learning SPR (structure-property relationship) model approach was employed, which can be predicted the solvation free energies of DMPZ in generic battery electrolyte solvents, previously introduced as *Delfos* (deep learning model for solvation free energies in organic solvents) model⁵¹. For the deep learning with the SPR model, our system was trained with 6,618 data points with a database about solvation features of the DMPZ within aqueous and various organic solutions, collected from FreeSolv (aqueous solutions, 642 data points) and Solv@TUM (organic solutions, 5,952 data points) experimental databases, as well as 24 DFT-calculated results for DMPZ with SMD (solvation model based on density) implicit

solvation model at the B3LYP/6-31G(d) level of theory⁵²⁻⁵⁵. We use ORCA 4.2.0 to attend the DFT/SMD calculations⁵⁶. Detailed information regarding a relative solubility prediction of the DMPZ in generic battery electrolyte solutions and its analysis is provided in **Chapter 3.3.2**.

3.2.3 Electrochemistry of DMPZ aqueous battery

The DMPZ electrode was fabricated using the following steps. A slurry, which composed 40 wt% of active materials, 40 wt% of carbon (Super P), and 20 wt% of PTFE dispersed in mixed solutions (water:*N*-methyl-2-pyrrolidone (NMP, 99.5%, Sigma-Aldrich), 9.5:0.5 v/v), was cast onto the c-Ti foil. The resultant mixture was dried in a 30 °C vacuum oven overnight to evaporate the water and NMP solutions and pressed by a roll-presser. The total areal loading of the electrode was ~ 1.0 mg cm⁻². The coin cells (CR2032, Hohsen) with non-aqueous electrolyte (1 M NaClO₄ in TEGDME) were assembled by the DMPZ electrode, a sodium metal as a counter electrode, and a separator (GF/F filter, Whatman) in an Ar-filled glove box. The aqueous DMPZ cells are composed of the active electrode, Zn metal as a counter electrode, and AMV as a separator with each concentration of aqueous solutions (1 m and 17 m NaClO₄ aqueous electrolytes) was assembled in coin cells in an Ar-filled glove box. The galvanostatic charge-discharge process was conducted using a potentio-galvanostat (WBCS-3000, Wonatech, Korea) at room temperature. Before the DMPZ in 17 m NaClO₄ aqueous electrolyte operation was evaluated, all of the

DMPZ cells were performed in several formation cycles (5 to 10 cycles) at 1C rate (1C = 255 mAh g⁻¹). For GITT measurements, the DMPZ cell in 17 m NaClO₄ electrolyte was operated at 1C rate for 2 minutes charge or discharge with 2 hours rest time in galvanostatic mode.

3.2.4 Dissolution behaviors of the DMPZ experiments

The charge-discharge process of the DMPZ in each electrolyte (1 M NaClO₄ in TEGDME, 1 m and 17 m NaClO₄ aqueous electrolytes) were obtained at 1C rate. At the state of charge (SOC) 50 and 100 (see **Figure 3.5**), which indicate the DMPZ⁺ and DMPZ²⁺ respectively, the DMPZ cells were disassembled immediately and the electrode was quickly washed using each solution (water and TEGDME) without salt to eliminate the remained electrolyte. After the washing process, the DMPZ electrodes were immersed in each pristine electrolyte (2 mL) for 12 hours for validating the intrinsic dissolution nature of the DMPZ electrode at different SOC with dissolving and removing the organic intermediates during a sufficient soaking process³⁷. After the soaking process, all solutions were collected and all electrodes were carefully washed again with each blank solution, and then dried in 30 °C vacuum oven overnight for measuring the weight change.

3.2.5 Materials characterization

X-ray photoelectron spectroscopy (XPS) analysis was conducted using a monochromatic Al K α X-ray source (1486.6 eV) generated by an acceleration voltage of 15 kV (PHI 5000 VersaProbe, ULVAC-PHI). All of the XPS spectra about cycled DMPZ electrodes were obtained with a raster size of 2 x 2 mm² after the etching of the electrodes less than 5 nm using Ar ion-sputtering at a 2-kV acceleration voltage. The structural and morphological analysis of the DMPZ electrode was evaluated using X-ray diffraction (XRD, D8 Advance, Bruker) with Cu-K α radiation ($\lambda = 1.54178$ Å) and scanning electron microscope (SEM, SUPRA 55VP, Carl Zeiss). For UV-vis spectroscopy measurement, absorption spectra of the solutions retrieved in dissolution behavior analysis were obtained using a UV-vis spectrometer (Agilent Technologies, Cary 5000) with an optical glass cuvette (Quartz, Hellma).

3.3 Result and discussion

3.3.1 Solubility feature of DMPZ in various electrolyte solutions and electrochemical property of DMPZ in aqueous electrolyte

The rational selection of electrolytes is critically important especially in organic batteries, because the dissolution behavior of organic compounds is determined by the interaction between electrolytes and electrode materials⁵⁷⁻⁶¹. DMPZ, the promising ROM for the organic cathode, also suffers from the dissolution problem and the proper choice of electrolytes is needed. The solubility correlation between organic molecule and solvent is affected by numerous physical properties based on their molecular structures such as dielectric constant, hydrophobic/hydrophilic property, and polarity⁵⁸. For the molecular structure of DMPZ, it has two nitrogen atoms in the pyrazine ring with symmetric benzene rings, which is well-known structure as a methylated phenazine provoking the reversible two-step redox reactions on the diazabutadiene motif as schematically illustrated in **Figure 3.1a**. The symmetric benzene and pyrazine ring structure of DMPZ provides the low polarity and hydrophobicity, leading to the highly soluble feature into the relatively low dipole moment and aprotic non-aqueous solution such as the ether- and linear carbonate-based solvent, which are widely used in battery system^{58,61-63}. It is easily predicted that the DMPZ cathode in the common electrolyte system will show poor cycle stability due to its highly soluble nature in the general non-aqueous media. **Figure 3.1b** presents the charge-discharge profiles of DMPZ cycled in triglyme

(TEGDME) electrolyte within the voltage range of 2.2-4 V vs. Na/Na⁺ at 1C (1C = 255 mA g⁻¹). The specific capacities of 171 and 140 mAh g⁻¹ for the initial charge and discharge, respectively, were delivered with two voltage plateaus indicating the two-electron redox reaction, corresponding to the average voltages of 3 and 3.6 V vs. Na/Na⁺, respectively¹⁸. Different from the initial cycle, the discharge capacity of DMPZ was rapidly decreased from 140 to 77 mAh g⁻¹ within 15 cycles, resulting from the high solubility of DMPZ in TEGDME solution. For the enhancement of cycle stability, it is clear that the suppression of the dissolution of the ROMs can be substantially critical by searching a proper solvent.

Inspired by solubility features and structural peculiarity of the DMPZ molecule, we conducted the state-of-the-art deep learning technique to effectively find the suitable solvent for DMPZ. We note that the deep learning technique has recently been described as a promising prognosticator for anticipating the solvation properties of a given organic compound in various solvents through the calculation of solvation free energies from the empirical properties or structural features of organic materials^{51,52,64-67}. It is well-known that the solvation free energies of the given organic compound enable to provide the relative soluble property with respect to the various kinds of solutions^{51,66}. **Figure 3.2a** indicate the relative solubility of DMPZ (denoted value as log *P* versus water) comparing within generic battery electrolyte solvents (see **Chapter 3.3.2** and **Table 3.1** for calculation details). The log *P* of DMPZ based on solvation free energy for each non-aqueous solvent was comparatively calculated by previously reported *Delfos* model (deep learning model

for solvation free energies in generic organic solvents), while the $\log P$ of water is zero by its definition (see **Chapter 3.3.2**)⁵¹. The solubility of DMPZ in all non-aqueous solvents was much higher than water at least ten times over. Notably, the $\log P$ of DMPZ in aprotic solvents such as linear-carbonate and ether-based solvents, which are conventionally used as the non-aqueous electrolyte, presented higher solubility than water (over $10^{3.5}$ times). To verify the different soluble nature of DMPZ in various solvents, dissolution behavior of DMPZ was compared for DMC, TEGDME, PC, and water. DMPZ easily dissolved in TEGDME and DMC even over the high-concentration of 0.1 M, and 0.02 M of DMPZ also dissolved in PC (see **Figure 3.2c**). In contrast, it was clearly observed that DMPZ was hardly soluble in water, as shown in **Figure 3.2b**, which is coincident with the solubility prediction via deep learning.

To further confirm that the low solubility of DMPZ in water plays an important role in the stable electrochemical performance, we evaluated the cell stability of DMPZ in the aqueous system. **Figure 3.3a** present the galvanostatic charge-discharge curves of DMPZ in 1 m NaClO₄ aqueous electrolyte cycled in the voltage range of 0.1-1.7 V *vs.* Zn/Zn²⁺ (2.03-3.63 V *vs.* Na/Na⁺) at 1C. The upper voltage limit of voltage range (1.7 V *vs.* Zn/Zn²⁺, 3.63 V *vs.* Na/Na⁺) was carefully selected for operating the DMPZ stably with avoiding the oxygen evolution reaction (OER) of water, regarding with the overpotential of OER, which have the theoretical potential of 1.597 V *vs.* Zn/Zn²⁺ at pH = 7. The voltage range of both Na and Zn is presented to compare with the non-aqueous electrolyte system as observed in **Figure 3.1b**.

Unlike the miserable electrochemical stability in TEGDME electrolyte, the DMPZ cathode in 1 m NaClO₄ aqueous electrolyte exhibited highly reversible and stable redox behavior as observed in **Figure 3.3a**. After the capacity of 136 mAh g⁻¹ was delivered in the first discharge process of the DMPZ in aqueous electrolyte, the capacity retention of 85% could be reversibly maintained over 200 cycles as illustrated in the inset of **Figure 3.3a**. As demonstrated thus far, it seems that the reduced solubility of DMPZ in the aqueous electrolyte successfully enhances the cycle stability of the DMPZ cell. However, in the 1 m NaClO₄ aqueous electrolyte, the voltage plateau of DMPZ was solely observed at 1.1 V vs. Zn/Zn²⁺ (3.03 V vs. Na/Na⁺), indicating that the DMPZ just went through the one single-electron reaction, not undergoing the second single-electron redox reaction. It can be attributed to the low charging voltage limit of under 1.7 V vs. Zn/Zn²⁺ (3.63 V vs. Na/Na⁺), where the DMPZ⁺ molecules cannot be fully participated in the second-electron redox reaction near 3.6 V vs. Na/Na⁺ (1.67 V vs. Zn/Zn²⁺) unlike non-aqueous electrolyte (1 M NaClO₄ in TEGDME) case. To fully activate the two single-electron reactions of DMPZ in the 1 m NaClO₄ aqueous electrolyte, the DMPZ cathode was cycled in the voltage rang of 0.1-2.0 V vs. Zn/Zn²⁺, charging higher than the theoretical OER potential (3.527 V vs. Na/Na⁺, 1.597 V vs. Zn/Zn²⁺ at pH = 7) as demonstrated in **Figure 3.3b**. The capacity of 251 mAh g⁻¹ was delivered for the first charge process of the DMPZ, closing to the theoretical capacity of the DMPZ (255 mAh g⁻¹). Moreover, the two-well-defined voltage plateaus at 1.1 V and 1.72 V vs. Zn/Zn²⁺ was observed in the charge process, which is similar to that obtained in the TEGDME

electrolyte (**Figure 3.1b**). However, charging the DMPZ to higher than theoretical OER potential in the 1 m NaClO₄ aqueous electrolyte induces the oxygen evolution at ~1.8 V vs. Zn/Zn²⁺, that results in cycle decay as shown in the inset of **Figure 3.3b**. Hence, it is necessary to further engineer the aqueous electrolyte for suitable application of the DMPZ cathode.

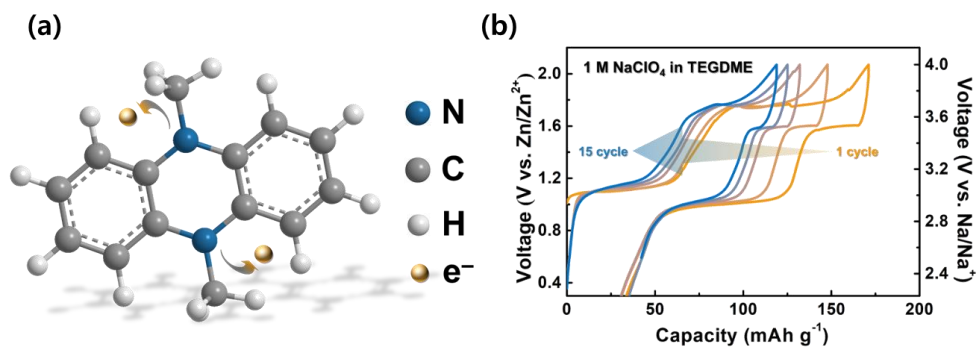


Figure 3.1. (a) Schematic illustrations of molecular structures of DMPZ. (b), Charge-discharge curves of DMPZ for 15 cycles in triglyme (TEGDME) electrolyte cycled in the voltage range of 2.2-4 V vs. Na/Na⁺ at 1C (1C = 255 mA g⁻¹).

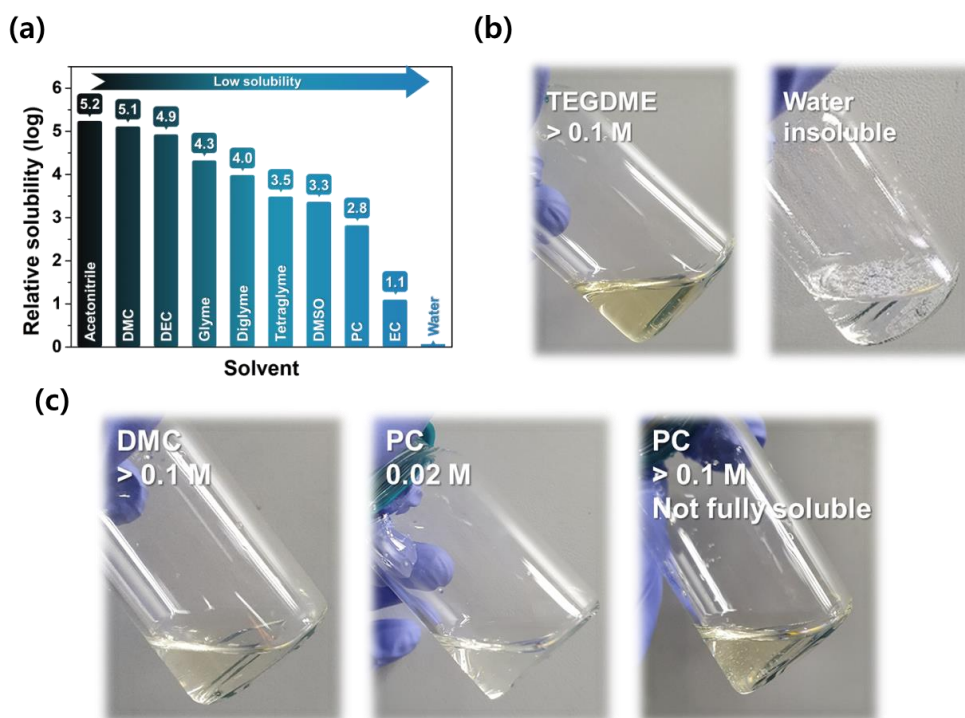


Figure 3.2. (a) Relative solubility of DMPZ calculated by machine learning comparing within generic battery electrolyte solvents. (b) Experimental solubility of DMPZ in TEGDME and aqueous solutions. (c) Dissolution behavior of DMPZ in DMC and PC solutions. DMPZ easily dissolved in DMC solution even over the high-concentration of 0.1 M, which coincident with the solubility prediction in (a). 0.02 M of DMPZ dissolved in PC solution, but ~ 0.1 M of DMPZ was not fully dissolved in PC and DMPZ powder was floating in the solution.

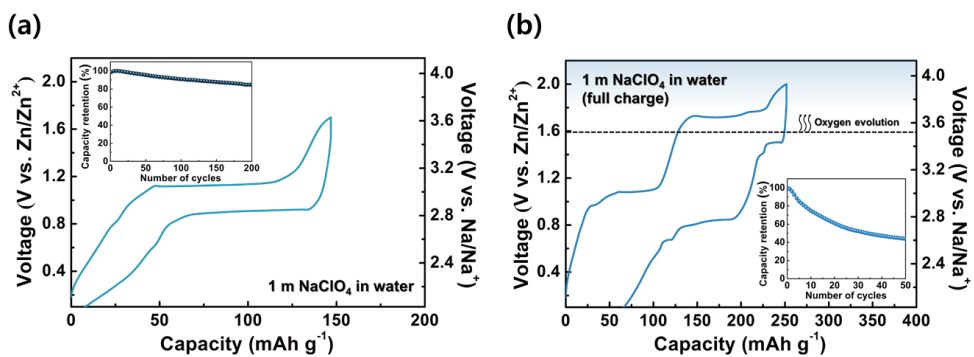


Figure 3.3. Galvanostatic charge-discharge profiles of the DMPZ in 1 m NaClO₄ according to **(a)** half charge and **(b)** full charge. The inset of **(a)** present the cycle stability of DMPZ at 1C. The inset of **(b)** presents the comparison of capacity retention in DMPZ according to half charge and full charge.

3.3.2 Prediction of the solubility of the DMPZ in generic battery electrolyte solutions via deep learning

We consider a solvation process that involves the insertion of a gaseous solute molecule into a bulk solvent. The solvation free energy denotes the accompanying Gibbs free energy change of the given reaction. We can decompose a transfer process between two solvents, $\text{DMPZ}(\text{solv1}) \rightleftharpoons \text{DMPZ}(\text{solv2})$, into two independent solvation processes that share a common solute:



Therefore, we can easily evaluate the Gibbs free energy change of the given transfer reaction:



and the equilibrium constant K also evaluate from its relation between ΔG_{trans} ,

$$\frac{RT}{2.30} \log P(K) = \frac{RT}{2.30} \log \frac{[\text{DMPZ}]_{\text{solv2}}}{[\text{DMPZ}]_{\text{solv1}}} = \Delta G_{\text{solv1}} - \Delta G_{\text{solv2}} \quad (4)$$

The partition coefficient, $\log P$ in equation (4), indicates the logarithmic molar concentration ratio (or logarithmic equilibrium constant) of DMPZ between two different solvents. Although the $\log P$ holds in the infinite dilution limit by definition of the solvation free energy, $\log P$ is still a useful measurement for relative solubility or solvent affinity of a given solute molecule^{65,67}. We calculated $\log P$ (versus water)

values for DMPZ in eight organic solvents as shown in **Table 3.1**, which are commonly used as non-aqueous electrolytes. That is to say, we fix water as *solvent1* in all of the equations and use DMC, DEC, EC, PC, glyme, diglyme, tetraglyme, and DMSO as *solvent2* in all of the equations, respectively. A positive value of $\log P$ denotes that the corresponding solvent readily dissolves DMPZ than water; vice versa for a negative value.

DMPZ has an aprotic nature, and all the non-aqueous solvents do not have any hydrogen bond donors either. Thus, they cannot form any hydrogen bonds at all, making the dispersion and dipole interactions dominant in the intermolecular interactions between DMPZ and the solvents. To assess the DMPZ-solvent interactions, we evaluated dipole moments of the solvent molecules using DFT calculations in the B3LYP/TZVP level of theory^{52,56}. As shown in **Table 3.1**, we found a significant negative correlation between dipole moments and $\log P$ values. In contrast, water molecule tends to make strong hydrogen bonds, as it is generally known. However, nitrogen atoms in DMPZ act as poor hydrogen bond acceptors because they belong to tertiary amine and are strongly conjugated with aromatic rings nearby. Consequently, DMPZ shows an extremely low solubility when compared to the other non-aqueous solvents.

To calculate $\log P$ values, we employed a deep learning SPR (structure-property relationship) model, which are previously introduced as the *Delfos* model, and predicted the solvation free energies of DMPZ in water and eight organic solvents⁵¹. The model predicts the solvation free energy with the following procedure: (i) the

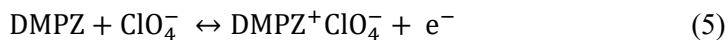
model pretrains $\sim 10^7$ chemical structures to generate atomistic vector representations of the input compounds⁶⁸. (ii) Then, the model performs a deep learning task with experimental and computational data for the target property (i.e. the solvation free energy). (iii) Finally, the model predicts solvation free energies of DMPZ in the given solvents. The SPR model was trained with 6,618 data points, which were collected from FreeSolv (642 data points)⁵³ and Solv@TUM (5,952 data points)^{54,55} experimental databases, as well as 24 DFT-calculated results for DMPZ with SMD (solvation model based on density) implicit solvation model⁵² at the B3LYP/6-31G(d) level of theory. We use ORCA 4.2.0 to attend the DFT/SMD calculations⁵⁶.

Table 3.1. Prediction of the solubility of DMPZ in the generic battery electrolyte solution.

Solvent	Dipole Moment (Debye)	Solvation energy (kJ mol ⁻¹)	Log P
Dimethyl carbonate (DMC)	0.34	-11.5	5.1
Diethyl carbonate (DEC)	0.64	-11.3	4.9
Ethyl carbonate (EC)	5.67	-6.01	1.1
Propylene carbonate (PC)	5.82	-8.33	2.8
Glyme	0.00	-10.4	4.3
Diglyme	1.44	-10.0	4.0
Tetraglyme	1.43	-9.31	3.5
Dimethyl sulfoxide (DMSO)	4.48	-9.00	3.3
Water	1.85	-4.56	0.0

3.3.3 Strategy for perfectly utilizing the performance of DMPZ

To overcome the cycle decay of the DMPZ in 1 m NaClO₄ aqueous electrolyte by OER reaction, we exploited the high-concentration NaClO₄ solution to avoid the OER reaction. The high-concentrated aqueous electrolytes have been adopted for the high-voltage operation of aqueous system by suppressing water activity³⁹⁻⁴¹. In addition, it is well-defined that the dissolution of solute into the high-concentration electrolyte was strongly diminished due to the reduced free-solvent^{32,45,69}. The deterioration process of DMPZ cell in 1 m NaClO₄ aqueous electrolyte by both the OER reaction and the small amount of DMPZ⁺ dissolution possibility is schematically illustrated in the left part of **Figure 3.4a**. As discussed in **Figure 3.3b**, the water molecules in 1 m NaClO₄ aqueous electrolyte go through the oxygen evolution during charging process over theoretical OER potential. Furthermore, even though the DMPZ molecules couldn't dissolve into the water, the DMPZ⁺ or DMPZ²⁺, which are oxidized form of DMPZ in the charging process, are likely to solvate with water due to the substantial existence of free-solvent. These negative facet of the low-concentration NaClO₄ aqueous electrolyte can be addressed by introducing the high-concentration NaClO₄ aqueous solution, which is expected to improve cell performances as follows: (i) widening the electrochemical stable voltage window by suppressing the OER reaction and (ii) reducing the solubility of all charge states of DMPZ as depicted in the right part of **Figure 3.4a**. Additionally, it is also worth noting that the redox potential of DMPZ can be positively shifted by the following Nernst equation described below:



$$E_{\text{DMPZ}^+}^{\text{DMPZ}} = E_0^{\text{DMPZ}^+} + 2.30 \frac{RT}{F} \times \log\left(\frac{1}{a_{\text{ClO}_4^-}}\right) \quad (6)$$

The redox potential of DMPZ in the high-concentration NaClO₄ aqueous electrolyte should shift downward than low-concentration one, as follows equation (6), due to the increased activity of anion (a_{ClO₄⁻}), which is proportional to the mole concentration^{18,70,71}. The downward shift of DMPZ redox potential in high-concentration aqueous electrolyte can also be helpful for the stable cycle performance of DMPZ owing to additionally avoiding the oxygen evolution.

The electrochemical performances of DMPZ was evaluated by employing high-concentration NaClO₄ aqueous electrolyte. **Figure 3.4b** presents the charge-discharge profiles of DMPZ in 17 m NaClO₄ aqueous electrolyte cycled in the voltage range of 0.1-1.7 V vs. Zn/Zn²⁺ (2.03-3.63 V vs. Na/Na⁺) at 1C. The electrochemical performance of DMPZ in 17 m NaClO₄ aqueous electrolyte with two well-defined voltage plateaus around at the average voltage of 0.78 V and 1.45 V vs. Zn/Zn²⁺ was obtained, implying the two single-electron redox reactions of DMPZ was well contributed. Moreover, DMPZ cycled in 17 m NaClO₄ aqueous electrolyte delivered a highly reversible redox behavior without delivering the irreversible capacity for the first charge-discharge process, in comparison with the first irreversible capacity of 31 mAh g⁻¹ for the non-aqueous counterpart case due to dissolution of the DMPZ. It is remarkable that this stable performance of DMPZ in the highly concentrated aqueous electrolyte attributed to suppression of the water

activity via reducing the free water and downshift of the redox potential of DMPZ in the 17 m aqueous electrolyte, as discussed above. The capacity of the first-electron redox reaction in charging process at 0.88 V vs. Zn/Zn²⁺ gradually increased during initial five cycles, which indicates the activation process occurs due to the kinetic hindrance of the reaction in the highly concentrated aqueous electrolyte (see **Chapter 3.3.4** and **Figure 3.7** to **Figure 3.10**).

To confirm the relationship between the high-concentration aqueous electrolyte effect and the stable cycling of DMPZ in this electrolyte, we investigated the voltage change and the solubility of DMPZ during cycling. The downward shift of the DMPZ redox potential in the highly concentrated aqueous electrolyte comparing with low-concentration one was clearly observed in the dQ/dV profiles, as presented in **Figure 3.4c**. It clearly shows that both charge-discharge average potentials of the DMPZ cycled in 17 m aqueous electrolyte downshifted about 0.16 V comparing to the low-concentration one. In addition, the redox potential dependency on the salt concentration was observed as shown in the inset of **Figure 3.4c**. According to the Nernst equation, the redox potential in high-concentration was drastically decreased due to the short-range ion-solvent interactions, resulting in rapid increasing of the activity coefficients of anion ($a_{\text{ClO}_4^-}$) in the equation (6)^{18,70,71}.

To further verify the soluble feature of DMPZ during cycling, we examined the dissolution behaviors of the DMPZ electrode, especially DMPZ⁺ and DMPZ²⁺ state, in comparing between non-aqueous, 1 m NaClO₄ aqueous, and 17 m NaClO₄ aqueous electrolyte. **Figure 3.5a** presents the charge-discharge profiles of the DMPZ

in various electrolytes with the collected solutions (inset picture of **Figure 3.5a**) at state of charge (SOC) 50 and 100 which indicate the DMPZ^+ and DMPZ^{2+} , respectively³⁷. The solutions were obtained by collecting and immersing the DMPZ electrodes at SOC 50 and 100 in the same electrolyte to evaluate the apparently different dissolution behaviors of DMPZ. As discussed above, the charge-discharge property of DMPZ in non-aqueous electrolyte exhibited irreversible behavior and delivered relatively small capacity than the aqueous electrolyte systems. The color of the solution cycled in non-aqueous electrolyte was obviously changed to green at SOC 50 (DMPZ^+) and deep green at SOC 100 (DMPZ^{2+}), indicating serious dissolution of the active materials in charged states. Despite the nearly non-dissolvable DMPZ property in water, the slight dissolution of the DMPZ in charged state (i.e. DMPZ^+ and DMPZ^{2+}) occurred during the charge process. During charge process, the color of the solution cycled in the 1 m NaClO_4 aqueous electrolyte was changed to pale yellow at DMPZ^+ and light green at DMPZ^{2+} . While the color of the all solution cycled in non-aqueous and low-concentration aqueous electrolytes was changed to green series, there is apparently no color changes of the solution cycled in high-concentration NaClO_4 aqueous electrolyte. Note that the color of the solution was remained intact even charged to SOC 100 (DMPZ^{2+}). To additionally confirm the dissolution trend of the DMPZ, we investigated the all solutions via ultraviolet-visible (UV-vis) spectroscopy (see **Figure 3.5b**). From the absorbance spectrum of the solutions cycled in various electrolytes, we measured the relative dissolution quantity of the DMPZ in comparing between non-aqueous electrolyte, 1 m NaClO_4

aqueous, and 17 m NaClO₄ aqueous electrolytes at each charged state of DMPZ (DMPZ⁺ and DMPZ²⁺, respectively) as shown in **Figure 3.6a**. The area of the absorbance spectrum in non-aqueous electrolyte which indicate the dissolution amount of the DMPZ⁺ and DMPZ²⁺ was selected as a reference. When the dissolution quantity of DMPZ in non-aqueous solution (TEGDME electrolyte) was assumed as one (100%), the relative dissolution percent of the DMPZ in 1 m aqueous electrolyte was 0.6 and 0.75 at DMPZ⁺ and DMPZ²⁺, respectively. On the other hand, the amount of the dissolved DMPZ in high-concentration aqueous electrolyte was drastically decreased to below 0.1 (0.08 and 0.03 at DMPZ⁺ and DMPZ²⁺, respectively). It is significant that the high-concentration aqueous electrolyte could exceedingly suppress the dissolution of DMPZ even at SOC 100 (DMPZ²⁺). Moreover, to further evaluate the amount of the dissolved active materials, we measured the weight change of the DMPZ electrode after dissolution, coincided with the results from the UV-vis analysis (see **Figure 3.6b**)³⁷. When the DMPZ electrode oxidized to DMPZ⁺ and DMPZ²⁺ during charge process, at least 40 wt% or more of the active materials was dissolved in the nonaqueous electrolyte and half of DMPZ can be recovered at the end of the discharge (~25 wt% weight loss), which indicating loss of the active materials via dissolution. However, the weigh change of DMPZ cycled in 17 m NaClO₄ aqueous electrolyte exhibited under 8 wt% of weight loss even at DMPZ²⁺ state and almost all of active material was recovered at the end of the discharge process (~1 wt% weight loss), which shows consistency with the results of the UV-vis analysis.

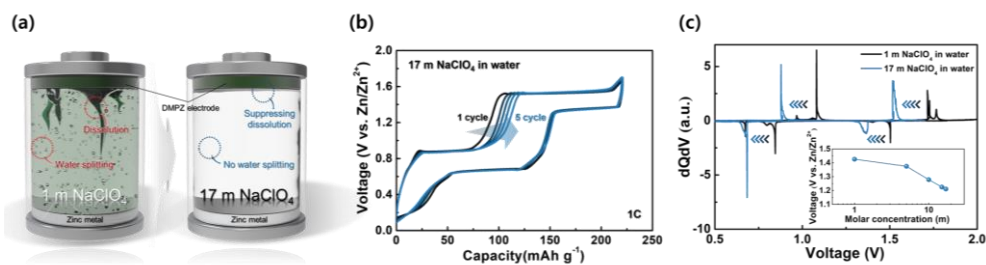


Figure 3.4. (a) Schematic illustrations of the strategy for perfectly drawing out the performance of DMPZ. (b) The charge–discharge profiles of DMPZ for the initial 5 cycles. (c) Comparison of redox potential in dQ/dV curves of DMPZ cycled in 1 and 17 m NaClO₄ aqueous electrolytes. The inset of (c) shows the redox potential dependency on the salt concentration.

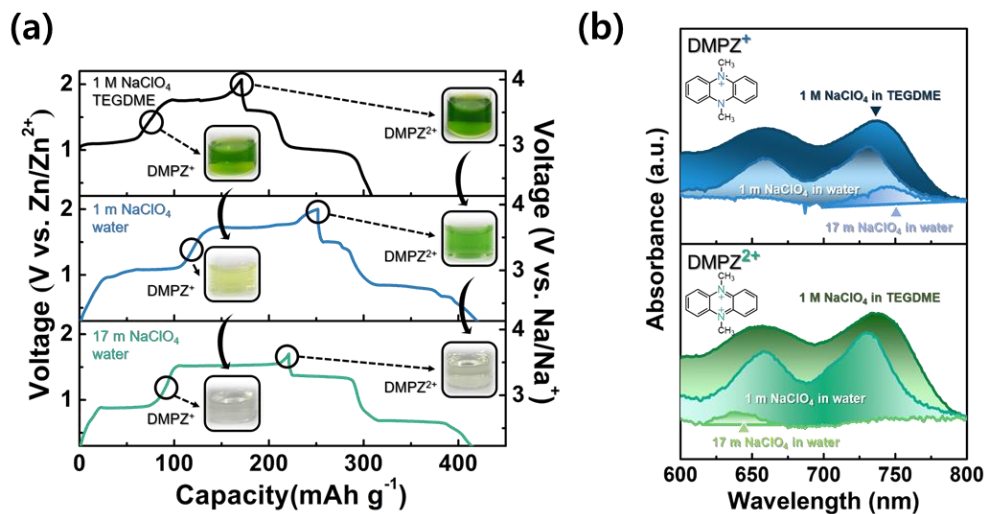


Figure 3.5. (a) Dissolution behaviors of DMPZ electrodes, especially the DMPZ⁺ and DMPZ²⁺ states and comparison of that between in non-aqueous electrolyte, 1 and 17 m NaClO₄ aqueous electrolyte. The inset pictures in (a) show the collected solutions at the DMPZ⁺ and DMPZ²⁺ state in each electrolyte. (b) UV-vis spectroscopy of retrieved solutions after soaking the cycled DMPZ electrode in each electrolyte. The upper part of (b) presents the absorbance spectrum of DMPZ⁺ state solutions and the lower part of (b) presents the UV-vis spectra of DMPZ²⁺ state solutions.

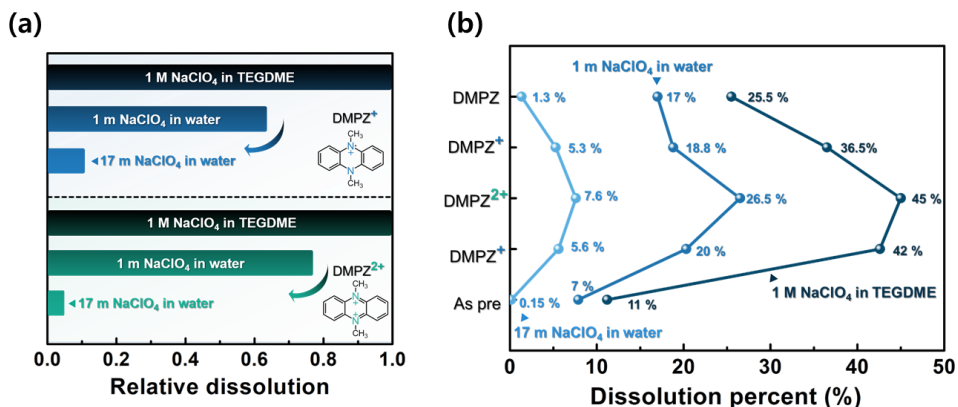


Figure 3.6. (a) Relative dissolution quantity of DMPZ for non-aqueous electrolyte, 1 m NaClO₄ aqueous, and 17 m NaClO₄ aqueous electrolytes at each charged state of DMPZ (DMPZ⁺ and DMPZ²⁺, respectively). The relative dissolution quantity of the DMPZ in comparing each electrolyte was obtained from the area of the absorbance spectrum which indicates the dissolution amount of the DMPZ⁺ and DMPZ²⁺ in **Figure 3.5b. (b)** The corresponding weight changes of the DMPZ electrode at different SOC after the dissolution in each electrolyte.

3.3.4 Kinetic hindrance of the DMPZ initial charge process in 17 m NaClO₄ aqueous electrolyte

When the DMPZ in 17 m aqueous electrolyte initially charged, a low capacity of $\sim 30 \text{ mAh g}^{-1}$ was delivered than the theoretical capacity of 127.5 mAh g^{-1} in the first-electron oxidation reaction at $\sim 0.9 \text{ V vs. Zn/Zn}^{2+}$ of voltage plateau, as observed in **Figure 3.7**. While the first-electron redox reaction shows a small capacity, the second-electron redox reaction delivered the capacity of 187 mAh g^{-1} , which is the 87 % capacity of first charge capacity ($\sim 217 \text{ mAh g}^{-1}$). We suspect that the small capacity of the first-electron redox reaction in the initial charge process of DMPZ can be attributed to the sluggish electrode reaction in 17 m aqueous electrolyte due to its viscous and unfamiliar property with the DMPZ electrode. To verify the sluggish reaction and polarization of DMPZ in 17 m aqueous electrolyte at the initial charge process, we measured the galvanostatic intermittent titration technique (GITT), as depicted in **Figure 3.7**. The dotted dark blue line indicates the theoretical redox potential of DMPZ at the initial charge process. In the initial charge process, the first-electron redox reaction exhibited $\sim 0.6 \text{ V}$ of large polarization, implying a kinetically sluggish reaction of DMPZ in high-concentration aqueous electrolyte. After finishing the first charge process, the polarization of DMPZ in the discharge process was dramatically decreased and does not exhibit in the second cycle. To understand this sluggish oxidation reaction of DMPZ in the initial charge process, the nature of the surface on the DMPZ electrode was investigated using SEM analysis. **Figure 3.8** presents the SEM images of DMPZ powder and before/after

pressed DMPZ electrode. While the DMPZ powder and electrode, which composed of only DMPZ particle and binder, consisted of ~ 10 micrometers of huge secondary particles before the roll-press process as shown in **Figure 3.8a** and **b**, the morphology of the DMPZ electrode after the roll-press process was changed to the flat and condensed surface due to soft and easily moldable property of organic molecules, which consist of primary particles of several hundred nanometers in size (**Figure 3.8c** and **d**). When the high-concentration aqueous electrolyte contacts the DMPZ electrode surface during the initial charge process, this flat and condensed surface morphology of the electrode will be hindered the penetration of electrolyte into the electrode inside for initiating the activation and redox reaction of DMPZ. This hindrance will make it difficult to activate the DMPZ in the initial first-electron reaction, leading to a small capacity due to kinetical polarization as shown in **Figure 3.7**. However, this kinetic hindrance was disappeared after the first charge process, implying the electrolyte and electron activation will be formed in the initial charge process. Therefore, to eliminate the kinetic hindrance of DMPZ cycled in high-concentration aqueous electrolyte, all of the DMPZ cells were performed in several formation cycles (5 to 10 cycles).

Additionally, to compare the surface morphology changes of DMPZ electrode cycled in the non-aqueous electrolyte (1 M NaClO₄ in TEGDME) and high-concentration aqueous electrolyte (17 m NaClO₄ in water) in initial charge-discharge process, SEM analysis of DMPZ electrode cycled in the non-aqueous and high-concentration aqueous electrolyte at initial cycle was evaluated, as observed in **Figure 3.9** and

Figure 3.10. **Figure 3.9a** and **b** present the flat and condensed surface of pristine DMPZ electrode, which consisted of several hundred nanometers sized primary DMPZ particles, as similar within **Figure 3.8c** and **d**. When the DMPZ is charged in a non-aqueous electrolyte, the DMPZ will be dissolved into the electrolyte, resulting in the loss of active materials. Thus, the loss of DMPZ from flat electrode make bumpy morphology, remaining conducting agent (see **Figure 3.9c** and **d**). However, when switching back to the full-discharge state, the dissolved DMPZ could be recovered onto the electrode and make a flat surface again, coinciding with the results of weight change and previously reported works (see **Figure 3.9e-f**, and **Figure 3.6b**)³⁷. On the other hand, the surface of DMPZ cycled in high-concentration aqueous electrolyte appears to change a little bit porous morphology but surely does not changed noticeably at both charged and discharged state in initial cycles, implying the suppression of DMPZ dissolution in high-concentration aqueous electrolyte (**Figure 3.10**). These results exhibit the consistency with the UV-vis analysis and the weight change of **Figure 3.6**.

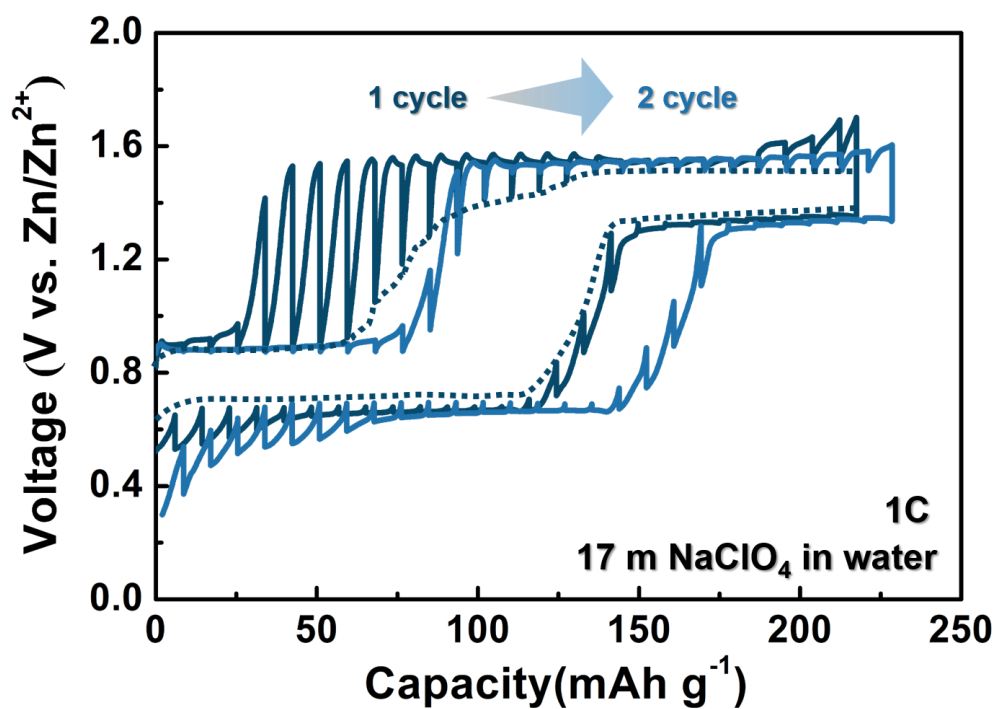


Figure 3.7. GITT profiles of the DMPZ in 17 m NaClO₄ aqueous electrolyte at 1C rate with 2 hours of rest time during initial and second charge-discharge process.

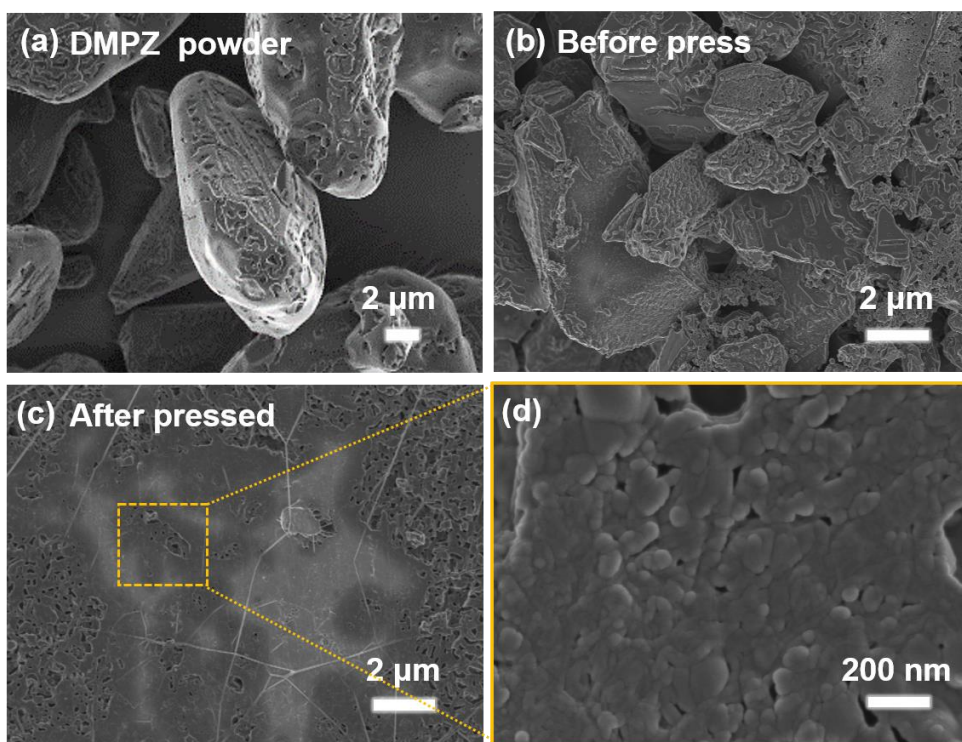


Figure 3.8. Morphology of DMPZ powder and electrode. SEM images of **(a)** pristine DMPZ powder and **(b)** Before roll-press the DMPZ electrode. This electrode was mixed only with DMPZ powder and binder (PTFE), then cast on the c-Ti foil. **(c)** and **(d)** Surface morphology of the electrode after the roll-press process. **(c)** low- and **(d)** high-magnification of the roll-pressed DMPZ electrode.

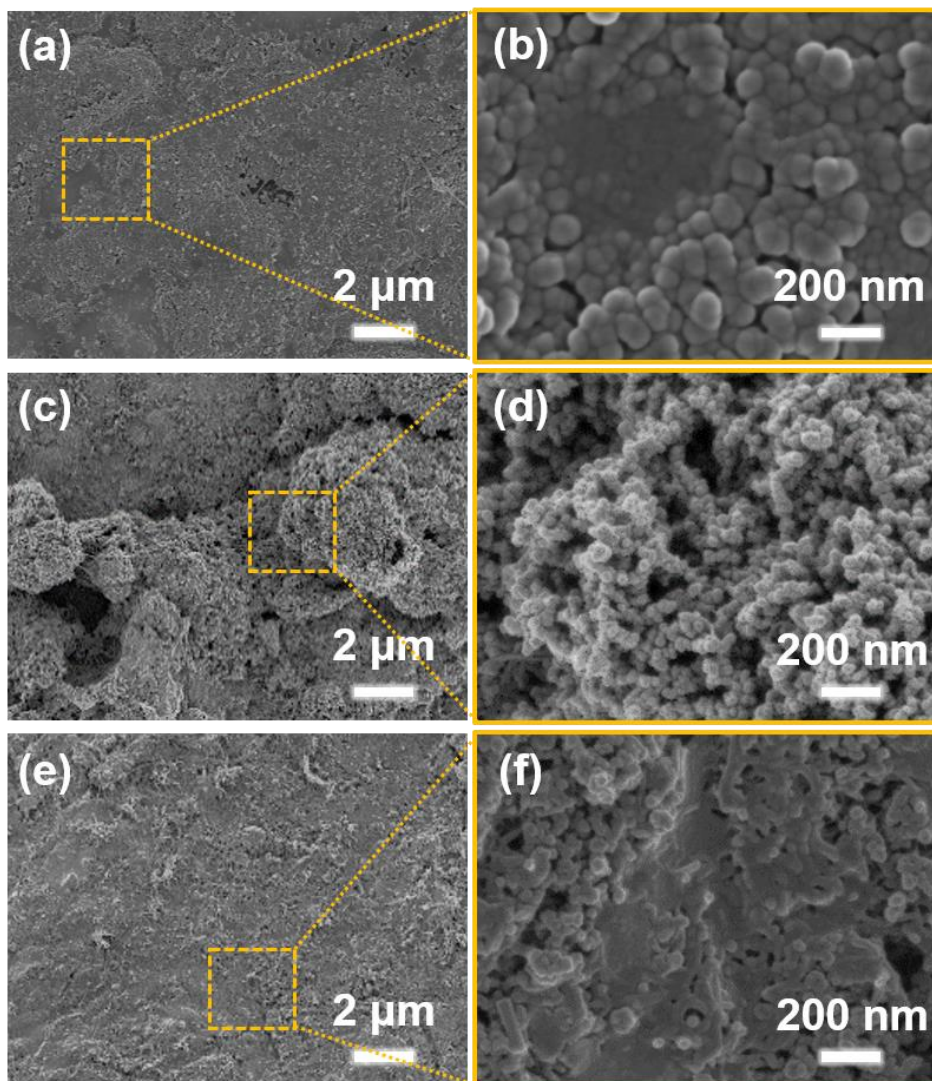


Figure 3.9. Surface morphology of the DMPZ pristine electrode and ex-situ electrode after the first cycle in 1 M NaClO₄ TEGDME electrolyte. **(a, c, and e)** SEM images of **(a)** pristine DMPZ electrode, and **(c)** first charged, **(e)** discharged DMPZ in 1 M NaClO₄ TEGDME electrolyte. **(b), (d), and (f)** presents the magnified SEM images of **(a), (c), and (e)**, respectively.

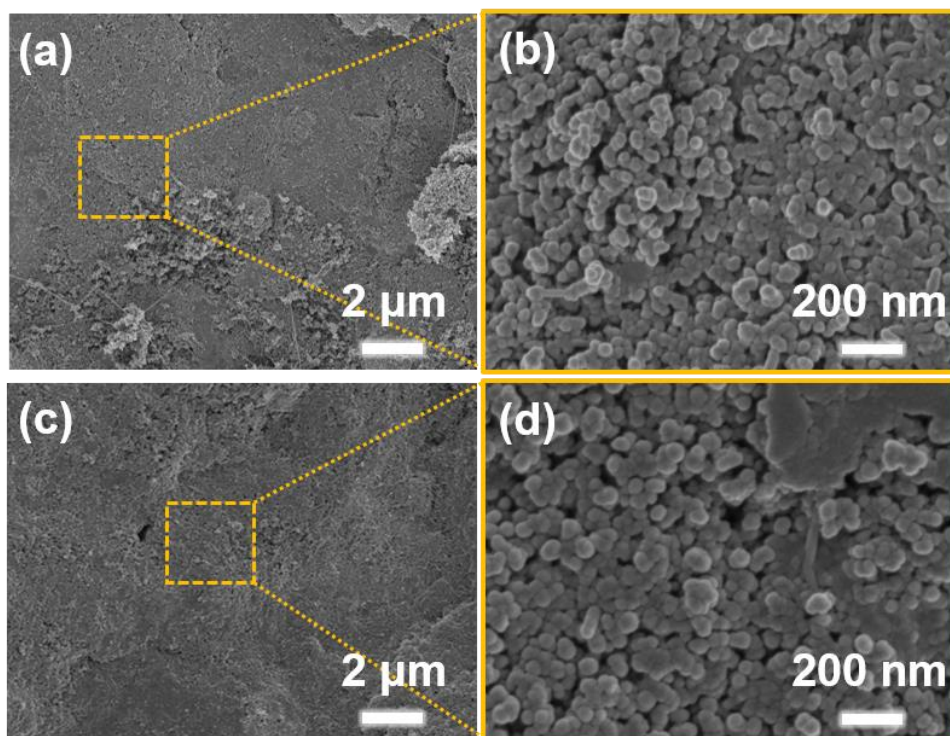


Figure 3.10. Surface morphology of the DMPZ electrode during the first cycle in 17 m NaClO₄ aqueous electrolyte **(a and c)** SEM images of DMPZ electrode after **(a)** first charged and **(c)** first discharged. **(b)** and **(d)** presents the magnified SEM images of **(a)** and **(c)**, respectively.

3.3.5 Durable electrochemical performance of the DMPZ cell employing the high-concentration aqueous electrolyte

To validate the enhanced electrochemical stability of the DMPZ in high-concentration aqueous electrolyte, we conducted the rate capability and long-term cycle stability test of DMPZ in 17 m NaClO₄ aqueous electrolyte in **Figure 3.11**, **Figure 3.13**, and **Figure 3.14**. **Figure 3.11** presents the rate capability of DMPZ cycled in high-concentration aqueous electrolyte at different current rates. DMPZ delivered the discharge capacity of 231, 227, 221, 187, 138, and 107 mAh g⁻¹ at 0.2C, 0.5C, 1C, 2C, 4C, and 5C, respectively. Upon increasing current rate, the characteristic discharge profiles were slightly changed (**Figure 3.12a**). This decent rate performance of DMPZ in high-concentrate aqueous electrolyte is induced to the high ionic conductivity of the 17 m NaClO₄ aqueous electrolyte, which was reported conductivity of above 100 mS cm⁻¹. Additionally, to further reveal the durability of DMPZ in high-concentration aqueous electrolyte, we measured long-term cycle stability of DMPZ in 17 m NaClO₄ aqueous electrolyte as presented in **Figure 3.13** and **Figure 3.14**. It is worth noted that the rigid validation of cycle stability, as demonstrated previous reports, comes from not only the high coulombic efficiency at low C rates but also the cycling time^{72,73}. Therefore, we manifested the long-term cycle stability of DMPZ in 17 m NaClO₄ aqueous electrolyte at 0.2C rate and 1C rate with over 1000 hours cycling times in **Figure 3.13** and **3.14**, respectively (see **Figure 3.12b** for cycle stability at 5C rate). Superior cycle stability with high capacity retention and coulombic efficiency close to 100% were achieved at both

0.2C and 1C rates. An initial capacity of 231 mAh g⁻¹ and the capacity retention of ~87% after 200 cycles (over 1,000 hours) were obtained at low rate of 0.2C. Even after 1,000 cycles at 1C rate with over 1,630 hours, the capacity retention was maintained over 81% from the initial discharge capacity of 221 mAh g⁻¹ with highly reversible and stable redox centers at the molecular level (see **Figure 3.xx-3.xx** and **Chapter 3.3.6** for details). The cycle degradation rate of the DMPZ in high-concentration aqueous electrolyte was eventually reached below 0.5% per day over 1,000 cycles at 1C rate. This outstanding cycle durability performance as demonstrated thus far rigidly validate that the highly concentrated NaClO₄ aqueous electrolyte plays an effective role for preventing the dissolution of the DMPZ and successively suppressing the water decomposition, which during tremendous repeated charge-discharge cycles.

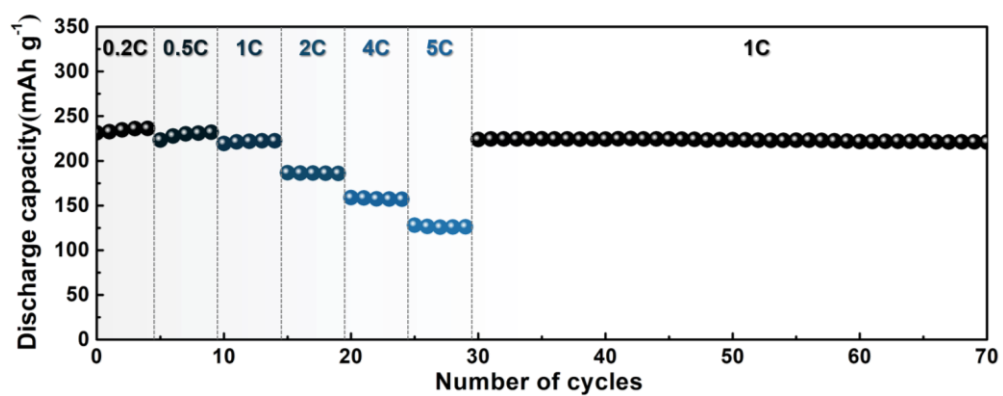


Figure 3.11. Rate performance of DMPZ cell at 0.2C, 0.5C, 1C, 2C, 4C, and 5C.

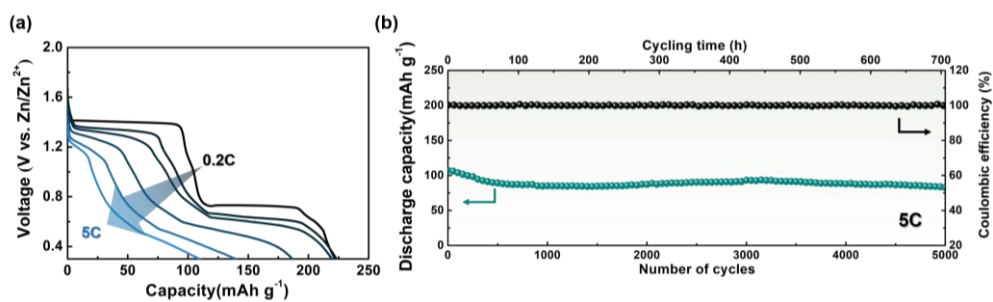


Figure 3.12. Rate performance of DMPZ cell at 0.2C, 0.5C, 1C, 2C, 4C, and 5C.

Rate performance of DMPZ in 17 m aqueous electrolyte. **(a)** Discharge profiles of the DMPZ in 17 m aqueous electrolyte at 0.2C, 0.5C, 1C, 2C, 4C, and 5C. **(b)** Cycle stability and coulombic efficiency of the DMPZ in 17 m aqueous electrolyte at 5C.

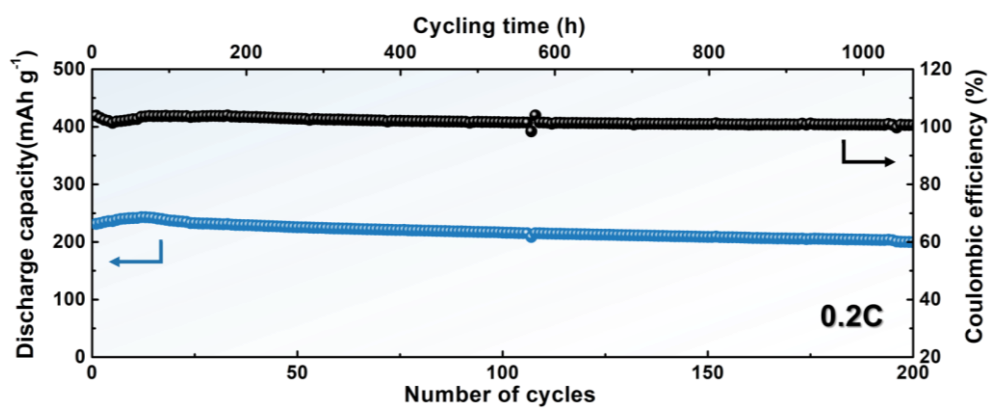


Figure 3.13. Cycle stability of DMPZ cell at 0.2C rate.

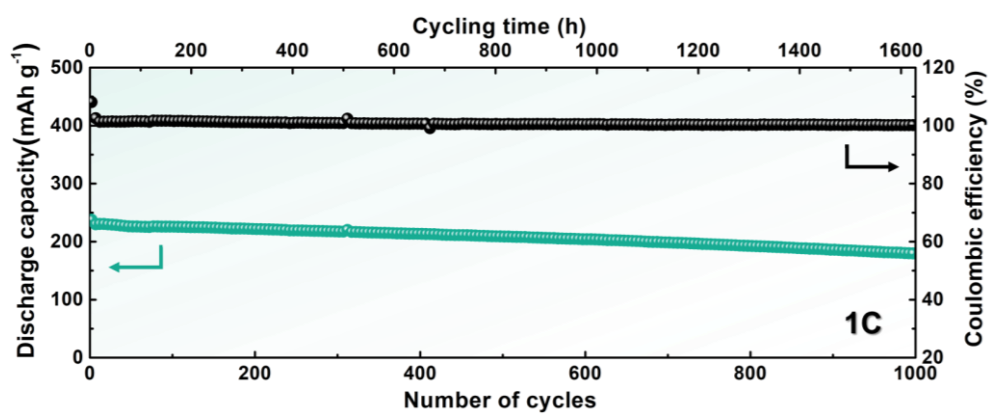


Figure 3.14. Cycle stability of DMPZ cell at 1C rate.

3.3.6 Structural and morphological analysis of the DMPZ cycled in the high-concentration aqueous electrolyte with long-term cycles

Figure 3.15 and **Figure 3.16** present the structural and mechanism analysis of the DMPZ after cycling in the high-concentration aqueous electrolyte. When the DMPZ was cycled in high-concentration aqueous electrolyte, the DMPZ delivered a highly reversible redox behavior with two well-defined voltage plateaus after formation cycles, as shown in **Figure 3.4b** and **Figure 3.7**. To confirm that the reversible redox behavior of DMPZ was sustained during the long-term cycle at 1C rate (**Figure 3.14**), we evaluated the charge-discharge profiles of DMPZ during 1-100 cycles and 100-1000 cycles as depicted in **Figure 3.15a** and **b**. During the charge-discharge process within 100 cycles in high-concentration aqueous electrolyte, the profiles of DMPZ with two well-defined voltage plateaus at initial cycles were transformed to S-shaped curves with maintaining the high specific capacity (**Figure 3.15a**). Then, the changed S-shaped curves were retained until 1000 cycles with a small amount of capacity decay ($\sim 50 \text{ mAh g}^{-1}$ of capacity loss), as shown in **Figure 3.15b**. The transformation of electrochemical profiles could be attributed to the changes in thermodynamic reaction mechanism or the structural changes of active materials. It is worth noting that the capacity of DMPZ was retained well even though the electrochemical profiles changed. Therefore, we assume that the transformation of the electrochemical curves of DMPZ in the high-concentration aqueous electrolyte was attributed to the structural changes of DMPZ without the mechanism changes. To verify our assumption about the structural changes of DMPZ, we measured the Ex-

situ X-ray diffraction of DMPZ after 1-, 50-, 100-cycling, as presented in **Figure 3.16a**. The DMPZ have a crystal structure, thus the DMPZ powder exhibited well-crystallized XRD patterns, which have the main peak at 11° , 13.15° , 15.2° , and 15.2° in 2θ degree. The XRD patterns of the pristine DMPZ electrode was consistent with the patterns of DMPZ powder. After the first charge process, the main peak of DMPZ at 11° and 13.15° was disappeared, but the peaks again returned reversibly, after the first discharge process. However, during the repeated charge-discharge process with 100 cycles, the main peaks were disappeared and the peak at 11° degree was broadened, implying that the crystallinity of DMPZ was disrupted and amorphized. According to the structural model (**Figure 3.16b**), three of the DMPZ molecules in their lattice structure are connected in the shape of enclosing each other with their size of 7.37 Å. The crystal structure of DMPZ at charged state seems to be easily disrupted due to the large size of ClO_4^- anion (ClO_4^- , ~ 2.4 Å), which consisted of two anions per one molecule. The lots of repeated charge-discharge process will be accelerated the amorphization of the crystalline DMPZ, and eventually, all of the DMPZ in the electrode transformed into the amorphous structure. The electrochemical profile transformation of DMPZ during cycling is attributed to this amorphization of the DMPZ electrode without mechanism changes. To further verify the maintaining of the redox centers at a molecular level, which indicates the reaction mechanism of DMPZ, XPS analysis was performed on the DMPZ electrode to obtain an in-depth redox mechanism view of the DMPZ. N 1s spectra of the DMPZ of the pristine and charged-discharged electrode after 1-, 50-, and 100-cycled are obtained

in **Figure 3.16c**. The redox center of DMPZ was revealed that the two single-electron redox reactions undergo reversibly around nitrogen atoms in the pyrazine ring of DMPZ during cycling^{37,50}. The peak centered at 399.7 eV of the pristine electrode in the N 1s spectra, which indicate the redox center of DMPZ, shifted to higher energy ($\Delta E = \sim 1$ eV) after the first charge process, then returned to the initial position after first discharge process. This peak shift is a well-known property of DMPZ as an indicator of the redox-active centers, which provides that the nitrogen atoms in DMPZ are redox-active centers attributed to the reversible conversion of non-conjugated sp^3 -NC- groups into conjugated sp^3 -NC- groups. This reversible peak change in the nitrogen atom was also observed in the charged-discharged electrode after 50-, and 100-cycled, implying the redox mechanism at the molecular level was not changed after long-term cycling, even though the electrochemical profiles were changed. Therefore, the redox centers of DMPZ were stably and reversibly sustained even after 1000 cycles, and only the crystal structure of DMPZ was transformed into amorphous.

In addition, to confirm the surface morphology changes of DMPZ electrode cycled in high-concentration aqueous electrolyte after long-term cycling, SEM analysis of DMPZ electrode was evaluated, as observed in **Figure 3.17**. **Figure 3.17a, c, e, and g** present the surface morphology of the DMPZ after 50-cycle charged, discharged, and 100-cycle charged, discharged, respectively. The surface of DMPZ cycled in high-concentration aqueous electrolyte after long-term cycles (both 50- and 100-cycles) appears to change a little bit porous morphology compared with the pristine

and initial cycled electrode (**Figure 3.9a-b**, and **Figure 3.10**) at both charged and discharged state. These results are related to the amorphization of DMPZ by oxidation with large size of ClO_4 anion during cycling, as shown in **Figure 3.15** and **Figure 3.16**. The large size of ClO_4 anion will induce not only amorphization of DMPZ but also volume change of DMPZ electrode during cycling. Therefore, the flat and condensed DMPZ in pristine electrode will be changed to a little porous morphology and amorphous structure after lots of charge-discharge repetition during cycling.

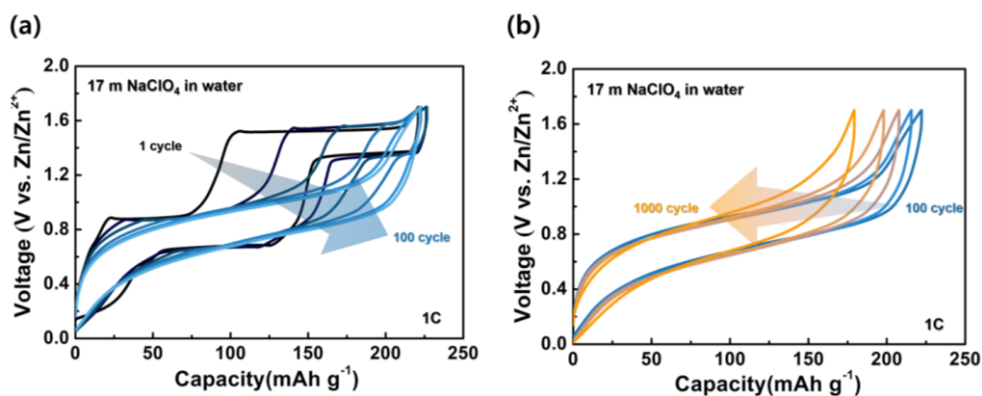


Figure 3.15. Structural analysis of the DMPZ after long-term cycling. **(a)** Charge-discharge profile changes of the DMPZ in 17 m aqueous electrolyte during 1 to 100 cycles. **(b)** Charge-discharge curves of the DMPZ in 17 m aqueous electrolyte during 100 to 1000 cycles.

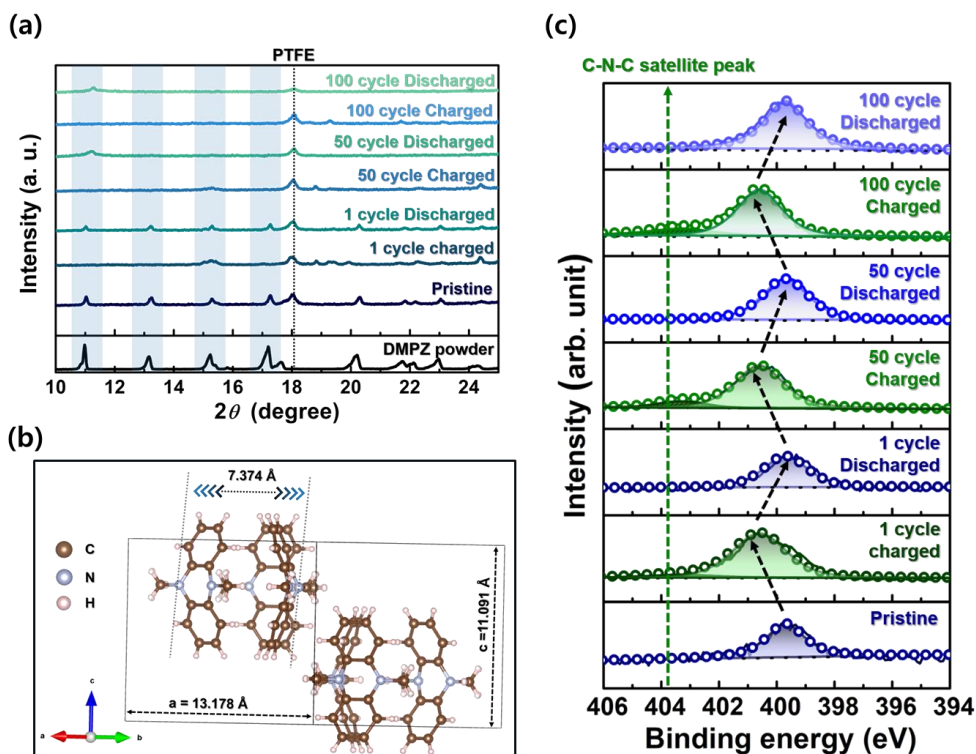


Figure 3.16. (a) Ex-situ XRD patterns of pristine, 1-, 50-, and 100-cycled DMPZ at the charged, discharged state of each cycle. (b) Schematic illustrations of crystal structures of DMPZ. The structural information of DMPZ has been adopted from CCDC (Cambridge Crystallographic Data Centre, www.ccdc.cam.ac.uk), whose detailed information is provided in the reference 74-75^{74,75}. (c) XPS profiles of N 1s spectra of DMPZ pristine and electrode after 1-, 50-, and 100-cycled at charged, discharged state of each cycle. Black arrow lines indicate the reversible reaction at redox center N of C-N-C groups in DMPZ^{37,50}. The green arrow line indicates the C-N-C satellite peak, which also indicates reversible redox reactions at redox center N of DMPZ.

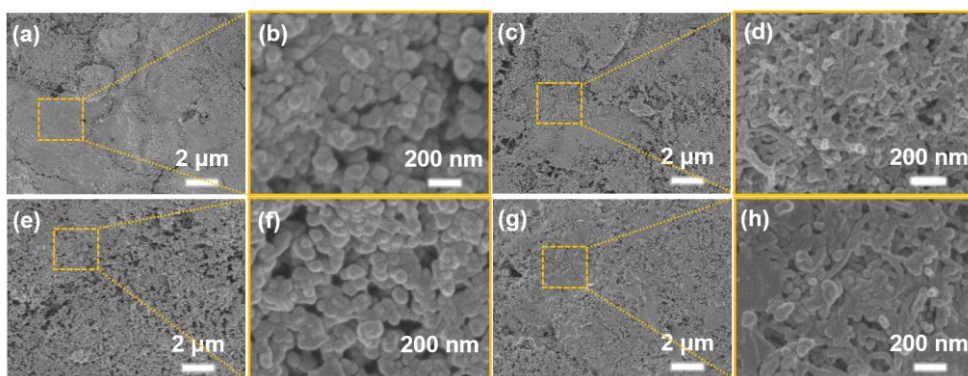


Figure 3.17. Surface morphologies of the DMPZ electrode after long-term cycling in 17 m aqueous electrolyte. **a, c, e, g**, SEM images of DMPZ electrode after **(a)** 50 cycle charged, **(c)** 50 cycle discharged, **(e)** 100 cycle charged, and **(g)** 100 cycle discharged. **(b), (d), (f),** and **(h)** presents the magnified SEM images of **(a), (c), (e),** and **(g)**, respectively.

3.3.7 Comparison of the performance of the DMPZ with previously reported works

To compare the performance of the DMPZ aqueous battery with previously demonstrated organic-based aqueous battery system, we comparatively depicted the corresponding performance with respect to the energy density (i.e. initial discharge capacity-based energy density of each battery system), the cycle degradation rate per day, and the calculated battery operational life based on the cumulative discharge capacity from the recent reported works as presented in **Figure 3.18**⁴²⁻⁴⁹. The details for calculation of the battery operational life and degradation percent per day are given in the **Table 3.2**. **Figure 3.18** shows that the DMPZ aqueous battery with high-concentration aqueous electrolyte far outperformed not only on the energy density but also the time-based durability (i.e. cycle degradation rate per day and battery operational life), compared with previously reported studies on the organic-based aqueous battery. Note that there is no any up-to-date cell performance enabling to exceed both the energy density of over 200 Wh kg⁻¹ and the battery operational life of over 800 hours. To the best of our knowledge, the DMPZ aqueous cell exhibited the highest long-term durability performance with delivering a remarkable energy density of ~250 Wh kg⁻¹ than reported thus far for cells implementing the organic electrodes with aqueous electrolyte.

The methodology to calculate the performance of the DMPZ (energy density, cycle degradation rate per day, and battery operational life), comparing the previously

reported works⁴²⁻⁴⁹, is provided in this section. The average voltage was estimated based on the discharge curves in the original paper, if not mentioned accurately in the previously reported study. For comparing the performance of the cells with equivalent parameters, we assumed and roughly calculated the comparison parameters from the reported data in the previous study.

Energy density: For equivalent comparison of the performance, we calculated the energy density of each cell based on the initial discharge capacity and average discharge voltage, as the following equation:

$$\text{Energy density (Wh kg}^{-1}\text{)} = C_{\text{initial}} \times V_{\text{avg}} \quad (7)$$

Where V_{avg} denotes the average discharge voltage and C_{initial} indicates the initial discharge capacity.

Battery operational life: An operated discharge time of the DMPZ and the previously reported works was roughly estimated. In the previously reported works, the battery operational time was not mentioned in general. Therefore, we calculate and estimate the battery operational life (time) from the performance parameters such as cumulative discharge capacity (mAh g⁻¹) of total cycles, current rate (mA g⁻¹), and number of cycles (N) in previous studies

$$C_{\text{cumulative}} = \frac{C_{\text{initial}} + C_{\text{final}}}{2} \times N \quad (8)$$

Where $C_{\text{cumulative}}$ denotes the cumulative discharge capacity of the total cycles in

all of the studies. N means number of cycles, and $C_{initial}$, C_{final} indicate the discharge capacity of initial and final cycles, respectively. Using cumulative discharge capacity, we estimate the battery operational life (time), as follows:

$$\text{Battery operational life (h)} = \frac{C_{cumulative}}{j} \quad (9)$$

Where j denotes the current rate. Note that we excluded the cycle degradation information of the all of batteries for equal comparison. Instead, the information about the cycle degradation is included in the cycle degradation rate per day.

Cycle degradation rate per day: This parameter presents the cycle degradation with time parameters. Cycle degradation rate was estimated based on the difference of discharge capacity between initial and final cycles in the original paper, if not mentioned explicitly in the given paper. After calculated or used the given cycle degradation rate, it is divided by battery operational time (day).

$$\text{Cycle degradation rate per day (\%)} = \frac{\left(\frac{C_{initial} - C_{final}}{C_{initial}} \times 100\right)}{\text{Battery operational life} \times \frac{1}{24}} \quad (8)$$

Where $C_{initial}$ and C_{final} denote the discharge capacity of initial and final cycles, respectively.

Table 3.2. Comparison of the performance of the DMPZ with previously reported works.

Materials	Average voltage (V)	Initial discharge capacity (mAh g ⁻¹)	Current rate (mA g ⁻¹)	Cycle number	Energy density (Wh kg ⁻¹)	Cycle degradation rate per day (%)	Battery operational life (h)
P-chloranil ⁴³	1.1	118	217	200	129.8	7.69	93
Cailx4quinone (C4Q) ⁴⁴	1	150	500	1,000	150	1.11	281
Pyrene-4,5,9,10-tetraone (PTO) ⁴²	0.74	213	3,000	1,000	157.6	12.84	60

Sulfur							
heterocycli							
c							
quinone							
dibenzo							
[b,i]	0.8	97	2,000	23,000	77.6	0.38	1,025
thianthrene							
-5,7,12,14-							
tetraone							
(DTT) ⁴⁸							
DTT ⁴⁸	0.8	200	100	150	160	0.5	291
3,4,9,10-							
perylene tetra-							
carboxylic							
c							
dianhydride	0.6	100	8,000	1,000	60	72.6	11
e							
(Pi-PMC							
or π -							
PMC) ⁴⁹							

Triangular phenanthrene nequinone- based macrocycl e (PQ delta or PQ- Δ) ⁴⁶ 1,4 bis(diphen ylamino) Benzene (BDB) ⁴⁵	0.78	210	150	500	163.8	0.03	697
BDB ⁴⁵	1.25	112	390	500	140	3.31	131
BDB ⁴⁵	1.25	80	780	1,000	100	6.69	90
diquinoxali no [2,3- a:2',3'-c] phenazine (HATN) ⁴⁷	0.6	150	5,000	5,000	90	1.1	145

5,10- dihydro- 5,10- dimethyl phenazine (DMPZ, This work) DMZP (This work)	1.1	221	255	1,000	243	0.5	810
	1.1	231	51	200	254	0.37	870

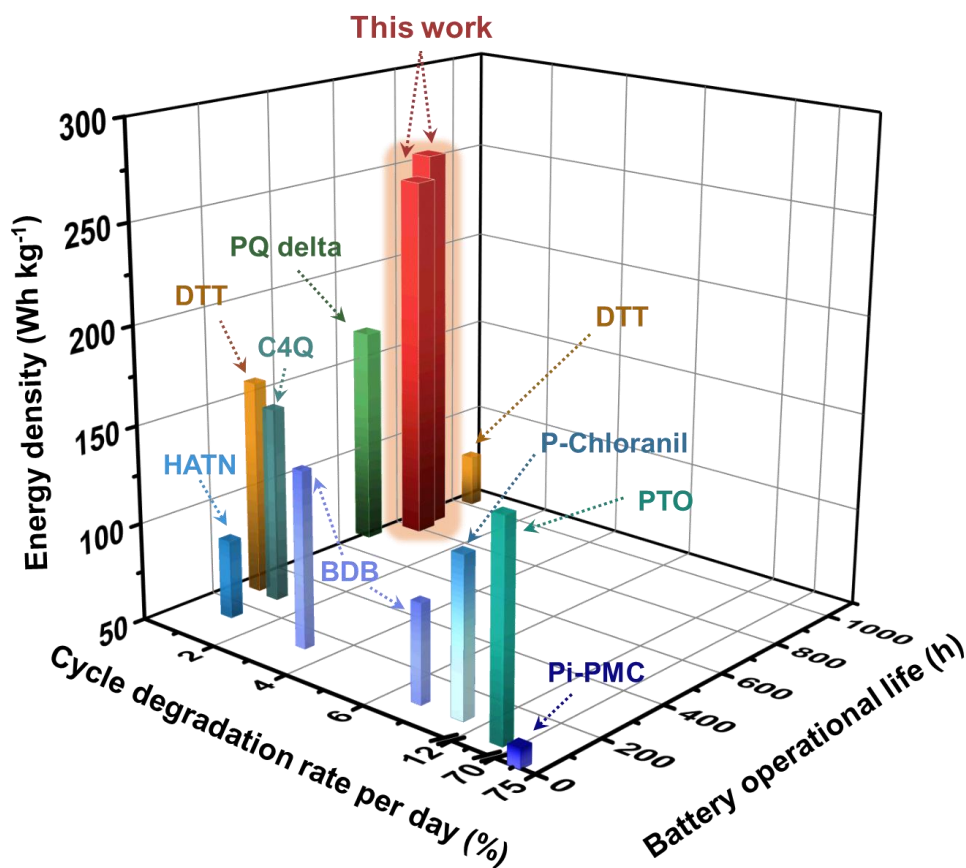


Figure 3.18. Comparison of performance of DMPZ aqueous battery with that of previously demonstrated organic-based aqueous battery system⁴²⁻⁴⁹. This plot summarizes the energy density (*i.e.*, initial discharge-capacity-based energy density of each battery system, z-axis), cycle degradation rate per day (x-axis), and calculated battery operational life (y-axis) based on the cumulative discharge capacity from recently reported works (see **Table 3.2** and **Chapter 3.3.7** for the calculation details of the battery operational life, degradation rate per day, and detailed references with abbreviations for each material).

3.4 Concluding remarks

We introduce a noble strategy to demonstrate full utilization of the DMPZ electrode by employing the most proper electrolyte that provide low solubility of DMPZ, thus improving the cycle durability. From the rational prediction and experimental confirmation of the DMPZ solubility with respect to the solvation free energy according to machine learning technique, aqueous electrolyte was adopted for improving the cycle durability of the DMPZ by suppressing its dissolution. A capacity retention in 1 m NaClO₄ aqueous electrolyte could be reversibly maintained over 200 cycles with the value reaching 85% with one single-electron redox reaction, but it was hard to provide the reversible second redox reaction due to the water splitting. To completely facilitate the multi-redox reaction of the DMPZ with suppressing water decomposition and dissolution of the active materials, high-concentration NaClO₄ aqueous electrolyte was employed. It was revealed that this high-concentration aqueous electrolyte can offer (i) widening the electrochemical stable voltage window of the aqueous solution, (ii) providing more enhanced diminishing the solubility of the DMPZ compared with low-concentration aqueous and non-aqueous electrolyte, and (iii) stabilizing the DMPZ redox reaction by downshifting the redox potential of DMPZ following the Nernst equation. It led to outstanding capacity retention of ~87% over 200 cycles (over 1,000 hours) at 0.2C and superior long-life durability with cycle degradation rate of below 0.5% per day even after 1,000 cycles at 1C (over 1,630 hours). Our findings suggest that the fundamental understanding about the compatibility between the active organic

material and solvent will offer a novel paradigm toward the realization for the practical implementation of the organic battery with achieving the long-term stability.

3.5 References

1. Huggins, R. A. *Advanced Batteries: Materials Science Aspects*. (Springer, 2008).
2. Dunn, B., Kamath, H. & Tarascon, J.-M. Electrical Energy Storage for the Grid: A Battery of Choices. *Science* **334**, 928, doi:10.1126/science.1212741 (2011).
3. Winter, M., Barnett, B. & Xu, K. Before Li Ion Batteries. *Chem. Rev.* **118**, 11433-11456, doi:10.1021/acs.chemrev.8b00422 (2018).
4. Choi, N.-S. *et al.* Challenges Facing Lithium Batteries and Electrical Double-Layer Capacitors. *Angew. Chem. Int. Ed.* **51**, 9994-10024, doi:https://doi.org/10.1002/anie.201201429 (2012).
5. Vikström, H., Davidsson, S. & Höök, M. Lithium availability and future production outlooks. *Appl. Energy* **110**, 252-266, doi:https://doi.org/10.1016/j.apenergy.2013.04.005 (2013).
6. Kalhoff, J., Eshetu, G. G., Bresser, D. & Passerini, S. Safer Electrolytes for Lithium-Ion Batteries: State of the Art and Perspectives. *ChemSusChem* **8**, 2154-2175, doi:https://doi.org/10.1002/cssc.201500284 (2015).

7. Sharma, S. S. & Manthiram, A. Towards more environmentally and socially responsible batteries. *Energy Environ. Sci.* **13**, 4087-4097, doi:10.1039/D0EE02511A (2020).
8. Armand, M. & Tarascon, J. M. Building better batteries. *Nature* **451**, 652-657, doi:10.1038/451652a (2008).
9. Larcher, D. & Tarascon, J. M. Towards greener and more sustainable batteries for electrical energy storage. *Nat. Chem.* **7**, 19-29, doi:10.1038/nchem.2085 (2015).
10. Lewis, N. S. Research opportunities to advance solar energy utilization. *Science* **351**, aad1920, doi:10.1126/science.aad1920 (2016).
11. Poizot, P. & Dolhem, F. Clean energy new deal for a sustainable world: from non-CO₂ generating energy sources to greener electrochemical storage devices. *Energy Environ. Sci.* **4**, 2003-2019, doi:10.1039/C0EE00731E (2011).
12. Schon, T. B., McAllister, B. T., Li, P.-F. & Seferos, D. S. The rise of organic electrode materials for energy storage. *Chem. Soc. Rev.* **45**, 6345-6404, doi:10.1039/C6CS00173D (2016).

13. Lee, S. *et al.* Recent Progress in Organic Electrodes for Li and Na Rechargeable Batteries. *Adv. Mater.* **30**, 1704682, doi:<https://doi.org/10.1002/adma.201704682> (2018).
14. Huang, J., Dong, X., Guo, Z. & Wang, Y. Progress of Organic Electrodes in Aqueous Electrolyte for Energy Storage and Conversion. *Angew. Chem. Int. Ed.* **59**, 18322-18333, doi:<https://doi.org/10.1002/anie.202003198> (2020).
15. Lee, S., Hong, J. & Kang, K. Redox-Active Organic Compounds for Future Sustainable Energy Storage System. *Adv. Energy Mater.* **10**, 2001445, doi:<https://doi.org/10.1002/aenm.202001445> (2020).
16. Lu, Y. & Chen, J. Prospects of organic electrode materials for practical lithium batteries. *Nat. Rev. Chem.* **4**, 127-142, doi:[10.1038/s41570-020-0160-9](https://doi.org/10.1038/s41570-020-0160-9) (2020).
17. Qin, K., Huang, J., Holguin, K. & Luo, C. Recent advances in developing organic electrode materials for multivalent rechargeable batteries. *Energy Environ. Sci.* **13**, 3950-3992, doi:[10.1039/D0EE02111C](https://doi.org/10.1039/D0EE02111C) (2020).
18. Lee, M. *et al.* Multi-electron redox phenazine for ready-to-charge organic batteries. *Green Chem.* **19**, 2980-2985, doi:[10.1039/C7GC00849J](https://doi.org/10.1039/C7GC00849J) (2017).

19. Kwon, G. *et al.* Multi-redox Molecule for High-Energy Redox Flow Batteries. *Joule* **2**, 1771-1782, doi:https://doi.org/10.1016/j.joule.2018.05.014 (2018).
20. Kwon, G. *et al.* Bio-inspired Molecular Redesign of a Multi-redox Catholyte for High-Energy Non-aqueous Organic Redox Flow Batteries. *Chem* **5**, 2642-2656, doi:https://doi.org/10.1016/j.chempr.2019.07.006 (2019).
21. Ham, Y. *et al.* Multi-redox phenazine/non-oxidized graphene/cellulose nanohybrids as ultrathick cathodes for high-energy organic batteries. *Nano Res.*, doi:10.1007/s12274-020-3187-9 (2020).
22. Lau, V. W.-h., Moudrakovski, I., Yang, J., Zhang, J. & Kang, Y.-M. Uncovering the Shuttle Effect in Organic Batteries and Counter-Strategies Thereof: A Case Study of the N,N'-Dimethylphenazine Cathode. *Angew. Chem. Int. Ed.* **59**, 4023-4034, doi:https://doi.org/10.1002/anie.201912587 (2020).
23. Lee, K. *et al.* Phenoxazine as a high-voltage p-type redox center for organic battery cathode materials: small structural reorganization for faster charging and narrow operating voltage. *Energy Environ. Sci.* **13**, 4142-4156, doi:10.1039/D0EE01003K (2020).

24. Lee, S. *et al.* Utilizing Latent Multi-Redox Activity of p-Type Organic Cathode Materials toward High Energy Density Lithium-Organic Batteries. *Adv. Energy Mater.* **10**, 2001635, doi:<https://doi.org/10.1002/aenm.202001635> (2020).

25. Li, W., Erickson, E. M. & Manthiram, A. High-nickel layered oxide cathodes for lithium-based automotive batteries. *Nat. Energy* **5**, 26-34, doi:[10.1038/s41560-019-0513-0](https://doi.org/10.1038/s41560-019-0513-0) (2020).

26. Li, W., Lee, S. & Manthiram, A. High-Nickel NMA: A Cobalt-Free Alternative to NMC and NCA Cathodes for Lithium-Ion Batteries. *Adv. Mater.* **32**, 2002718, doi:<https://doi.org/10.1002/adma.202002718> (2020).

27. Kim, Y., Seong, W. M. & Manthiram, A. Cobalt-free, high-nickel layered oxide cathodes for lithium-ion batteries: Progress, challenges, and perspectives. *Energy Storage Mater.* **34**, 250-259, doi:<https://doi.org/10.1016/j.ensm.2020.09.020> (2021).

28. Liang, Y., Zhang, P., Yang, S., Tao, Z. & Chen, J. Fused Heteroaromatic Organic Compounds for High-Power Electrodes of Rechargeable Lithium Batteries. *Adv. Energy Mater.* **3**, 600-605, doi:<https://doi.org/10.1002/aenm.201200947> (2013).

29. Song, Z. & Zhou, H. Towards sustainable and versatile energy storage devices: an overview of organic electrode materials. *Energy Environ. Sci.* **6**, 2280-2301, doi:10.1039/C3EE40709H (2013).
30. Bhosale, M. E., Chae, S., Kim, J. M. & Choi, J.-Y. Organic small molecules and polymers as an electrode material for rechargeable lithium ion batteries. *J. Mater. Chem. A* **6**, 19885-19911, doi:10.1039/C8TA04906H (2018).
31. Nokami, T. *et al.* Polymer-Bound Pyrene-4,5,9,10-tetraone for Fast-Charge and -Discharge Lithium-Ion Batteries with High Capacity. *J. Am. Chem. Soc.* **134**, 19694-19700, doi:10.1021/ja306663g (2012).
32. Huang, W. *et al.* Quasi-Solid-State Rechargeable Lithium-Ion Batteries with a Calix[4]quinone Cathode and Gel Polymer Electrolyte. *Angew. Chem. Int. Ed.* **52**, 9162-9166, doi:https://doi.org/10.1002/anie.201302586 (2013).
33. Muench, S. *et al.* Polymer-Based Organic Batteries. *Chem. Rev.* **116**, 9438-9484, doi:10.1021/acs.chemrev.6b00070 (2016).
34. Wang, S. *et al.* Exfoliation of Covalent Organic Frameworks into Few-Layer Redox-Active Nanosheets as Cathode Materials for Lithium-Ion Batteries. *J. Am. Chem. Soc.* **139**, 4258-4261, doi:10.1021/jacs.7b02648 (2017).

35. Chi, X. *et al.* Tailored Organic Electrode Material Compatible with Sulfide Electrolyte for Stable All-Solid-State Sodium Batteries. *Angew. Chem. Int. Ed.* **57**, 2630-2634, doi:<https://doi.org/10.1002/anie.201712895> (2018).
36. Luo, Z. *et al.* A Microporous Covalent–Organic Framework with Abundant Accessible Carbonyl Groups for Lithium-Ion Batteries. *Angew. Chem. Int. Ed.* **57**, 9443-9446, doi:<https://doi.org/10.1002/anie.201805540> (2018).
37. Bai, S. *et al.* Permselective metal–organic framework gel membrane enables long-life cycling of rechargeable organic batteries. *Nat. Nanotechnol.* **16**, 77-84, doi:[10.1038/s41565-020-00788-x](https://doi.org/10.1038/s41565-020-00788-x) (2021).
38. Dai, G. *et al.* The Design of Quaternary Nitrogen Redox Center for High-Performance Organic Battery Materials. *Matter* **1**, 945-958, doi:<https://doi.org/10.1016/j.matt.2019.05.009> (2019).
39. Lee, M. H. *et al.* Toward a low-cost high-voltage sodium aqueous rechargeable battery. *Mater. Today* **29**, 26-36, doi:<https://doi.org/10.1016/j.mattod.2019.02.004> (2019).
40. Borodin, O., Self, J., Persson, K. A., Wang, C. & Xu, K. Uncharted Waters: Super-Concentrated Electrolytes. *Joule* **4**, 69-100, doi:<https://doi.org/10.1016/j.joule.2019.12.007> (2020).

41. Li, M., Wang, C., Chen, Z., Xu, K. & Lu, J. New Concepts in Electrolytes. *Chem. Rev.* **120**, 6783-6819, doi:10.1021/acs.chemrev.9b00531 (2020).
42. Guo, Z. *et al.* An Environmentally Friendly and Flexible Aqueous Zinc Battery Using an Organic Cathode. *Angew. Chem. Int. Ed.* **57**, 11737-11741, doi:https://doi.org/10.1002/anie.201807121 (2018).
43. Kundu, D. *et al.* Organic Cathode for Aqueous Zn-Ion Batteries: Taming a Unique Phase Evolution toward Stable Electrochemical Cycling. *Chem. Mater.* **30**, 3874-3881, doi:10.1021/acs.chemmater.8b01317 (2018).
44. Zhao, Q. *et al.* High-capacity aqueous zinc batteries using sustainable quinone electrodes. *Sci. Adv.* **4**, 1761, doi:10.1126/sciadv.aao1761 (2018).
45. Glatz, H., Lizundia, E., Pacifico, F. & Kundu, D. An Organic Cathode Based Dual-Ion Aqueous Zinc Battery Enabled by a Cellulose Membrane. *ACS Appl. Energy Mater.* **2**, 1288-1294, doi:10.1021/acsaem.8b01851 (2019).
46. Nam, K. W. *et al.* Redox-Active Phenanthrenequinone Triangles in Aqueous Rechargeable Zinc Batteries. *J. Am. Chem. Soc.* **142**, 2541-2548, doi:10.1021/jacs.9b12436 (2020).
47. Tie, Z., Liu, L., Deng, S., Zhao, D. & Niu, Z. Proton insertion chemistry of

- a zinc–organic battery. *Angew. Chem. Int. Ed.* **59**, 4920-4924 (2020).
48. Wang, Y. *et al.* Binding Zinc Ions by Carboxyl Groups from Adjacent Molecules toward Long-Life Aqueous Zinc–Organic Batteries. *Adv. Mater.* **32**, 2000338, doi:<https://doi.org/10.1002/adma.202000338> (2020).
49. Zhang, H., Fang, Y., Yang, F., Liu, X. & Lu, X. Aromatic organic molecular crystal with enhanced π – π stacking interaction for ultrafast Zn-ion storage. *Energy Environ. Sci.* **13**, 2515-2523, doi:10.1039/D0EE01723J (2020).
50. Wang, F. *et al.* Highly reversible zinc metal anode for aqueous batteries. *Nat. Mater.* **17**, 543-549, doi:10.1038/s41563-018-0063-z (2018).
51. Lim, H. & Jung, Y. Delfos: deep learning model for prediction of solvation free energies in generic organic solvents. *Chem. Sci.* **10**, 8306-8315, doi:10.1039/C9SC02452B (2019).
52. Marenich, A. V., Cramer, C. J. & Truhlar, D. G. Universal Solvation Model Based on Solute Electron Density and on a Continuum Model of the Solvent Defined by the Bulk Dielectric Constant and Atomic Surface Tensions. *J. Phys. Chem. B* **113**, 6378-6396, doi:10.1021/jp810292n (2009).
53. Mobley, D. L. & Guthrie, J. P. FreeSolv: a database of experimental and

- calculated hydration free energies, with input files. *J. Comput.-Aided Mol. Des.* **28**, 711-720, doi:10.1007/s10822-014-9747-x (2014).
54. Hille, C. *et al.* Generalized molecular solvation in non-aqueous solutions by a single parameter implicit solvation scheme. *J. Chem. Phys.* **150**, 041710, doi:10.1063/1.5050938 (2018).
 55. Hille, C. *et al.* (ed Technical University of Munich) (2018).
 56. Neese, F. The ORCA program system. *WIREs Comput. Mol. Sci.* **2**, 73-78, doi:https://doi.org/10.1002/wcms.81 (2012).
 57. Hildebrand, J. H. & Scott, R. L. The Entropy of Solution of Nonelectrolytes. *J. Chem. Phys.* **20**, 1520-1521, doi:10.1063/1.1700206 (1952).
 58. Barton, A. F. M. Solubility parameters. *Chem. Rev.* **75**, 731-753, doi:10.1021/cr60298a003 (1975).
 59. Yalkowsky, S. H. & Valvani, S. C. Solubility and partitioning I: Solubility of nonelectrolytes in water. *J. Pharm. Sci.* **69**, 912-922, doi:https://doi.org/10.1002/jps.2600690814 (1980).
 60. Jain, N. & Yalkowsky, S. H. Estimation of the aqueous solubility I:

- Application to organic nonelectrolytes. *J. Pharm. Sci.* **90**, 234-252, doi:[https://doi.org/10.1002/1520-6017\(200102\)90:2<234::AID-JPS14>3.0.CO;2-V](https://doi.org/10.1002/1520-6017(200102)90:2<234::AID-JPS14>3.0.CO;2-V) (2001).
61. Gharagheizi, F., Eslamimanesh, A., Farjood, F., Mohammadi, A. H. & Richon, D. Solubility Parameters of Nonelectrolyte Organic Compounds: Determination Using Quantitative Structure–Property Relationship Strategy. *Ind. Eng. Chem. Res.* **50**, 11382-11395, doi:10.1021/ie200962w (2011).
 62. Xu, K. Nonaqueous Liquid Electrolytes for Lithium-Based Rechargeable Batteries. *Chem. Rev.* **104**, 4303-4418, doi:10.1021/cr030203g (2004).
 63. Zhong, C. *et al.* A review of electrolyte materials and compositions for electrochemical supercapacitors. *Chem. Soc. Rev.* **44**, 7484-7539, doi:10.1039/C5CS00303B (2015).
 64. Sato, H. A modern solvation theory: quantum chemistry and statistical chemistry. *Phys. Chem. Chem. Phys.* **15**, 7450-7465, doi:10.1039/C3CP50247C (2013).
 65. Huang, W., Blinov, N. & Kovalenko, A. Octanol–Water Partition Coefficient from 3D-RISM-KH Molecular Theory of Solvation with Partial Molar Volume Correction. *J. Phys. Chem. B* **119**, 5588-5597,

doi:10.1021/acs.jpcb.5b01291 (2015).

66. Skyner, R. E., McDonagh, J. L., Groom, C. R., van Mourik, T. & Mitchell, J. B. O. A review of methods for the calculation of solution free energies and the modelling of systems in solution. *Phys. Chem. Chem. Phys.* **17**, 6174-6191, doi:10.1039/C5CP00288E (2015).
67. Wu, Z. *et al.* MoleculeNet: a benchmark for molecular machine learning. *Chem. Sci.* **9**, 513-530, doi:10.1039/C7SC02664A (2018).
68. Jaeger, S., Fulle, S. & Turk, S. Mol2vec: Unsupervised Machine Learning Approach with Chemical Intuition. *J. Chem. Inf. Model.* **58**, 27-35, doi:10.1021/acs.jcim.7b00616 (2018).
69. Zhang, K., Guo, C., Zhao, Q., Niu, Z. & Chen, J. High-Performance Organic Lithium Batteries with an Ether-Based Electrolyte and 9,10-Anthraquinone (AQ)/CMK-3 Cathode. *Adv. Sci.* **2**, 1500018, doi:https://doi.org/10.1002/advs.201500018 (2015).
70. Lucasse, W. W. ACTIVITY COEFFICIENTS AND TRANSFERENCE NUMBERS OF THE ALKALINE EARTH CHLORIDES. *J. Am. Chem. Soc.* **47**, 743-754, doi:10.1021/ja01680a021 (1925).

71. John O'M. Bockris, A. K. N. R. *Modern Electrochemistry I: Ionics*. Vol. Volume1 (Springer US, 2007).

72. Burns, J. C. *et al.* Evaluation of Effects of Additives in Wound Li-Ion Cells Through High Precision Coulometry. *J. Electrochem. Soc.* **158**, A255, doi:10.1149/1.3531997 (2011).

73. Suo, L. *et al.* "Water-in-salt" electrolyte enables high-voltage aqueous lithium-ion chemistries. *Science* **350**, 938, doi:10.1126/science.aab1595 (2015).

74. Keller, H. J., Moroni, W., Nöthe, D., Scherz, M. & Weiss, J. Kristall- und Molekülstruktur von 5.10-Dihydro-5.10-diniethylphenaziniumtriiodid und 5.10-Dihydro-5.10-diethylphenaziniumtriiodid / Molecular and Crystal Structure of 5,10-Dihydro-5.10-dimethylphenaziniumtriiodide and 5.10-Dihydro-5.10-diethylphenazinium triiodide. *Z. Naturforsch. B* **33**, 838-842, doi:doi:10.1515/znb-1978-0805 (1978).

75. Holzapfel, M., Lambert, C., Selinka, C. & Stalke, D. Organic mixed valence compounds with N,N-dihydrodimethylphenazine redox centres. *J. Chem. Soc., Perkin Trans. 2*, 1553-1561, doi:10.1039/B204392K (2002).

Chapter 4. Conclusion

From renewable energy production/storage to electric-powered vehicles, rechargeable batteries are indispensable and an important enabler of environmentally benign energy solutions. Although the conventional lithium-ion batteries present a promising outlook, lots of hurdles to their use for such large-scale energy storage system and their mass-production have yet to be overcome, owing to increase costs stemming from the limited abundance of raw materials and safety concerns arising from the use of highly flammable organic electrolytes. In this regard, aqueous electrolytes emerge as a potential game changer in LIB market due to its non-flammability, non-toxicity, and low-cost resources. However, aqueous electrolytes give a narrow electrochemical stability window of ~ 1.23 V away from which gives rise to thermodynamic water decomposition such as hydrogen and oxygen evolution. This inevitably acts as a bottleneck for the limited choice of electrode materials that in turn provide a limited energy density for the aqueous system, making it unfit for practical application.

Recently, highly concentrated electrolytes have attracted a tremendous interest for both aqueous and non-aqueous systems owing to their remarkable characteristics distinct from dilute electrolytes, which include low solvent activity, low flammability, and ability to suppress side reactions. Especially, super-concentrated electrolytes in an aqueous electrolyte system have already outperformed conventional electrolytes by suppressing water activity and thus expanding its stability window of electrochemical operation. Despite the surging interest of super-concentration

electrolyte aqueous system for a non-flammable, high energy density aqueous battery in energy market, the economic concern with regards to high-cost organic solutes in the aqueous electrolyte hinders the commercialization of aqueous batteries for grid-scale energy storage systems and, thus, brings up an urgent need for the design rule that accounts for cost efficiency. Therefore, the vital need for the discovery and development of low-cost salt for the high-concentration aqueous electrolytes is signified.

Exploiting a new low-cost salts for high-concentration aqueous electrolytes is the most important process in developmetn of low-cost and high-energy denstiy aqueous battery. For screanning and finding a new salts for low-cost high-concentration aqueous electrolyte, important criteria was defined based on previous reported high-costs salts in Chapter 2. Based on those criteria, I carefully examine the water structure-modifying effect of the commonly used low-cost inorganic solutes in the saturated high-concentration aqueous systems, in conjunction with previously reported super-concentrated electrolytes using organic salts. Upon close inspection, it is identified that saturated NaClO_4 (17 m) solution is the most suitable candidate for a low-cost high-voltage sodium aqueous electrolyte. This electrolyte exhibits a wide electrochemical stability window of up to ~ 2.7 V via suppressed water decomposition from solvation structure changes and formation of a robust solid-electrolyte interphase (SEI) layer. This electrolyte could be successfully demonstrated that a 2-V $\text{Na}_4\text{Fe}_3(\text{PO}_4)_2(\text{P}_2\text{O}_7)/\text{NaTi}_2(\text{PO}_4)_3$ full cell in 17 m of NaClO_4 electrolyte provides remarkable cycle stability and a coulombic efficiency. In

addition, it is found that the formation of a protective layer composed of Na_2CO_3 and Na-O compounds on electrode surface led to excellent stability of the full-cell with remarkable storage stability for ~ 900 hours. Surprisingly, the SEI layer formation does not follow the conventional wisdom of anion reduction of salts as in the aqueous electrolyte with organic salts. Hence, this study proposes a new mechanism of the protective layer formation on the anode via a different route from what has been widely accepted in literature.

Although the low-cost high-concentration electrolyte was demonstrated and it could be widened their electrochemical stability window, limitation of its energy density still remained. Thus, to make more sustainable and design flexible system with high-energy density, further feasible investigation on cell configuration of the high-concentration aqueous electrolyte system could be tunable. In this regard, the multi-electron-redox phenazine molecule (DMPZ) as a cathode in aqueous battery with zinc anode was adopted for greener and sustainable system. Despite the marvelous potential of DMPZ for high-energy density cathode material, remaining challenges related to the dissolution of the electrode material and the resulting poor cycle life with undesirable shuttle effects, which are general issues in organic batteries, make it unsuitable for practical implementation. In this regard, more fundamental approaches are necessary to understand and mitigate the dissolution problems of DMPZ, and rational electrolyte engineering can be a crucial solution for demonstrating high-performance organic batteries. Therefore, the strategy for boosting the durability of DMPZ through the rational design of electrolytes

that exhibits optimal performance with DMPZ was proposed in chapter 3. From the careful predicting and exploiting the dissolution tendency of DMPZ for the various solvents, the high-concentration aqueous electrolyte (17 m NaClO₄) was finally adopted as the most suitable electrolyte to effectively suppress the dissolution. The aid of high-concentration aqueous electrolyte, the long-term cycle durability of the DMPZ electrode is obtained with outstanding capacity fading rate, which is one of the best performances in organic aqueous battery systems.

In conclusion, the rational desing and fundamental strategy for approaching the low-cost, greener, and sustainable aqueous battery with high-energy density was investigated and suscesffuly further demonstration of battery performance was conducted in this thesis. The two key highlights in this thesis from using low-cost inorganic salt-based super-concentration aqueous electrolytes are: 1) realization of comparable electrochemical performance to state-of-the-art organic counterparts and discovery of robust surface layer formation, composed of Na₂CO₃ and Na-O compounds, without the reduction of the salts, and 2) facilitation to the complete utilization of the capacity and drastically improve the cycle durability by employing an electrolyte that is the most compatible with a DMPZ electrode with fundamental and experimental validation. I believe that the new insight, which on the low-cost solutes with fundamental solvation study and the dissolution properties of DMPZ in high-concentration aqueous electrolytes, broaden our understanding of super-

concentration aqueous electrolytes and provide an essential guidance towards low-cost, high-energy density and sustainable high-concentration aqueous battery system.

Abstract in Korean

초록

자연 친화적이고 지속가능한 에너지 저장 시스템에 대한 요구가 급증하고 있으며, 이에 따라 리튬이온 이차전지의 대량생산이 현재 에너지 시장에서 매우 증가하고 있다. 기존 상용화된 리튬이온 이차전지의 유망한 전망에도 불구하고, 대용량 저장 관련 적용분야에 대한 사용에 대하여 제한적인 원자재로 인한 비용상승문제와 가연성 특성이 높은 유기계 전해질을 사용함에 따른 안전성 문제로 인하여 극복해야 할 많은 문제들이 아직 남아 있다. 이에 따라 더욱 안전한 대체 방안으로서 물 기반의 수성 전해질을 사용하는 배터리가 연구되어 왔습니다. 하지만, 전통적으로 사용하는 물 기반의 수계 전해질은 1.23 V의 전압을 넘으면 물분해가 일어나는 좁은 전기화학적 안정성을 제공합니다. 물의 좁은 전기화학적 안정성은 필연적으로 수계 배터리 시스템에 제한된 에너지 밀도를 제공하며 이에 따라 실제 산업으로의 적용을 어렵게 만들고 있다. 수계 배터리 시스템의 에너지 밀도를 높이기 위하여, 최근 개발된 고농도 수계 전해질 시스템은 녹아 있는 염의 분해를 통해 안전한 고체-전해질 계면 층 (SEI)을 형성하여 보다 넓은 전기화학적 안전성을 확보하였고 물의 분해를 억제함으로써, 고전압 수계 배터리 시스템으로의 새로운 길을 열어주었다. 비록 고농도

전해질이 높은 에너지 밀도를 갖는 수계 배터리 시스템을 가능하게 하였지만, 이 시스템 역시 매우 값비싼 유기계 염을 매우 많은 양 녹여서 사용해야 한다는 점에서 아직 많은 문제가 존재하였다. 본 학위 논문에서는 저렴하면서 높은 에너지 밀도를 가질 수 있는 수계 시스템을 만들기 위한 디자인 전략을 소개하였다. 특히, 고농도 NaClO_4 수계 전해질 기반의 배터리 시스템을 개발하여 물 분해를 억제하며 보다 넓은 범위의 전기화학적 안정성을 가진 시스템을 소개하였고, 이 전해질 시스템을 활용한 보다 지속가능하고 친환경적인 유기물 기반의 수계 배터리 시스템을 소개한다.

제2장에서는 고농도 수성 전해질로 적용가능한 저가의 용질을 찾기 위해 기존에 알려진 모든 일반적인 저가의 용질을 다시 검토하였다. 새로운 전해질을 찾는 전략으로 많이 녹으며 용질이 용매화 구조를 변화시킬 수 있는 가능성이 있는 저가의 무기질 용질을 찾았고, 결국 NaClO_4 고농도 용액이 효과적으로 수계 전해질의 전기안정적 창을 넓히며 물분해를 억제하고 ClO_4 용질의 분해 없이도 안전한 SEI 층을 형성할 수 있다는 것을 밝혔다. 용질의 분해 없이 형성된 SEI 층의 경우 Na_2CO_3 와 Na-O 및 NaOH 가 합쳐진 형태의 혼합물로 구성되어 있다는 것을 밝혔고 이 안전한 층은 수계 Na 셀에서 $\text{Na}_4\text{Fe}_3(\text{PO}_4)_2(\text{P}_2\text{O}_7)$ 양극과 $\text{NaTi}_2(\text{PO}_4)_3$ 음극으로 이루어진 배터리 시스템에서 안전한 사이클 성능과 전기화학적 에너지 저장 성능을

높이는데 큰 기여를 한다는 것을 증명하였다. 새로운 전략으로 찾아낸 이 저가의 수계 전해질 시스템은 훌륭한 사이클 안정성과 쿨롱 효율 (coulombic efficiency)를 제공하였고 이는 기존에 보고된 전해질의 성능을 월등히 초과하는 것을 보였다. 제2장에서 제안된 전략은 저가의 고전압 수계 시스템을 구성하는데 중요한 가이드라인을 제시하였다.

제3장에서는 고농도 NaClO_4 의 수계 전해질을 적용 범위를 넓히고 더욱 친환경적이고 지속가능한 수계 시스템을 개발하고자, 유기계 전극을 활용한 시스템을 개발하였다. 유기계 양극 물질로서 매우 유망한 p-type 특성을 갖는 다중 전자 산화 환원이 가능한 페나진기반의 분자를 (DMPZ) 고농도 수계 시스템에 적용하였다. DMPZ 물질의 용매도를 분석하여 수계 시스템이 DMPZ 물질의 용매도를 낮추어 가장 최적의 전해질로 사용할 수 있다는 것을 deep learning 기법과 실험을 통해 밝혔고, DMPZ의 모든 용량을 발현시키며 사이클 안정성을 증가시키기 위하여 제2장에서 개발한 저가의 고농도 NaClO_4 전해질 시스템을 적용하였다. 고농도 전해질은 DMPZ의 용해를 더욱 억제하며 추가로 물분해도 억제하여 DMPZ의 성능을 최대로 이끌어내는데 도움을 주었고, 최종적으로 매우 안정하고 우수한 사이클 안정성을 제공해주었다. 제3장에서는 유기계 전극 물질과 전해질 사이의 용해도와 전기화학적 성능에 대한 심도 깊은 이해를 제공해주었고, 이를 통해 보다 고성능에 지속가능하고 친환경적인 수계 유기 배터리를 개발하기

위한 전략을 제시하였다.

이 학위논문에서는 저가의 고에너지밀도를 갖는 수계 전해질 기반 이차전지를 개발하기 위한 전략으로 2가지 중요한 포인트를 제공해주었다: 1) 저가의 고농도 전해질을 개발하고 이를 통해 물분해를 억제하고 보다 넓은 범위의 전기화학적 안정성을 갖는 전해질을 개발하기 위한 전략 제시, 2) 보다 지속가능한 시스템을 만들어 줄 수 있는 유기계 기반의 전극 물질의 성능을 최대한 활용하기 위한 전략으로 전해질과 전극물질의 용매도에 대한 깊은 이해를 제공하고 이와 전기화학적 성능 간의 관계를 제시함으로써 각 유기계 전극 물질의 가장 적합한 전해질을 찾는 전략을 제시함. 본 학위논문은 통해 저가의 고에너지 밀도를 갖는 지속가능한 수계 고농도 시스템을 실현하기 위한 중요한 가이드라인을 제시해줄 것으로 기대된다.

주요어: 에너지 저장장치, 이차전지, 전기화학, 수계 배터리, 고농도 전해질

학번: 2012-24163